Seas in hot water –
marine heatwaves on the move;
following the heat.

Hillary A. Scannell

A dissertation
Submitted in partial fulfillment of the
Requirements for the degree of

Doctor of Philosophy

University of Washington
2020

Reading Committee:
LuAnne Thompson, Chair
Parker MacCready
Gregory Johnson

Program Authorized to Offer Degree:
Oceanography

University of Washington

Abstract

Seas in hot water –
marine heatwaves on the move;
following the heat.

Hillary A. Scannell

Chair of the Supervisory Committee:
LuAnne Thompson
School of Oceanography

Over the past decade marine heatwaves (MHWs) have gained increased attention due to their long-lasting impacts on marine ecosystems and the services they provide. These unusual, warm-water events have occurred throughout the global ocean, often having the most severe impacts along the coast. As ocean temperatures continue to rise due to anthropogenic greenhouse gas forcing, MHWs are expected to become more frequent, intense, and longer-lasting. This raises concerns for how dangerous MHWs may become in the future. This dissertation provides new insights into the spatiotemporal evolution of marine heatwaves using a global network of satellite and *in situ* observations. This work first describes the role of the ocean and atmosphere in driving upper ocean temperature seasonally using a mixed layer heat budget, which is essential to diagnosing the drivers of MHWs. The roles of subsurface temperature, salinity, and density are also examined with respect to the persistence and penetration of recent Northeast Pacific MHWs. Lastly, a new tracking algorithm is proposed to characterize the spatiotemporal evolution of MHWs globally, and to understand the sensitivities of spatial resolution and chosen thresholds in the detection of MHWs. This collection of work contributes to the eventual forecast of MHWs that will assist marine managers in mitigating the harmful impacts from these events in the future.

TABLE OF CONTENTS

ACKNOWLEDGEMENTS

I feel extraordinarily privileged to have had the opportunity to work alongside many brilliant people who have supported me throughout this journey. Before I express my gratitude, I must first acknowledge that my race most likely excluded me from the prejudices people of color face today in America, especially those in academia. Systemic racism is destructive in every aspect and we must do better to fix it. If you are reading this before the November 3, 2020 U.S. election and have not yet voted, please consider casting your ballot today.

There is no "one size fits all" Ph.D. and my advisor, LuAnne Thompson, recognized that. I am so grateful that she saw my potential early on and gave me the opportunity to succeed, while also trusting me with the freedom to pursue my own research interests. I have greatly enjoyed learning from LuAnne over the past five years and she continues to be my role model moving forward.

I owe a great deal of gratitude to my co-authors and colleagues, which include several close mentors. These collaborations have not only helped energize pioneering new research, but have also made doing science a lot more fun. I would especially like to thank Gregory Johnson, Neil Holbrook, Eric Oliver, Alistair Hobday, Alex Sen Gupta, Matthew England, David John Gagne, Daniel Whitt, and Andrew Pershing for all they have taught me.

I would be remiss if I did not also recognize the community within the School of Oceanography that has created a truly welcoming and friendly environment to work. In addition to their support, I wish to acknowledge that this dissertation would not be possible without the financial support from the Leonardo DiCaprio Foundation and Microsoft AI for Earth. I have learned throughout this Ph.D. that there are many creative ways to fund science by identifying those who support your ambition. Thank you sincerely to everyone who has supported mine.

DEDICATION

"There is only one way to eat an elephant: a bite at a time."

— Desmond Tutu

Starting from a young age, I was taught by my parents to persevere and to not give up when times were difficult. The famous quote from Desmond Tutu, a South African human rights activist, represents the idea that progress is made one step at a time. My parents, Mark and Malinda Scannell, have supported me in every step of my life. They have celebrated each of my accomplishments as if they were their own and shared in my sorrows during my failures. Their exuberance, love, and support is never ending. I am reminded everyday how lucky I am to be their daughter and dedicate this entire dissertation in their honor. I love you both.

LIST OF FIGURES

LIST OF TABLES

INTRODUCTION

The ocean acts as the largest reservoir of heat in Earth's climate system and plays a critical role in regulating climate on seasonal to centennial timescales. As the climate warms due to anthropogenic greenhouse gas forcing, the ocean responds by absorbing and storing excess heat from the atmosphere. As with heatwaves on land, climate change also causes dangerous hot-water events to become more frequent in the ocean. These extreme events, called *marine heatwaves* (MHWs), are increasing in frequency globally leading to prolonged periods of thermal stress in the marine environment. Several recent high profile MHWs have occurred over the last decade and these events have raised global awareness for how oceanographic extremes and their drivers may alter ecological communities and human-ecosystem interactions.

The study of MHWs is highly interdisciplinary owing to its impacts on physical, biogeochemical, and societal systems. The field has rapidly evolved since its humble beginnings in 2011, with a focus now on developing new approaches to help society respond to and manage these evolving threats. This dissertation provides new insights into the spatiotemporal evolution and persistence of MHWs by **(1)** quantifying the drivers of sea surface temperature variability using a mixed layer heat budget, **(2)** characterizing the role of the subsurface ocean in the persistence of long-lived MHWs, and **(3)** developing a framework to track the spatiotemporal evolution of MHWs globally. This Introduction aims to provide a synthesis of the history,

current progress, and future challenges in the field of ocean temperature extremes before delving into the contributions of this dissertation

Definitions and Categorization

One of the earliest discoveries of temperature extremes in the marine environment was made by anchovy fishermen off the coasts of Peru and Ecuador around the seventeenth century. They observed periodic warm spells off the Pacific coast of South America coincident with when fish could not be found. Today we know this event as El Niño, and it is the most well studied warming phenomenon in the ocean. Fast forward to the late 1990s, researchers began linking periods of elevated sea surface temperature (SST) with coral bleaching, which is still today the most advanced field of thermal stress-related marine ecology (Donner et al., 2005; Spillman and Alves, 2009). Metrics such as degree heating weeks were developed to monitor and predict coral bleaching events (Eakin et al., 2010). Temperature extremes are increasingly recognized as important influences on biological systems, yet when the first MHW was described (Pearce et al. 2011) there was no consistent definition to assess its impact.

Shortly after the 2011 warm event off Western Australia first described by Pearce et al. (2011), another so-called "ocean heat wave" occurred in the Gulf of Maine during the summer of 2012 (Mills et al., 2013). At the time there were very few people studying these warm spells and our understanding was purely based on one-off events. Recognizing the relationships between these two events, a small group of 15 international climate scientists, oceanographers, atmospheric scientists, and ecologists gathered at the University of Western Australia Oceans Institute in

Perth, Australia for the first of three workshops focused on defining MHWs and summarizing their physical drivers and impacts (**Figure 1**).

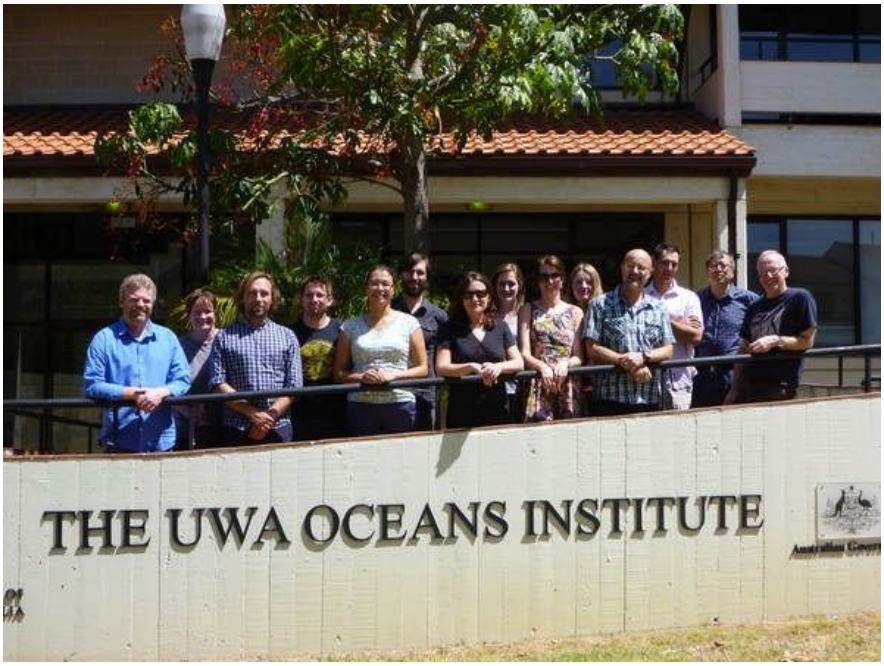

Figure 1. Participants of the first international marine heatwave workshop at the University of Western Australia Oceans Institute in Perth, Australia in January 2015. From left to right are Neil Holbrook, Pippa Moore, Markus Donat, Dan Smale, Jessica Benthuysen, Eric Oliver, Lisa Alexander, Hillary Scannell, Sarah Perkins, Sandra Straub, Thomas Wernberg, Alistair Hobday, Ming Feng, and Michael Burrows. Alex Sen Gupta was not present, however contributed. Photo is borrowed with permission from http://www.marineheatwaves.org.

One of the first outcomes from the workshop was a paper led by Alistair Hobday that set forth a framework to consistently define and characterize MHWs (Hobday et al., 2016). Using the lessons learned from the more established atmospheric community to define extreme temperature events, Hobday et al., (2016) proposed a qualitative and quantitative definition for characterizing MHWs across all regions. They consider a MHW to be a "*discrete prolonged anomalously warm water event*" defined when the SST exceeds a threshold set by the 90th percentile relative to a

30-year fixed historical baseline. The 99th percentile has subsequently been used to also define MHWs (Frölicher et al., 2018; Frölicher and Laufkötter, 2018; Darmaraki et al., 2019) — such as in the Intergovernmental Panel of Climate Change (IPCC) Special Report on the Ocean and Cryosphere (SROCC) (Collins et al., 2019). According to Hobday et al. (2016), a MHW must also persist for at least 5 or more consecutive days with no more than a 2-day gap. Any event shorter than 5-days is considered a heat spike (Hobday et al., 2016). This definition requires MHWs to be discrete, meaning that they have a well-defined start and end date such that a duration can be quantified.

Categorical classifications for MHWs have also been proposed to group events according to the maximum temperature anomaly above the local climatology (Hobday et al., 2018). Similar to classifying hurricanes, MHWs are grouped into categories as either being "moderate", "strong", "severe", or "extreme" (Hobday et al., 2018). These categories correspond to the multiples of the 90th percentile difference from the mean climatology that the SST exceeds (i.e., 1x=*moderate*, 2x=*strong*, 3x=*severe*, 4x=*extreme*). Oliver et al. (2019) show that under Radiative Concentration Pathway (RCP) 4.5, there will be a dramatic increase in strong, severe, and extreme MHWs by year 2100. Even worse, under RCP8.5, the majority (70%) of all MHWs will be considered extreme by the end of the 21st Century. These MHW categories provide a consistent syntax to facilitate the communication and comparison of events, however it is only a descriptive measure and does not necessarily diagnose MHW drivers.

Other metrics for characterizing MHWs have used statistical distributions of anomaly areal extent to describe regional differences in event statistics. Scannell et al. (2016) found that the areal extent of MHWs defined by an SST threshold of one standard deviation above the regional mean follows a fat-tailed power law distribution where small area anomalies occur more frequently than large area anomalies. The shape of the power law (i.e., probability of a particular sized event) is determined by the intensity and duration of the event. For example, a large area, high intensity, and long-lasting MHW is less likely to occur than a small area heat spike. Scannell et al. (2016) further show that these statistics are influenced by large-scale modes of natural climate variability, such as the El Niño-Southern Oscillation (ENSO), by changing the underlying regional structure of background SST.

The definitions proposed by Hobday et al. (2016; 2018) can be applied more broadly to assess the local physical processes and remote drivers of MHWs using heat budget analyses and statistical methods. Our understanding of MHW drivers represents the culmination of several regional case studies, including in the northern Mediterranean Sea (Olita et al., 2006; Sparnocchia et al., 2006), along the coast of Western Australian (Pearce and Feng, 2013), in the northwest Atlantic (Chen et al., 2014), in the northeast Pacific (Bond et al., 2015; Di Lorenzo and Mantua, 2016), and off southeastern Australia (Oliver et al., 2017). Knowing the drivers of MHWs helps to inform their predictability by increasing our capacity to detect and understand their emergence on a global scale.

Physical Drivers

Anomalous weather patterns play a crucial role in controlling the extent and location of some MHWs. Reduced cloud cover, light winds, high surface air temperatures, and humidity all influence local air-sea heat flux that can generate and maintain MHWs (Holbrook et al., 2019). For example, high synoptic atmospheric sea level pressure over the Northeast Pacific during 2013–2014 reduced surface wind speeds that led to lower rates of wintertime turbulent heat loss from the ocean to atmosphere and resulted in widespread warming (Bond et al., 2015). In addition to changes in atmospheric heat flux, advection by warm ocean currents forced by changes in local and remote surface winds can contribute to localized warming. For example, the intensification of the easterly Trades in the equatorial Pacific during La Niña were associated with the poleward acceleration of the Leeuwin Current along the coast of Western Australia during a 2011 MHW (Feng et al., 2013). A useful diagnostic to understand the dominant drivers of specific MHWs is the quantification of the upper ocean mixed layer heat budget.

The mixed layer heat budget represents the balance of local processes directly affecting the rate of temperature change in the uppermost part of the ocean, including contributions from advective and air-sea heat fluxes. The derivation of the mixed layer heat budget is discussed further in **Chapter 1**. In order to generate a MHW, the mixed layer heat fluxes must sufficiently contribute to large net positive temperature tendencies that act to warm SST over a threshold (e.g., 90^{th} percentile). While the mixed layer temperature budget can diagnose MHW drivers in the upper ocean, we know that MHWs also extend deeper. In **Chapter 2**, we describe the mechanisms through which surface MHW anomalies could penetrate the subsurface where they can persist.

Warming within the mixed layer during MHWs has also been connected to large-scale modes of natural climate variability, either through local extreme ocean-atmosphere coupled feedbacks (e.g., eastern equatorial Pacific during El Niño) or by remote teleconnection mechanisms (e.g. propagation of planetary-scale waves in the atmosphere or oceanic Kelvin waves). Holbrook et al. (2019) and Scannell et al. (2016) both found that these large-scale climate modes act as important modulators for the enhancement or suppression of MHW occurrences.

Global Trends and Patterns

MHWs have become ubiquitous features of the climate system owing to the forced response of increased atmospheric CO_2 concentrations (Laufkötter et al., 2020; Frölicher et al., 2018; Oliver et al., 2018). Oliver et al. (2018) apply the Hobday definition to characterize MHWs globally and show positive trends in frequency and duration between 1925 to 2016. Frölicher et al. (2018) also found similar globally averaged trends in frequency and duration, and a doubling in the number of MHW days over the same time period for summertime MHWs defined relative to the 99^{th} percentile threshold. Oliver et al. (2018) and Frölicher et al. (2018) both attribute the observed trends in MHW statistics to anthropogenic climate change.

The forced response can be either mitigated or enhanced due to intrinsic variability within the climate system (Scannell et al., 2016; Joh and Di Lorenzo, 2017). Large-scale spatial patterns of MHW characteristics reveal hotspots in intensity, for example in the western boundary currents (Oliver et al., 2018). The eastern tropical Pacific has some of the longest lasting and most intense

MHWs compared to other regions due to a strong influence from ENSO. These MHWs, however, are less frequent owing to the 3-7 year periodicity of ENSO events (Deser et al., 2010). The teleconnections associated with tropical ENSO dynamics also influence MHW hotspots in remote locations such as in the northeast Pacific (Hartmann, 2015; Di Lorenzo and Mantua, 2016), off the west coast of Australia (Feng et al., 2013), and in the central South Pacific (Lee et al., 2010).

Impacts

The effects from MHWs cascade through complex physical, ecological, and societal systems that can lead to increased economic tensions between nations (e.g., Mills et al., 2013). Consequences of MHWs have included closures of lucrative fisheries and changes to catch quotas (Caputi et al., 2016; Cavole et al., 2016; McCabe et al. 2016; Oliver et al., 2017), widespread coral bleaching (Hughes et al., 2017; McGowan and Theobald, 2017), nutrient depletion in coastal surface waters (Bond et al., 2015; McCabe et al. 2016), mass mortality of marine invertebrates (Garrabou et al., 2009), the collapse of kelp forests (Wernberg et al., 2016), and shifts in species' range distributions that unsettle ecological community structure (Mills et al., 2013; Wernberg et al., 2016).

Dissertation Outline

- **Chapter 1** investigates the seasonal cycle of SST in the southeast tropical Atlantic where there are large model biases. A mixed layer heat budget is commonly used to diagnose the drivers of MHWs, here it is applied to estimate the seasonal cycle. MHWs occur on

top of the seasonal cycle so it is important to understand the components driving the seasonal fluctuations of SST. We use data from the 6ºS, 8ºE Prediction and Research Moored Array in the Tropical Atlantic (PIRATA), augmented with in-situ observations from satellites and Argo.

- **Chapter 2** characterizes the subsurface structure of temperature, salinity, and density related to recent MHWs occuring in the northeast Pacific. We use Argo data from 2.5 to 1,785 dbar and compare the two extreme MHWs during 2013–2016 and 2019–2020.

- **Chapter 3** develops a new method for tracking the spatiotemporal evolution of MHWs globally. We explore the sensitivities of the MHW definition and tracking parameters for well-known 21st Century MHWs.

Chapter 1

SEASONAL MIXED LAYER TEMPERATURE BALANCE IN THE SOUTHEASTERN TROPICAL ATLANTIC

1.1 Abstract

Most climate models simulate sea surface temperatures (SSTs) that are consistently 1–4 °C warmer than observed in eastern tropical Atlantic. These biases undermine seasonal prediction efforts and the credibility of climate change projections in this region. To understand what drives the seasonal cycle in upper ocean temperature near the eastern boundary of the tropical Atlantic, we use a 5-year moored buoy data set from the Prediction and Research Moored Array in the Atlantic at 6°S, 8°E. The buoy is located along the southeastern edge of the Atlantic cold tongue where the seasonal cycle in SST, which is maximum in March and minimum in August, is influenced by the meridional movement of the Intertropical Convergence Zone (ITCZ) and formation of low-level marine stratocumulus clouds. Associated with these seasonal changes in atmospheric conditions, surface heat fluxes on seasonal timescales are most strongly controlled by shortwave radiation and latent heat flux. The seasonal mixed layer shoals, warms, and freshens in the boreal spring coincident with a southward migration of the ITCZ. The shallow mixed layer amplifies heating from solar radiation on mixed layer temperature at this time. Conversely, during the boreal summer, upwelling leads to entrainment of cold and salty water

into the surface layer. From this analysis, we discuss the relative importance of the different components of the seasonal mixed layer heat balance at 6°S, 8°E and how they can be used to better understand the sources of climate model SST biases.

1.2 Introduction

The tropical Atlantic Ocean and atmosphere are strongly coupled through the transfer of heat, momentum, and moisture across the air-sea interface, with variability in these exchanges dominated by the seasonal cycle. In the eastern basin, the African continent plays an important role in shaping the structure of surface currents and consequently the distribution of sea surface temperature (SST). Along the eastern boundary, the warm Angola Current flows southward along the African coast to 15–17°S where it is met and deflected offshore by a cool equator-flowing Benguela Current. The strength and direction of these currents are modulated on seasonal and interannual timescales by local near-surface wind stress (Bachèlery et al., 2016; Richter et al., 2010) and remote forcing by equatorial and coastally trapped waves (Bachèlery et al., 2016; Florenchie et al., 2003; Lübbecke et al., 2010; Rouault et al., 2007).

Wind patterns in the eastern tropical Atlantic associated with the Intertropical Convergence Zone (ITCZ) migrate latitudinally in response to the seasonal heating and cooling of the Northern and Southern Hemispheres. The meridional movement of the ITCZ and distribution of SST and sea surface salinity (SSS) are closely coupled and dominated by the seasonal cycle (Yu et al., 2006). The ITCZ can be traced by a band of heavy precipitation, increased high level clouds, and weakened wind speeds (Figure 1.1). During March, SSTs greater than 27 °C and heavy

precipitation are zonally uniform and co-located between the equator and 5°S in the southeast Atlantic (Xie & Carton, 2004). Increased precipitation and river runoff decreases SSS in the Gulf of Guinea and along the eastern boundary during this time of year (Figure 1.1).

During the boreal summer, the ITCZ reaches its northernmost extent centered near 8°N associated with the onset of the West African Monsoon and formation of the equatorial cold tongue (Xie & Carton, 2004; Yu et al., 2006). Monsoon winds intensify in the Gulf of Guinea from an increase in convection and precipitation over the North African continent. Simultaneous strengthening of the South Atlantic anticyclone enhances upwelling of cold, saline water along the African coast and along the equator (Figure 1.1). Low-level marine stratocumulus clouds expand over the upwelled cold deep-water in the southeast Atlantic. These clouds reflect solar radiation and reinforce the cooling of SST (Figure 1.1).

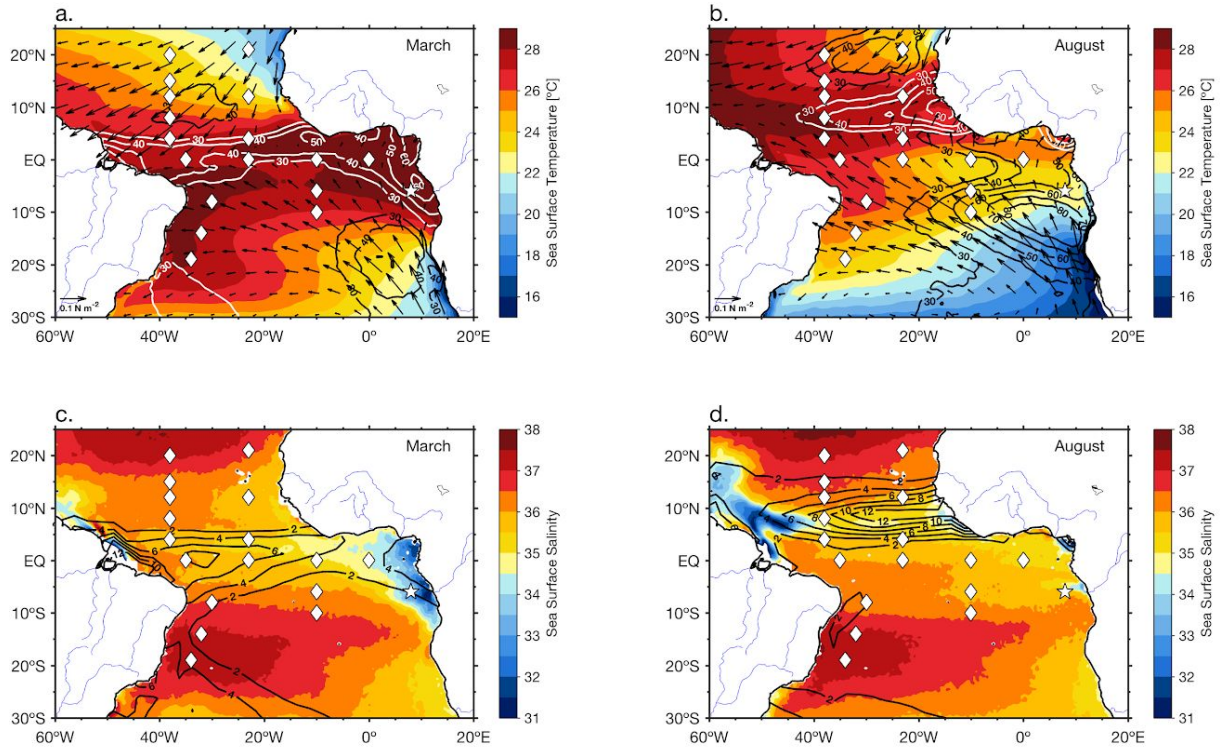

Figure 1.1 Climatological March and August snapshots of the tropical Atlantic. Mean (a) March and (b) August sea surface temperature (SST) and wind stress vectors with contoured percent cover of high level clouds (white lines) and low level clouds (black lines). Mean (c) March and (d) August sea surface salinity with contoured monthly averaged precipitation (mm/day). Locations of the Prediction and Research Moored Array in the Atlantic buoys are marked by diamonds and a star for the southeast extension (6°S, 8°E). Major rivers are shown over continents. Monthly wind stress data are from TropFlux between 1979 and 2017. Percentages of low (>680 hPa) and high (<440 hPa) level clouds (a and b) are retrieved from MODIS-Terra from 2002 to 2015 and represents the total fraction of a 1° latitude by1° longitude grid cell covered by clouds. Monthly precipitation (c and d) come from the Climate Prediction Center Merged Analysis of Precipitation from 1979 to 2017. SST is averaged from the daily optimum interpolation SST data set from 1981 to 2018 and sea surface salinity comes from the Soil Moisture Ocean Salinity mission available from 2010 to 2016.

During the boreal summer, the ITCZ reaches its northernmost extent centered near 8°N associated with the onset of the West African Monsoon and formation of the equatorial cold tongue (Xie & Carton, 2004; Yu et al., 2006). Monsoon winds intensify in the Gulf of Guinea from an increase in convection and precipitation over the North African continent. Simultaneous

strengthening of the South Atlantic anticyclone enhances upwelling of cold, saline water along the African coast and along the equator (Figure 1.1). Low-level marine stratocumulus clouds expand over the upwelled cold deep-water in the southeast Atlantic. These clouds reflect solar radiation and reinforce the cooling of SST. (Figure 1.1).

Of particular significance to the southeast tropical Atlantic is the systematic errors in sea surface temperature in global climate models. Most models in phase 5 of the Coupled Model Intercomparison Project, for example, simulate sea surface temperatures that are too warm with respect to observations, especially along the coasts of Namibia and Angola. Biases in the southeastern tropical Atlantic range typically from 1 to 4 °C with the most severe warm biases up to 6–8 °C (Zuidema et al., 2016). This persistent and widespread problem is characteristic of earlier generations of Coupled Model Intercomparison Project models as well. The largest contribution to the warm biases is primarily the excessive solar insolation caused by the underestimation of low level marine stratocumulus clouds and from insufficient turbulent vertical mixing of cold water across the base of the mixed layer (Exarchou et al., 2017; Richter, 2015). It is suggested that SST biases in coupled climate models can feedback on cloud biases and influence the location of deep convection through large-scale circulation. As a consequence, systematic errors in deep convection also have the potential to shift the distribution of precipitation that influences horizontal gradients in SSS (Zuidema et al., 2016). These biases limit our ability to accurately simulate regional and global climate variability and change (Qu et al., 2014; Sherwood et al., 2014) and present a challenge in modeling and predicting droughts, floods, severe tropical storms, and hurricanes, which impact millions of people in the region.

Process-based observational analyses are therefore needed to further understand what drives the seasonality of SSTs in regions with severe model bias.

Previous studies of the mixed layer temperature balance in the tropical Atlantic have benefited from data collected as part of the Prediction and Research Moored Array in the Tropical Atlantic (PIRATA). This network is comprised of 18 moored ocean buoys that continually measure oceanic and atmospheric conditions in the tropical Atlantic (Bourles et al., 2008; Figure 1.1). The moorings collect and transmit to shore in real-time high temporal resolution data to support the study of ocean-atmosphere interactions and ocean dynamics in the tropical Atlantic. Foltz et al. (2003) used these data to diagnose the mixed layer heat budget at eight PIRATA moorings in the northwest (8°N–5°N along 38°W), equatorial (between 10°W and 35°W) and southeastern (6°S–10°S along 10°W) areas of the basins. They found that off the equator the seasonal cycle of mixed layer temperature is primarily balanced by latent heat loss and shortwave radiation, whereas along the equator the role of horizontal advection and entrainment becomes increasingly important. A model study by Yamagata and Iizuka (1995) at the off-equatorial location of 10°S, 9°E also found that surface fluxes drive the seasonal cycle, with cooling March through August and warming September through February.

The mooring at 6°S, 8°E did not exist at the time that Foltz et al. (2003) performed their analysis. This mooring is in an oceanic region that has been historically undersampled and where model SST biases are relatively large compared to other PIRATA sites (Zuidema et al., 2016). This site is also of interest because it sits on the southeastern edge of the Atlantic cold tongue where

upwelling and turbulent entrainment may contribute to the seasonal evolution of mixed layer temperature (e.g., Foltz et al., 2003). We describe in detail the various processes that give rise to the seasonal evolution of SST at this site and discuss the implications of our results for climate model SST biases in the southeastern tropical Atlantic.

1.3 Data and Methods

1.3.1 PIRATA-Southeast Extension 6°S, 8°E

Since the initial implementation of PIRATA in 1997 (Servain et al., 1998), the array has undergone a series of extensions and enhancements. One of these expansions includes the PIRATA-Southeast Extension (PIRATA-SEE) at 6°S, 8°E that was initiated in 2005 (Rouault et al., 2009). A pilot phase began in June 2006 through June 2007, and the mooring has been continually operational since June 2013. We use the daily data record from PIRATA-SEE since June 2013, which extends almost 5 years to present (Figure 2).

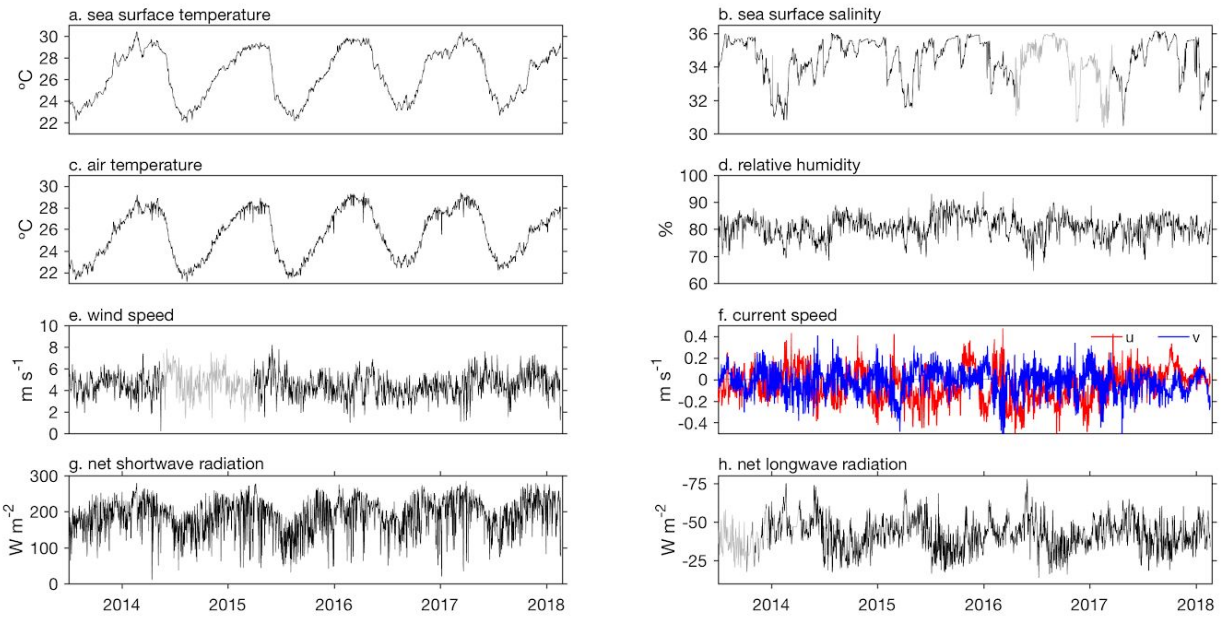

Figure 1.2 Daily ocean surface and meteorological measurements from the Prediction and Research Moored Array in the Atlantic-Southeast Extension mooring at 6°S, 8°E. Gaps in the data record for (e) wind speed and (h) net longwave radiation are extrapolated using a least squares regression with data from the TropFlux product. Missing data in (b) sea surface salinity are extrapolated from least squares regression of salinity at 1 and 5 m. Net longwave radiation assumes a broadband emissivity of 0.97 at the sea surface and net shortwave radiation assumes a surface albedo of 0.055. The sign convention is positive for surface heat flux into the ocean and vice versa.

The PIRATA-SEE site was occupied with an Autonomous Temperature Line Acquisition System mooring from 2013 to 2017 and later with a functionally equivalent T-Flex system beginning in March 2017. Subsurface temperature is available at 14 depth intervals from 1 to 500 m and subsurface salinity at 9 depth intervals from 1 to 120 m. Temperature is sampled at 1, 3, 5, 10, 20, 40, 60, 80, 110, 120, 140, 180, 300, and 500 m, and subsurface salinity is sampled at 1, 3, 5, 10, 20, 40, 60, 80, and 120 m. Subsurface temperature and salinity at 3 m was not available until late March 2017 with the implementation of the T-Flex mooring sensor upgrade. We refer to the 1-m values of temperature and salinity as SST and SSS, respectively. Temperature and salinity are measured hourly and are available from the National Oceanic and Atmospheric

Administration/Pacific Marine Environmental Laboratory Global Tropical Moored Buoy Array Project website (https://www.pmel.noaa.gov/gtmba/). For the purposes of this study, we use daily averages computed from higher-resolution hourly data.

Temporal gaps in daily subsurface salinity at 1 and 5 m toward the end of the record are filled using orthogonal linear least squares regression relationships between 10 and 1 m and 10 and 5 m, respectively. Salinity covaries significantly across depths within the upper 10 m, so that a linear regression model using 10 m salinity predicts 92.8% of the variance in 5-m salinity, and 92.6% of the variance in 1-m salinity. The root-mean-square error is 0.74 for 5-m salinity estimates and 0.77 for 1-m salinity estimates. After filling gaps in the time series, subsurface temperature and salinity profiles are linearly interpolated in the vertical to 1-m resolution. Subsurface density (σ_T) is then computed from temperature and salinity. Vertical profiles of temperature, salinity, and density show a strong seasonal cycle in a very shallow mixed layer (Figure 1.3).

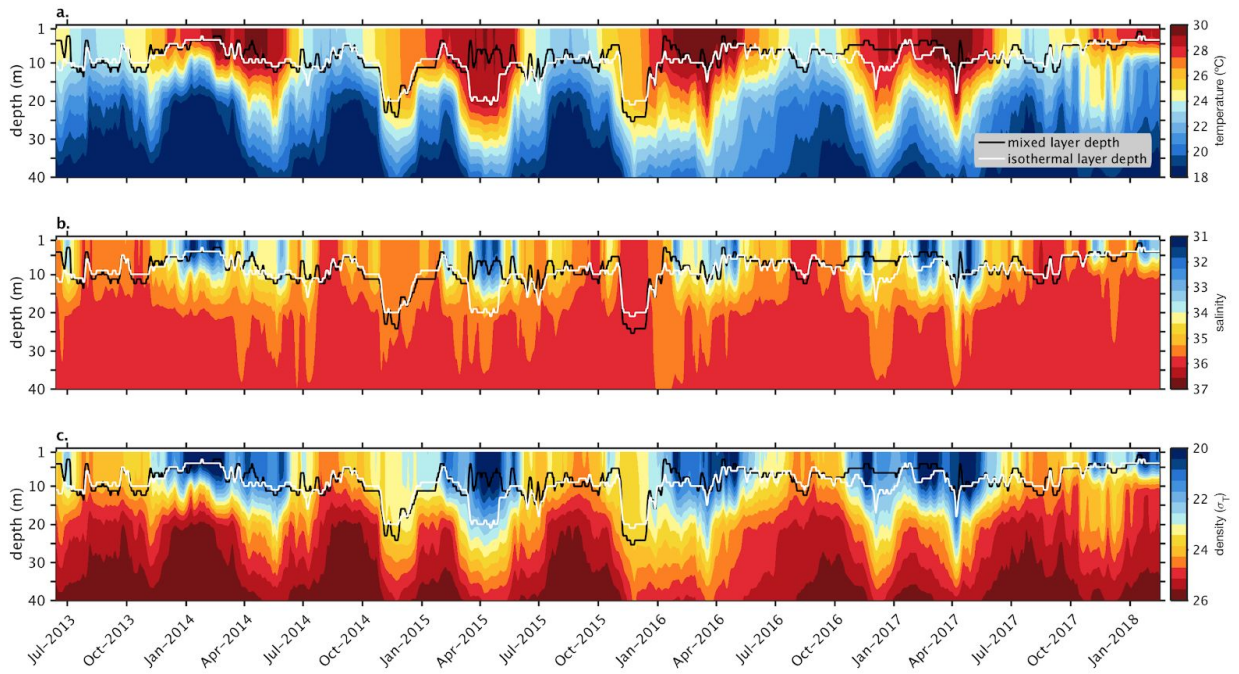

Figure 1.3 Upper ocean hydrographic structure at the Prediction and Research Moored Array in the Atlantic-Southeast Extension buoy from June 2013 to February 2018. Daily profiles of (a) temperature, (b) salinity, and (c) density (σT) in the upper 40 m are vertical interpolated to a 1-m resolution and smoothed temporally with a 7-day triangle filter to eliminate high-frequency variability. Mixed layer depth (black line) and isothermal layer depth (white line) are calculated for each interpolated profile using a 0.3 °C temperature decrease from a 1-m reference level.

Instrumental accuracy is ±0.02 °C and ± 0.02 for temperature salinity respectively (A'Hearn et al., 2002; Freitag et al., 1999, 1995, 2016). A single-point acoustic-Doppler current meter at 10-m depth measures both zonal and meridional current velocities at an hourly sampling interval with ±5 cm/s accuracy (Plimpton et al., 1995, 2004). Near-surface air temperature and relative humidity are sampled at 10 min intervals 3 m above the sea surface and have accuracy within ±0.2 °C and ± 2.7% respectively (Lake et al., 2003). Rainfall is sampled every 10 min from a gauge 3 m above the sea surface with ± 0.4 mm/hr accuracy (Serra et al., 2001). Shortwave and longwave radiation is measured every 2 min from sensors 3.5 m above the sea surface with instrument accuracy ±2% and ± 1%, respectively (Cronin & McPhaden, 1997). Net shortwave

radiation assumes a surface albedo of 5.5% and net longwave radiation assumes a sea surface emissivity of 0.97. An anemometer at 4 m above the sea surface records wind speed every 10 min with accuracy ±0.3 m/s (Freitag et al., 2001).

We fill gaps in wind speed and net longwave radiation using an orthogonal least squares linear regression based on the relationships between the PIRATA-SEE data and the TropFlux reanalysis of air-sea heat and momentum flux (Kumar et al., 2013; Figure 1.2). TropFlux, available from 1979 onward, is derived from the European Reanalysis-Interim and the International Satellite Cloud Climatology Project and has been bias- and amplitude-corrected based on the Global Tropical Moored Buoy Array (Kumar et al., 2013). TropFlux longwave radiation explains 81.3% of variance in net longwave radiation measured at the PIRATA-SEE buoy. TropFlux wind speed data are located at 10 m above the sea surface. To compare with PIRATA, we adjust the 4-m PIRATA wind speed data to 10 m using the neutral wind equation following Smith (1988), which assumes that wind speed increases logarithmically with height to a first approximation. TropFlux wind speed explains 91.7% of variance of the adjusted wind speed measured at the PIRATA-SSE buoy.

To describe the seasonal cycle in the southeast tropical Atlantic, we analyze the mixed layer heat budget using data available from PIRATA-SEE at 6°S, 8°E. To eliminate high-frequency variability, we fit daily data with mean, annual, and semiannual harmonics using least squares regression. Daily profiles of temperature and salinity are fit using this procedure to show seasonal variations in the upper 45 m (Figures 4c and 4d). We expect that the largest source of

uncertainty given the short observational record will be from sampling errors estimated from deviations about the harmonic fits to the data and that instrumental and computational errors are relatively small compared to these errors. Errors in this analysis are therefore expressed as 1 standard error based on year-to-year deviations from the mean seasonal cycle.

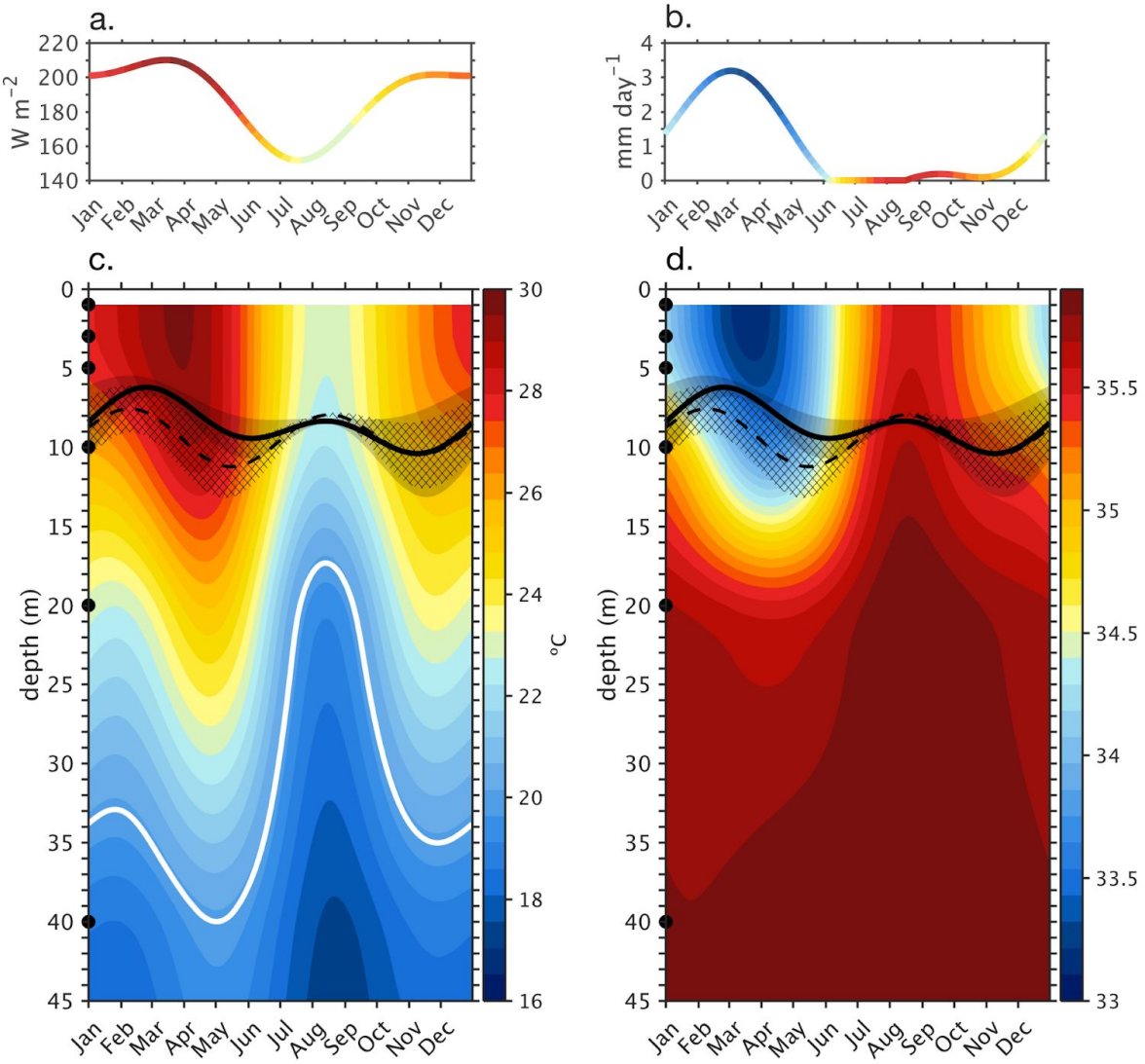

Figure 1.4 Seasonal cycles of mixed layer temperature and salinity 6°S, 8°E. Mixed layer temperature and salinity are influenced by (a) net downwelling shortwave radiation and (b) precipitation measured at the Prediction and Research Moored Array in the Atlantic buoy with a color encoding that corresponds to the average mixed layer temperature and salinity, respectively. Upper 40-m (c) temperature with 20 °C isotherm depth (white line), mixed layer depth (solid black line), and isothermal layer (dashed black line), and (d) salinity show water column stratification. Mixed layer temperature and salinity are computed as the integration of values from the sea surface to the base of the mixed layer. The mixed layer depth is defined as a 0.08 kg/m3 density (σ_T) increase from a 1-m reference level, and its standard error (gray shading) is based on interannual anomalies the 2013–2018 mean seasonal cycle. The isothermal layer depth (dashed line) is defined as the depth at which temperature decreases 0.3 °C from a 1-m reference level and is shown with its monthly standard error (cross hatches). Dark circles in (c) and (d) represent the depths of direct PIRATA measurements used to linearly interpolate data to a 1 m vertical resolution.

1.3.2 Heat Balance

The processes responsible for determining mixed layer temperature are represented by the following balance of terms (Moisan & Niiler, 1998; Stevenson & Niiler, 1983):

$$\rho c_p h \frac{\partial T}{\partial t} = -\rho c_p h(\mathbf{v} \cdot \nabla T\ ) + q_o + \varepsilon. \tag{1}$$

From left to right, the terms in (1) represent the time rate of change of mixed layer heat storage, which is balanced by mean horizontal heat advection, net surface heat flux absorbed in the mixed layer, and a residual term. Parameters in equation (1) include the mixed layer density (ρ), specific heat of seawater (c_p), mixed layer depth (h), and the time rate of change of the vertically averaged mixed layer temperature (T). Horizontal advection is a function of the vertically averaged mixed layer velocity (v) and the horizontal gradient of mixed layer temperature.

Net surface heat flux (q_o) is the sum of net downwelling shortwave radiation (SWR) minus the shortwave radiation that penetrates through the base of the mixed layer (SWR_{pen}), net longwave radiation (LWR), latent (LHF), and sensible heat fluxes (SHF), such that

$$q_o = \left(\mathrm{SWR} - \mathrm{SWR_{pen}}\right) + \mathrm{LWR} + \mathrm{LHF} + \mathrm{SHF}. \tag{2}$$

The penetration of shortwave radiation through the mixed layer is controlled by the optical properties of the mixed layer and its depth. As in Foltz et al. (2003), we evaluate two models to estimate shortwave penetration. The first is a chlorophyll-dependent empirical model for penetrative shortwave radiation that takes into account biological productivity using chlorophyll-a concentration, $Q_{pen} = 0.47 Q_{surf}\, e^{-\left(0.027 + 0.518 CHL^{0.428}\right) h}$ (Morel, 1988). The amount of

penetrative shortwave radiation relies on the surface shortwave radiation (Q_{surf}), satellite-derived chlorophyll-*a* concentration (CHL) from National Aeronautics and Space Administration Moderate Resolution Imaging Spectroradiometer-Aqua (MODIS-Aqua) and the depth of the mixed layer (h). We compute the monthly climatology of the satellite derived chlorophyll-*a* concentration (mg/m^3) averaged across 5–7°S and 7–9°E to find the monthly climatology of penetrative shortwave radiation. We compare the empirical model with one that assumes a 25-m *e*-folding decay of shortwave radiation, $Q_{pen} = 0.45Q_{surf}\, e^{-\gamma h}$, where γ is the decay rate constant, 0.04 m^{-1} (Wang & McPhaden, 1999). Gamma is set to larger values in biologically productive regions or near high river runoff. Both models have similar seasonal cycles; however, there is a 12–26 W/m^2 bias seasonally between the two radiation models where the chlorophyll-based model always estimates more absorbed shortwave radiation than the exponential decay model (Figure 1.5). The influence of high biological productivity in a region with shallow mixed layers exerts a large effect on the total absorbed shortwave radiation. We therefore use the empirical chlorophyll-*a* model to derive penetrative shortwave radiation in this analysis.

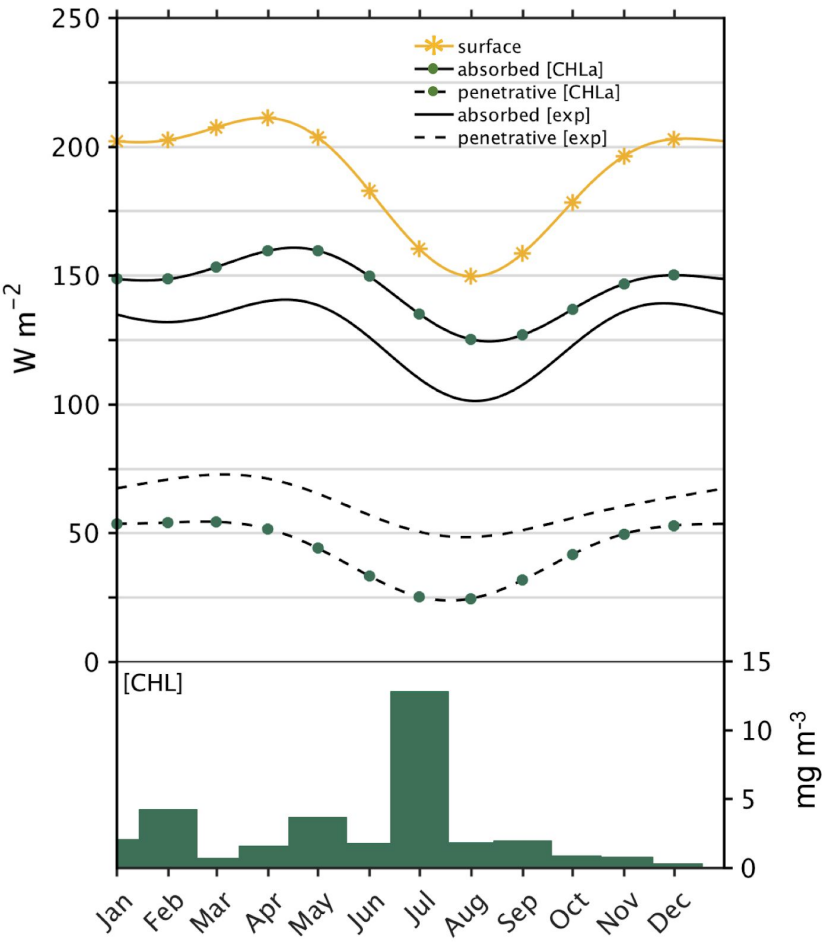

Figure 1.5 Seasonal cycles of downwelling surface radiation, estimated absorbed radiation within the mixed layer and penetrative shortwave radiation at the base of the mixed layer at 6°S, 8°E. Two methods are compared: (1) using a 25 m *e*-folding decay of net surface shortwave radiation to estimate the amount absorbed (solid black line) and penetrative (dashed black line) and (2) using an empirical approximation based on the concentration of chlorophyll-a at the sea surface to compute the absorbed (solid green dot line) and penetrative (green dash-dotted line) radiation. The monthly climatology of chlorophyll-*a* concentration is estimated from the MODIS-Aqua mission. All data are monthly averaged and fit with mean, annual, and semiannual harmonics.

Absorbed shortwave radiation is determined from equation (2) as the difference between downwelling shortwave radiation at the surface and that which penetrates through the base of the mixed layer. To understand the seasonal effects of clouds on the mixed layer heat budget, we compare the absorbed shortwave radiation with the noontime maximum in solar radiation when

no clouds are present (Figure 1.6). The clear-sky global horizontal irradiance is calculated using the Adnot-Bourges-Campana-Gicquel model

$$\mathrm{GHI} = 951.39\cos(\theta_z)^{1.15}, \tag{3}$$

which is a univariate function of the solar zenith angle (θ_z) at 6°S (Badescu, 1997).

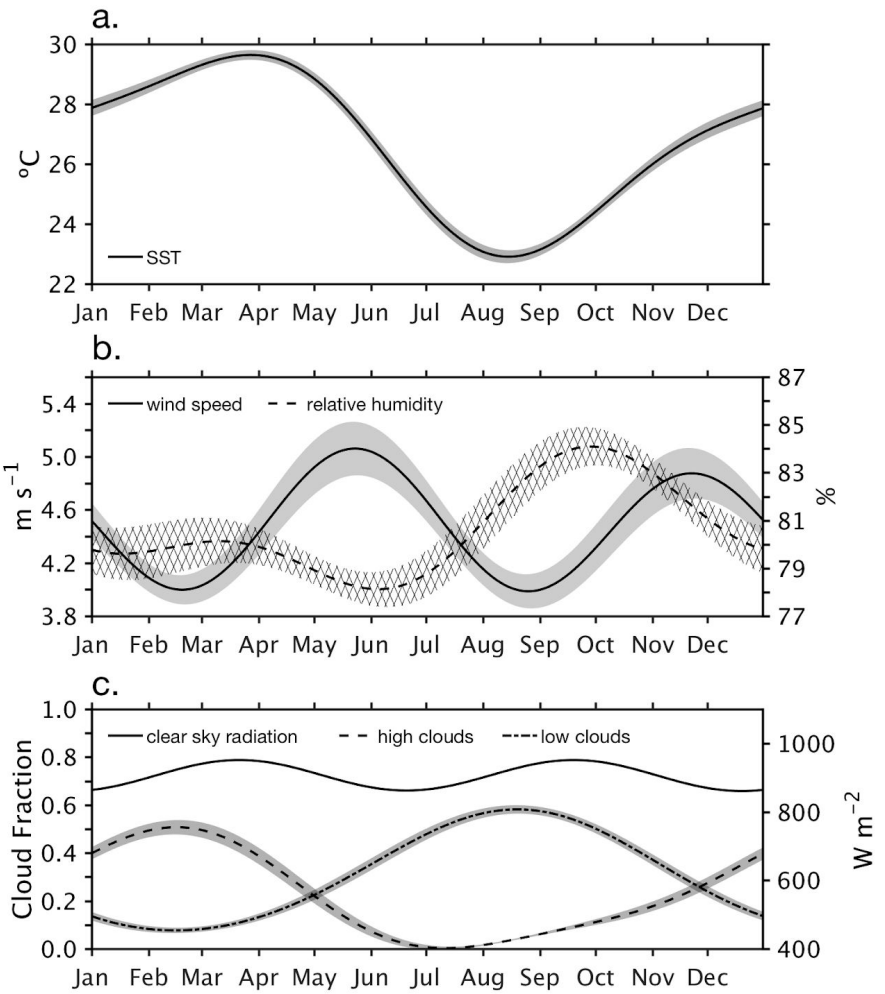

Figure 1.6 Mean seasonal cycle of (a) sea surface temperature, (b) 10-m wind speed and relative humidity, and (c) high and low cloud fraction, and clear-sky radiation at 6°S, 8°E. Shading represents the standard error of monthly averaged terms fit to the seasonal cycle.

Turbulent heat fluxes are estimated using the Coupled Ocean-Atmosphere Response Experiment version 3.5 bulk flux algorithms (Fairall et al., 2003). Version 3.5 has improved parameterizations of the surface roughness and drag coefficients used to estimate surface stress from bulk formulas (Edson et al., 2013). Latent heat flux is dependent on surface humidity, wind speed, air temperature, and SST, $Q_{lhf} = \rho_a L_E C_L \{W\Delta q\}$, where ρ_a is the air density, L_E is the latent heat of vaporization, C_L is the transfer coefficient, W is wind speed, and Δq is the difference between surface saturation at the sea surface and air humidity. Sensible heat flux relies on wind speed and the temperature difference between the sea surface and atmosphere $Q_{shf} = \rho_a C_p C_s \{W\Delta T\}$, where C_p is the specific heat capacity of air, C_s is the transfer coefficient, and ΔT is the air-sea temperature difference.

We define the depth of the ocean mixed layer based on a density difference from a near-surface reference level. This definition takes into consideration the influence of salinity on upper ocean stratification. When a shallow halocline persists above a deeper thermocline, barrier layers can form that prevent mixing between the surface mixed layer and thermocline waters (Foltz & McPhaden, 2009). The barrier layer is a region between the thermocline and surface mixed layer that decouples the two regions by limiting vertical turbulent transfers between them. When barrier layers exist, the mixed layer defined in terms of temperature alone results in an overestimation of the true mixed layer depth. Thus, we use the mixed layer depth definition according to Sprintall and Tomczak (1992), $\sigma_t(h) = \sigma_t(h_r) + \Delta T \frac{\partial \sigma_t(h_r)}{\partial T}$, where the mixed layer depth (h) is defined where the density (σ_t) at 1-m reference level (h_r) increases to a density equivalent of a 0.3 °C temperature change (ΔT) (Figure 1.3). Our choices for h_r and ΔT were

chosen based on sensitivity analyses with different values. The mixed layer is most sensitive to the reference level, and 1 m is chosen because the mixed layer can be as shallow as 5 m and it is a non-interpolated depth value measured directly at the mooring. A temperature change of 0.3 °C is equivalent to a 0.08 kg/m^3 density increase and is consistent with other heat budget studies (e.g., Foltz et al., 2013).

The vertical resolution of PIRATA temperature and salinity measurements used to compute mixed layer depth varies from 2 to 10 m in the upper 20 m of the water column. Seasonal fluctuations in mixed layer depth are found to be small and on the order of 5 m. To understand the sensitivity of the mixed layer depth calculation to vertical resolution, we use 186 higher vertical resolution Argo profiles within ±2° latitude and longitude of the PIRATA mooring (see Appendix A). We find that coarser vertical resolution of PIRATA data yields mixed layers that are on average about 20% too shallow. We therefore correct the PIRATA-derived mixed layer depths using a regression equation based on comparison with the Argo data and use this adjusted mixed layer depth throughout the remainder of the paper (Figure A1.1).

We use the zonal and meridional velocity measurements from the at 10-m current meter to compute horizontal advection in the mixed layer. We assume that the velocity at 10 m is representative of the mixed layer, which varies between 5 and 15 m, recognizing that there are times when 10 m is just below the mixed layer. We approximate the horizontal gradients in mixed layer temperature using the satellite derived daily optimum interpolation SST data set that has a 0.25° latitude by 0.25° longitude resolution (Reynolds et al., 2007). We take horizontal

gradients of optimum interpolation SST using a centered difference over ± 0.375° latitude and longitude domain centered at 6°S, 8°E. The horizontal scale for this calculation was chosen based on the time that a water parcel would take to travel across this distance at the observed velocity. Horizontal current velocities at 6°S, 8°E have a standard deviation of 13.4 km/day zonally and 11.2 km/day meridionally so that it would take a water parcel approximately 1 week to advect through this region.

The residual heat flux (ε) represents the combination of accumulated instrumental, sampling, and computational errors in the explicitly resolved terms plus any neglected physical processes, the most important of which are vertical turbulent transfers of heat involving diffusion and/or entrainment across the base of the mixed layer (Foltz et al., 2003). Turbulent processes cannot be directly measured from the buoy data. However, the upper bounds can be estimated by assuming that ε is all due to turbulence rather than any noise contamination (McPhaden, 1982; Wang & McPhaden, 1999). For the sake of argument, we will further assume the turbulent processes involve entrainment of thermocline water across the base of the mixed layer although it is also possible that diffusive processes may be operative as well. With these assumptions, the upper bound on turbulent entrainment velocity (W_e) is given by

$$W_e = -\frac{\varepsilon}{\rho_0 C_p \delta T} \tag{4}$$

where (δT) is the temperature difference between the mixed layer and a depth 20 m below the mixed layer (Chang, 1993).

Terms in equations 1–4 are computed using daily data smoothed with a 7-day triangle filter to eliminate high frequency variability (Figure 1.7). Daily data are then fit to mean, annual, and semiannual harmonics to define the seasonal cycle. Sampling errors are expressed as 1 standard error from this fitting procedure.

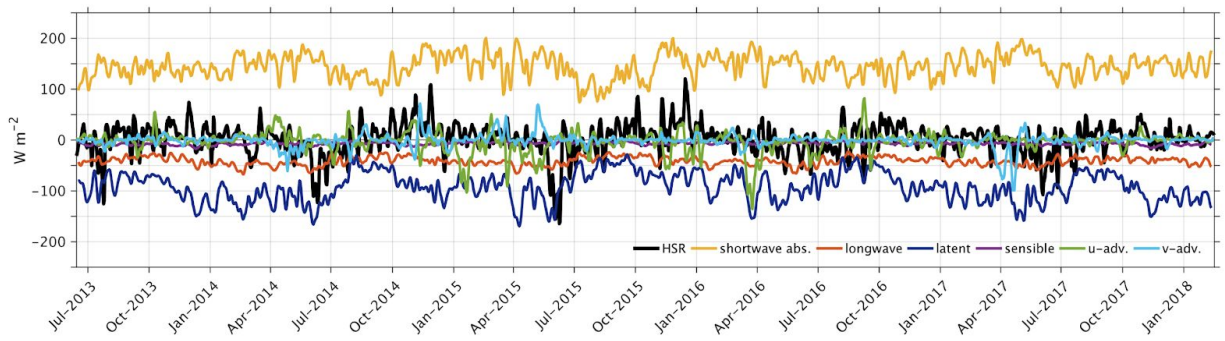

Figure 1.7 Components of the mixed layer heat balance at 6°S, 8°E from Prediction and Research Moored Array in the Atlantic-Southeast Extension. Daily data are smoothed temporally with a 7-day triangle filter to eliminate high frequency variability. The components that balance the total heat storage rate (HSR) are absorbed shortwave and net longwave radiation, latent and sensible turbulent heat flux, and zonal (u-adv) and meridional (v-adv) heat advection. Positive terms are interpreted as heating the ocean mixed layer and negative terms as cooling.

1.4 Results

In the following section, we describe the seasonal variability of various processes that affect the surface layer heat balance followed by a detailed examination of the terms in the balance itself at the 6°S, 8°E PIRATA buoy. We begin with a description of the vertical structure of upper ocean temperature and salinity, which is dominated by the annual and semiannual cycles (Figures 1.4c and 4d). The base of the mixed layer exhibits a semiannual cycle with shoaling during the boreal winter and summer over a vertical depth range of less than 5 m (solid black lines in Figures 1.4c and 4d). Early in the year, the mixed layer warms and freshens in response to high austral

summer insolation and precipitation (Figures 1.4a and 1.4b) as the ITCZ moves toward its southernmost latitude (Figure 1.1).

Surface salinity influences the processes controlling mixed layer temperature through changes in mixed layer density and depth. Near-surface freshening during the boreal spring forms a shallow halocline above the seasonal thermocline that can produce barrier layers where the mixed layer based on density is shallower than the isothermal layer. Barrier layer thickness is defined as the difference between the mixed layer and isothermal layer as, for example, illustrated in Figures 1.3 and 1.4c and 1.4d. Barrier layers can limit the mixing of cold thermocline waters into the near-surface layer; however, we find that when averaged to seasonal timescales, the thickness of the barrier layer in boreal spring is thin (Figures 1.4c and 1.4d); moreover, the difference between the mixed layer and isothermal layer is not statistically significant. Thus, on seasonal timescales, barrier layers most likely do not have a large effect, though barrier layers may play a more significant role on subseasonal timescales (e.g., Figure 1.3).

During the boreal summer, SST rapidly decreases coincident with a reduction in shortwave radiation due to a seasonal maximum in solar zenith angle and the expansion of the stratocumulus cloud deck (Figures 1.4a and 1.6c). Low-level stratocumulus clouds form over cold surface water and reflect sunlight back to space, significantly reducing solar radiation at the surface. Marine stratocumulus clouds that form over cold water thus further cool SSTs in the boreal summer. Cold SST in turn increases the stability of the marine boundary layer and confine

low-level and highly reflective marine stratocumulus clouds to the lower troposphere near the descending branch of the Hadley Cell (Wood, 2012).

The stratus deck in the southeastern tropical Atlantic is prominent only in the boreal summer, so that insolation exhibits a primarily 1 cycle per year variation with a minimum in boreal summer (Figure 1.4a) even though clear-sky radiation shows a 2 cycle per year variation (Figure 1.6c; see also Li & Philander, 1997). However, the amount of solar radiation absorbed by the ocean mixed layer is also dependent on the optical properties of the water. During summer, surface chlorophyll-*a* concentrations are maximum in July when upwelling brings cold, nutrient-rich water to the sea surface and boosts biological productivity (Figure 1.5). An abundance of phytoplankton that contain chlorophyll absorb and scatter shortwave radiation within the mixed layer and decrease the amount of penetrative radiation escaping the base of the mixed layer (Figure 1.5). Thus, phytoplankton change the optics of the upper ocean during the boreal summer thereby increasing the attenuation of solar radiation with depth.

Latent heat flux is dependent on wind speed as well as the difference between the saturation specific humidity of the sea surface and the specific humidity of the air just above. This air-sea humidity difference is large when the relative humidity of the air is low and vice versa. In May and June, a weak seasonal minimum of relative humidity (78%) and maximum in wind speed (5 m/s) increase evaporation at the sea surface and enhance cooling in the mixed layer (Figure 1.6b). Conversely in September, a maximum in relative humidity above the sea surface (84%) coincides with a minimum in wind speed (4.1 m/s) that reduces the efficiency of evaporative

cooling at the sea surface. These predominantly semiannual variations of wind speed and annual variations in relative humidity lead to both annual and semiannual variations in latent heat loss, with a pronounced minimum in heat loss during August–October (Figure 1.8a).

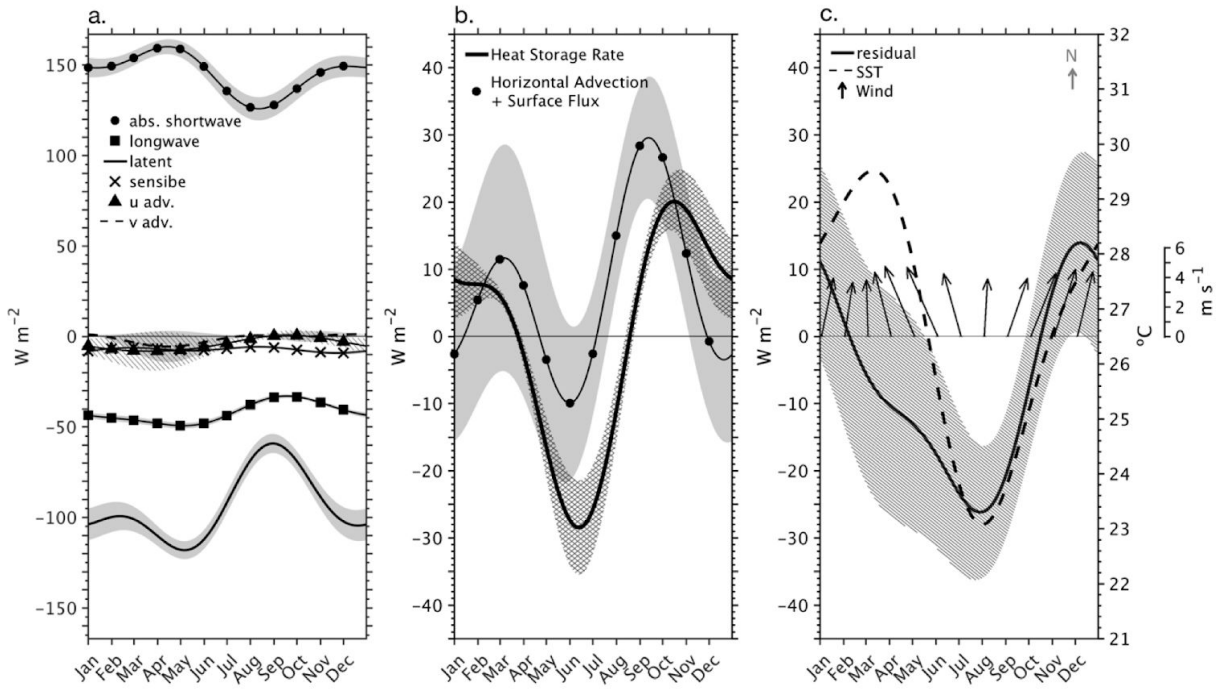

Figure 1.8 Seasonal mixed layer heat balance at 6°S, 8°E at the Prediction and Research Moored Array in the Atlantic-Southeast Extension. (a) The mean seasonal cycle of the different components in the surface mixed layer heat balance, (b) total heat storage rate and sum of horizontal advection (u-adv and v-adv) and surface flux (absorbed shortwave, longwave, latent, and sensible), and (c) residuals computed as the total heat storage rate minus the sum of horizontal advection and surface flux terms, sea surface temperature, and wind speed and direction. Shading representing uncertainty computed as one standard error of monthly values fit to the seasonal cycle.

Sea surface salinity reaches a seasonal maximum during the late boreal summer coincident with a minimum in SST (Figure 1.4c). The seasonal peak in surface salinity is enhanced by the northward displacement of the ITCZ that reduces freshwater supply from local precipitation and river runoff at this time (Figure 1.1). The mixed layer and isothermal layer shoal in boreal summer are coincident with a rapid upwelling of the thermocline (Figure 1.4c). Upwelling

advects cold, saline thermocline water toward the surface where it can be entrained into the mixed layer. The depth of the thermocline can be estimated by the 20 °C isotherm, which has both annual and semiannual components that varies from a depth of 19–40 m (Figure 1.4c, white line). Local winds do not appear to drive this upwelling, since winds that are southerly all year (Figure 1.8) have their minimum speeds during this season (Figure 1.6b). Cold SSTs stabilize the atmospheric boundary layer in the boreal summer by minimizing the downward vertical atmospheric momentum flux, which results in weaker surface winds (Hayes et al., 1989; Wallace et al., 1989). As SSTs warm, atmospheric stratification erodes allowing more efficient mixing between the boundary layer and the free atmosphere, causing the southeasterly trades to intensify (Hayes et al., 1989). These wind field variations in relation to SST have been observed in the cold tongue regions of the equatorial Pacific (Wallace et al., 1989) and Atlantic (De Coëtlogon et al., 2013) and are evident in the relation of wind speed (Figure 1.6a) to the seasonal cycle of SST (Figure 1.4c) at 6°S, 8°E.

Remote wind forcing rather than local wind forcing is most likely responsible for driving upwelling at this location. Yamagata and Iizuka (1995) have pointed out that semiannual relaxation of the trade winds west of 30°W will generate downwelling Kelvin waves that propagate eastward into the Gulf of Guinea deepening the thermocline there in March and November. In addition, easterly trade winds intensify in boreal summer in the central equatorial Atlantic as the ITCZ migrates northward forcing an eastward propagating upwelling Kelvin wave (Weisberg & Tang, 1990). The buoy at 6°S, 8°E is situated off the equator in a region of maximum amplitude for first meridional mode Rossby waves that would be generated from the

boundary reflection of remote wind-driven equatorial Kelvin waves (Ding et al., 2009). The superposition of remotely forced and reflected longwave most likely explains the seasonal variations in thermocline depth at 6°S, 8°E.

We now turn to the specifics of how the heat storage rate in the mixed layer is influenced by horizontal advection, surface radiative and turbulent heat fluxes, and vertical turbulent processes (Figure 1.8). Absorbed shortwave radiation and latent heat loss are the largest terms in the surface energy balance and have a pronounced seasonal cycle (Figure 1.8a). The seasonal cycle of latent heat flux due to evaporation is out of phase with absorbed shortwave radiation and cools the mixed layer more strongly in the boreal spring than summer. Sensible heat flux cools the mixed layer throughout the year but is less than −10 W/m^2 with a negligible seasonal cycle. Net longwave radiation is nearly constant at −40 W/m^2 and also has a small seasonal cycle (Figure 1.8). Horizontal advection has a weak seasonal cycle that is not distinguishable from zero within the error bounds (Figure 1.8a).

The sum of the terms calculated here does not balance the rate of heat storage. There is missing a source of cooling in the boreal summer indicated by significant negative residuals in June through September ranging from −17.4 W/m^2 to −26.2 W/m^2 (solid back line in Figure 1.8c). We interpret these residuals as due to turbulent entrainment. Using vertical temperature changes at the base of the mixed layer, we determine how large turbulent entrainment velocity would need to be to account for the residual heat flux during these months. We find that the largest residuals (July and August) are associated with relatively small vertical temperature gradients and

significant W_e values (Figure 1.9). The maximum seasonal W_e occurs in August coincident with the largest negative residual in the mixed layer heat balance (Table 1.1). This suggests that vertical entrainment processes are likely to be important to the mixed layer heat balance during the boreal summer months and plausibly explain the missing source of mixed layer cooling during this time of year. These results are consistent with the mixed layer heat balance by Foltz et al. (2003) at 0°, 10°W who showed the residual heat flux in summer was as large as ~100 W/m^2 and that entrainment, calculated as the mass flux across the base of the mixed layer, was most important during the boreal summer. Similarly, in Wang and McPhaden (1999) the residual heat budget flux in the eastern equatorial Pacific at 0°, 110°W was as large as ~120 W/m^2 during the boreal summer, which is ~5–10 times larger than found here. Interpreted as entrainment, their estimate of W_e was likewise 10 times larger than ours. One explanation for these differences is that upwelling and entrainment on the equator are more vigorous in the cold tongue region than at 6°S so that both heat budget residuals and estimates of W_e are smaller at the PIRATA-SEE site.

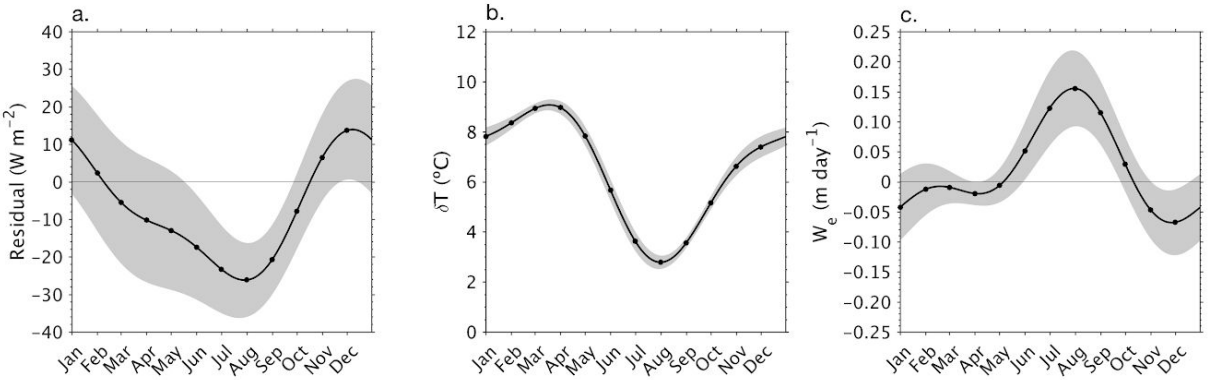

Figure 1.9 Seasonal cycle of the (a) mixed layer heat budget residuals (replotted from Figure 1.8c), (b) vertical temperature difference between the mixed layer and 20-m below the base of the mixed layer (δT), and (c) inferred turbulent entrainment velocity (W_e) across the base of the mixed layer. Light shading represents 1 standard error.

Table 1.1 Monthly Significant Negative Non-zero Residuals in the Mixed Layer Temperature Balance at 6°S, 8°E, Temperature Difference Between the Mixed Layer and 20 m Below the Base of the Mixed Layer (δT), and the Turbulent Entrainment Velocity (W_e) Across the Mixed Layer

	June	July	August	September
Residual (W/m^2)	−17.43 ± 16.49	−23.27 ± 8.93	−26.16 ± 10.57	−20.73 ± 9.76
δT (°C)	5.66 ± 0.48	3.63 ± 0.21	2.78 ± 0.33	3.56 ± 0.25
W_e (m/day^1)	0.05 ± 0.05	0.12 ± 0.06	0.16 ± 0.06	0.12 ± 0.05

Note. Uncertainty is displayed as 1 standard error based on deviations from the mean seasonal cycle.

1.5 Summary

In this study we examined the seasonal mixed layer heat balance in the southeast tropical Atlantic using 5 years of observations collected from the PIRATA-SEE mooring at 6°S, 8°E, combined with satellite and reanalysis data. Our purpose was to determine the factors responsible for the seasonal evolution of mixed layer temperature. We found that the seasonal evolution of mixed layer temperature has two pronounced regimes: a warm-fresh regime (December–April) and a cold-salty regime (May–September).

The warm-fresh regime (December through April) is characterized by high surface shortwave radiation and precipitation that increase near-surface stratification, leading to a shallow mixed layer. Solar heating is very efficient in warming SST at this time since heat is trapped in a relatively thin mixed layer. Warming and freshening of the mixed layer is associated with a southward migration of the ITCZ that increases local precipitation and river runoff from the Congo River. The mixed layer is warmed primarily through shortwave radiation, which reaches

maximum values in austral fall at this location. Conversely, horizontal advection from the poleward flowing Angola Current contributes little to the heat balance at this location.

The mixed layer transitions to cool and salty during the boreal summer (May through September) when the equatorial cold tongue develops. This cool and salty regime is driven by the intensification of the southeasterly Trades in response to the onset of the West African Monsoon and the displacement of the ITCZ further north (Mitchell & Wallace, 1992). The strengthened Trades enhance local evaporative cooling and upwelling along the African coast as well as along and south of the equator. The mixed layer shoals in August when cold and salty thermocline water is entrained into the mixed layer. Cool SSTs stabilize the shallow stratocumulus cloud deck along the eastern boundary, shielding the ocean surface from downwelling shortwave radiation, which is a minimum at this time of year. The mixed layer gradually warms and freshens following this period through processes controlled by the position of the sun overhead and southern migration of the ITCZ.

The residuals of the explicitly calculated terms in the heat budget include various sources of error and neglected physical processes, the most important of which is related to vertical turbulent mixing. We attribute the residual cooling in the mixed layer during June through August primarily to vertical turbulent entrainment enabled by upwelling favorable conditions at this time (e.g., Camara et al., 2015; Da‐Allada et al., 2013; Tzortzi et al., 2013). The residual heat flux in June through September and inferred entrainment velocities are about 5–10 times smaller than found right on the equator in the eastern Pacific and Atlantic, consistent with the

notion that upwelling and entrainment during the boreal summer are more vigorous on the equator than at the poleward margins of the equatorial cold tongue.

Our results are consistent with previous studies that found that surface fluxes dominate the annual cycle of SST off the equator, while ocean dynamics play a more important role near the equator between 5°S and 10°N (Carton & Zhou, 1997; Foltz et al., 2003; Yu et al., 2006). Our results also suggest that precipitation is an important component toward understanding the heat balance in the eastern tropical Atlantic since the freshwater flux into the ocean leads to shallow mixed layers in the early part of the calendar year. This work motivates collection of temperature, salinity, and velocity observations with finer vertical resolution in the upper ocean to more accurately document and understand the physical processes involved.

These findings indicate that the distribution of SST is highly sensitive to surface fluxes in the southeastern tropical Atlantic where the most severe climate model biases occur. In particular, absorbed shortwave radiation is dependent on low-level cloud cover, which is often misrepresented in climate models. An underestimation of the stratocumulus cloud deck allows excessive absorption of shortwave radiation to reach the sea surface and contributes strongly to the SST warm biases in the eastern tropical Atlantic (Zuidema et al., 2016).

Previous evaluations of coupled climate models suggest that a variety of factors are involved in creating these SST biases. Goubanova et al. (2018) and Patricola et al. (2012), for example, point to an equatorial westerly wind bias as the major contributor to incorrect thermocline depth

representation and its influence on SST in the eastern tropical Atlantic. Harlaß et al. (2018) showed that models with high horizontal and vertical atmospheric resolution had improved wind structure that correctly simulated the development of the equatorial cold tongue during the boreal spring and summer by allowing more realistic thermocline depth variation and latitudinal position of the ITCZ. However, higher atmospheric resolution alone does not completely eliminate SST biases in coupled climate model simulations of the tropical Atlantic (Doi et al., 2012), suggesting that improved cloud parameterizations are important for improving the simulation of cloud radiative feedbacks and their effects on SST. To quantify the significance of various factors in coupled climate models that lead to systematic warm biases in the eastern tropical Atlantic, model-based mixed layer heat budget analyses complimentary to that presented in this paper need to be undertaken in a future study.

Chapter 2

SUBSURFACE EVOLUTION AND PERSISTENCE OF MARINE HEATWAVES IN THE NORTHEAST PACIFIC

2.1 Abstract

The reappearance of a northeast Pacific marine heatwave (MHW) sounded alarms in late summer 2019 for a warming event on par with the 2013–2016 MHW known as The Blob. Despite these two events having similar magnitudes in surface warming, differences in seasonality and salinity distinguish their evolutions. We compare and contrast the ocean's role in the evolution and persistence of the 2013–2016 and 2019–2020 MHWs using mapped temperature and salinity data from Argo floats. An unusual near-surface freshwater anomaly in the Gulf of Alaska during 2019 increased the stability of the water column, preventing the MHW from penetrating deep as strongly as the 2013–2016 event. This freshwater anomaly likely contributed to the intensification of the MHW by increasing the near-surface buoyancy. The gradual buildup of subsurface heat content throughout 2020 in the region suggests the potential for persistent ecological impacts.

2.2 Introduction

Marine heatwaves (MHWs) have become distinguishable features of northeast (NE) Pacific Ocean temperature variability that disrupt the productivity of marine ecosystems and their

services (Smale et al., 2019). These prolonged, discrete, and anomalously warm water events (Hobday et al., 2016) are most recognizable at the sea surface and are influenced by anthropogenic warming (Laufkötter, et al., 2020). The effects of long-term ocean warming have led to a near-doubling in the average annual count of MHW days globally since the early 20th Century (Oliver et al., 2018). Although MHWs have occurred throughout the global ocean, the NE Pacific has recently emerged as a hotspot for extremely persistent and large-scale events that are forced by anomalous air-sea heat flux driven by remote forcing from the tropics (Di Lorenzo and Mantua, 2016; Holbrook et al., 2019), in addition to long-term warming from anthropogenic greenhouse forcing (Laufkötter, et al., 2020). The most remarkable NE Pacific MHWs have occurred in 2013–2016 and 2019–2020, and are colloquially referred to as The Blob (Bond et al., 2015) and Blob2.0 (Amaya et al., 2020) respectively (Figure 2.1 and Figure 2.3).

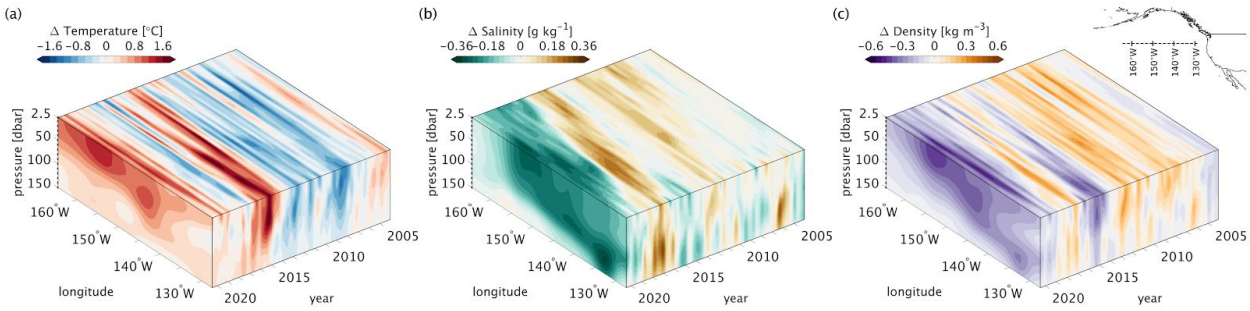

Figure 2.1 Subsurface evolution and vertical structure of (a) conservative temperature, (b) absolute salinity, and (c) potential density anomalies in the Northeast Pacific vs time (January 2004 through June 2020), pressure (2.5 to 150 dbar) and longitude (164.5–127.5 ºW) at 44.5 °N; see map inset. The objectively mapped Roemmich-Gilson Argo Climatology is used (Roemmich and Gilson, 2009). Anomalies are computed with respect to the January 2004 through June 2020 monthly means.

The magnitude of sea surface temperature (SST) anomalies associated with MHWs depends critically on the seasonal evolution of the mixed-layer depth (MLD), which deepens in winter

and shoals in summer. If winter mixed layer MHW anomalies are present in the early spring when the mixed layer shoals, they can become trapped in the subsurface during the summer through detrainment. These detrained temperature anomalies are then stored in the subsurface and can reemerge the following winter when the mixed layer deepens and re-entrains them (Alexander and Deser, 1995; Alexander et al, 1999; Alexander et al., 2001). Alternatively, in the presence of downward Ekman pumping from wind stress curl, for example in the North Pacific subtropical gyre, detrained anomalies can subduct, where they are further isolated from the mixed layer (Qiu and Huang, 1995). Here, we explore the role of detrainment and subduction in the sequestration of MHW anomalies into the permanent pycnocline where they can persist for years.

The evolution of the 2013–2016 NE Pacific MHW was complex and shaped by multiple drivers. Warm SST anomalies first appeared in the southern Gulf of Alaska centered on 40°N and 150°W and subsequently developed along the coast and south into the Southern California Current System near 25°N. In the Gulf of Alaska, lower rates of turbulent heat loss during the winter of 2013–2014 from the ocean to atmosphere and a reduction in wind-generated stirring allowed the winter mixed layer to remain unseasonably warm and shallow (Bond et al., 2015). The MWH transitioned to the south owing to local positive downward shortwave radiation anomalies and a positive SST-cloud feedback over the Southern California Current System that reinforced surface warming near the coast in 2014 (Zaba and Rudnick, 2016; Myers et al., 2018; Schmeisser et al., 2019). Below the mixed layer, anomalously warm and salty water was detrained to denser and deeper isopycnals, reaching depths of 140 m beginning in 2014 (Jackson et al., 2018). These

subsurface anomalies lingered through at least 2018, long after the initial onset of atmospheric forcing in late 2013.

A similar situation played out during the summer of 2019 when a resurgence of Blob-like surface conditions intensified in the NE Pacific. Weakened surface wind speeds, driven by atmospheric teleconnections associated with SST anomalies in the Tropical Pacific, resulted in reduced evaporative heat loss from the ocean to atmosphere and limited wind-driven mixing, resulting in a MHW off the U.S. West Coast (Amaya et al., 2020). Increased shortwave radiation and a positive SST-cloud feedback helped to maintain the MHW over an exceptionally shallow summertime mixed layer (Amaya et al., 2020). Here, we show evidence for the role of salinity anomalies in increasing upper ocean stability, and describe the propagation and persistence of the 2019–2020 NE Pacific MHW in the subsurface.

In this study, we examine the connections between surface MHWs and the subsurface structure of temperature, salinity, and density by analyzing objectively mapped monthly Argo data in the NE Pacific, comparing and contrasting the 2013–2016 and 2019–2020 MHWs. We characterize the spatiotemporal evolution of anomalous subsurface conditions and their connection to mixed layer properties from January 2004 through June 2020, and we quantify the change in water mass properties and ocean heat content anomalies within and below the mixed layer. Understanding the subsurface evolution and persistence of MHWs gives insight into the potential predictability and reemergence of these events in the future, where a trend towards shallower summertime MLDs is expected to increase the likelihood and intensity of MHWs in the North Pacific (D.J.

Amaya, personal communication, 2020). The persistence and potential reoccurrence of MHWs could result in long-lasting impacts on the health of marine ecosystems, especially in the subsurface where the effects of warming on marine life (i.e., thermal stress) can persist for years (Cavole et al., 2016).

2.3 Data

We analyze monthly mean SST maps from the Optimum Interpolation SST version 2 (OISSTv2) dataset on a 0.25° longitude by 0.25° latitude global grid from 1982 through present (Reynolds et al., 2002; 2007). These SST maps are generated from a blend of satellite (Advanced Very High Resolution Radiometer only), ship, buoy (both moored and drifting), and Argo float data. The satellite data are interpolated to fill gaps and are bias corrected with reference to buoys to account for platform differences. We use the OISSTv2 dataset as it incorporates *in situ* observations, offers complete global coverage, and spans almost 40 years.

We also analyze monthly mean fields from January 2004 through June 2020 from the updated Roemmich-Gilson Argo Climatology (Roemmich and Gilson, 2009; hereafter RG09) to examine the vertical structure of temperature, salinity, and density anomalies associated with MHWs. Argo is a global network of autonomous profiling floats that continuously measures the temperature and salinity of the upper 2,000 m of the ocean. The Argo program began in 1999 and now consists of over 3,800 active floats and more than 2 million hydrographic profiles reported thanks to a coordinated effort from dozens of countries worldwide (Jayne et al., 2017).

Archived and near real-time float data are made publicly available (http://sio-argo.ucsd.edu/RG_Climatology.html) and are incorporated into monthly maps on a 1° longitude by 1° latitude grid beginning in January 2004 when the global array had at least 1,000 floats and first approached sparse global coverage (RG09). These maps are made in 58 pressure layers with the shallowest centered on 2.5 dbar and the deepest on 1,975 dbar, with finer resolution near the surface (e.g., spaced 10 dbar apart from 10 to 170 dbar). The 2.5 dbar monthly temperature anomalies in RG09 closely track the monthly OISSTv2 anomalies in the NE Pacific, capturing large scale spatial and temporal variability.

In addition to the mapped temperature and salinity vs. pressure fields from RG09, we also analyze 19,697 quality-controlled Argo profiles in the NE Pacific (35.5–51.5°N, 135.5–154.5°W; box in Figure 2.3) to compute the MLD from January 2004 through June 2020 using the density algorithm of Holte and Talley (2009). The sampling frequency from Argo in the NE Pacific (35.5–51.5°N, 135.5–154.5°W) steadily increases from the early 2000s, achieving over 1,000 profiles per year starting in 2012 (Figure 2.2). These profiles were downloaded from one of the two Argo Global Data Assembly Centers (https://nrlgodae1.nrlmry.navy.mil/argo/argo.html) in August 2020.

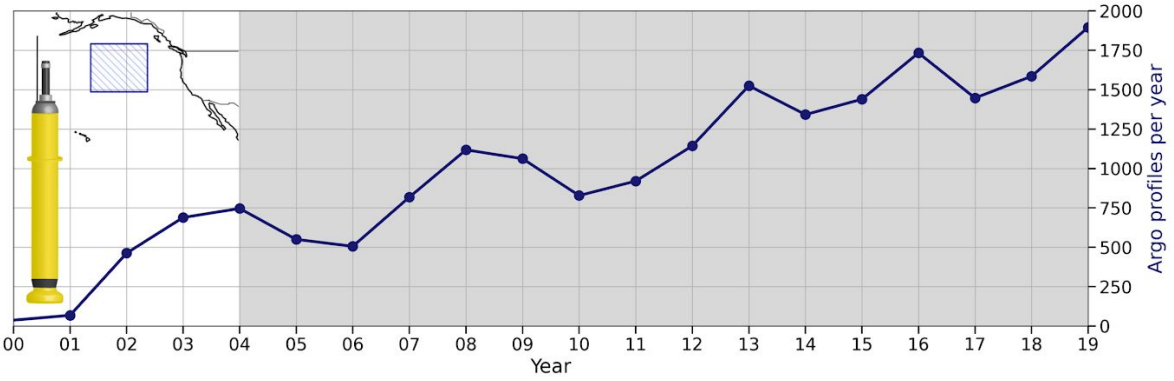

Figure 2.2 Number of Argo float profiles in the NE Pacific (35.5–51.5ºN, 135.5–154.5ºW; blue boxed region in map inset). Years shaded in gray are used in this analysis and overlap with the Roemmich-Gilson Argo Climatology. We use 19,697 profiles from January 2004 through June 2020. An illustration of a core Argo float is shown measuring 1.3 m in height, 20 cm wide, and approximately 40 kg in weight. These autonomous floats profile the upper 2,000 m on 10-day intervals and measure ambient seawater salinity, temperature, and pressure. The schematic of an Argo float is provided by the Argo Program (https://www.argo.ucsd.edu).

2.4 Analysis

We define MHWs locally when SST exceeds the monthly climatological 90th percentile for at least a month using monthly data from January 2004 through June 2020. Our definition for MHWs is similar to that proposed in Hobday et al. (2016) with modifications in the length of the climatological period and in the minimum event duration. Owing to the prominence and persistence of the 2013–2016 and 2019–2020 MHWs, our definition highlights the same large-scale features described in previous studies using daily data (e.g., Gentemann et al., 2017; Fewings and Brown, 2019).

Before analyzing the RG09 dataset, we fit temperature and salinity at each spatial point to a mean, trend, annual, and semiannual harmonics using least squares regression from January 2004

through June 2020. We then remove the mean, annual, and semi-annual harmonics (but not the trend) to generate anomalies. Following MHW conventions (e.g., Hobday et al., 2016), we choose to retain the warming trend in the analysis using a fixed climatology computed over the entire record. Furthermore, the trend would not be accurately estimated over such a short period and would be extremely biased by the 2013–2016 and 2019–2020 MHWs at one end of the time-series. Finally, detrending would effectively remove part of the strong MHW signal that we observe towards the latter end of the record. We therefore retain it. Next, we smooth the anomalies and the regression coefficients with a 5-month Hanning filter and then a 6° latitude x 6° longitude LOESS filter to reduce mesoscale signals that are retained in the RG09 maps. We then reconstruct the total smoothed *in-situ* temperature and practical salinity maps using the smoothed anomalies and smoothed model coefficients. We apply the thermodynamic equation of seawater (Intergovernmental Oceanographic Commission et al., 2010) to compute the absolute salinity (S_A) and conservative temperature (Θ) at each space and time grid point. Using S_A and Θ, we also compute the potential density anomaly (σ_θ) with reference to 0 dbar; expressed as a particular potential density minus 1000 kg m^{-3}. The potential density represents the density a fluid parcel would acquire if it were brought adiabatically to the sea surface, thus eliminating the density dependence on pressure. We also map the RG09 fields of S_A, Θ, and pressure (P) to a vertical density coordinate, σ_θ. We compute anomalies in S_A, Θ, and P in σ_θ coordinates, as well as S_A, Θ, and σ_θ in P coordinates, by removing the monthly means of these quantities across the entire 198-month time series at each spatial point and for each vertical coordinate system (σ_θ and P) to get the anomalies. We describe changes in S_A, Θ, and P on an isopycnal (25.4 kg m^{-3}) that may outcrop during winter. When isopycnals outcrop their properties are easily

modified through air-sea interactions that may drive surface MHWs. Once isopycnals subduct below the mixed layer, their properties can be modified through mixing and/or lateral advection, which is usually less effective than direct air-sea heat and freshwater exchange.

We examine the ocean heat content anomaly (Q') within the mixed layer (10–90 dbar), thermocline (100–180 dbar), and just below the thermocline (200–280 dbar). These layers of equal thickness are chosen based on the vertical profiles of subsurface temperature in the NE Pacific (Figure 2.8b). They typify the surface, pycnocline, and interior ocean in the region, allowing for the distinction of the changes in Q' with depth. We define $Q' = \int 1/g \cdot c_p \cdot \Theta' dp$, where $g = 9.8\ ms^{-2}$ is the acceleration due to gravity, $c_p = 3991.8680\ J\ kg^{-1}K^{-1}$ is the standard specific heat of seawater when using Θ, Θ' is the conservative temperature anomaly, and $\int dp$ is the integral over each of these three 80-dbar thick layers.

We apply the Holt and Talley (2009) density algorithm to 19,697 Argo float profiles in the NE Pacific (35.5–51.5ºN, 135.5–154.5ºW; box in Figure 2.3) to estimate monthly MLDs from January 2004 through June 2020. This method searches for the depth at which the density increases by 0.03 kg m^{-3} relative to a near-surface reference level.

We quantify the bulk stratification of the upper ocean using the Brunt-Väisälä frequency squared $N^2 = -\frac{g}{\rho}\frac{d\rho}{dz}$. Here, $\frac{d\rho}{dz}$ is the change in potential density with reference to 0 dbar between 2.5 and 200 dbar. Large values of N^2 correspond to greater upper ocean stratification — a more stable

water column. We compute anomalies in N^2, again with respect to monthly long-term means, to quantify the change in the stratification of the upper ocean due to MHW variations in both Θ and S_A.

To further examine the relationships among Θ, S_A, and σ_θ, we examine $\Theta - S_A$ diagrams with contours of constant density and spice to show changes in water-mass properties between different MHW years in the NE Pacific. Spice quantifies $\Theta - S_A$ variations along isopycnals (Munk, 1981), where warm/salty anomalies are spicy and cool/fresh anomalies are minty. We compute spice following McDougall and Krzysik (2015) using a potential density with reference to 0 dbar. Isopycnal variations in spiciness can be used to describe MHW impacts on isopycnal water-mass properties in density units.

2.5 Results

Anomalies in $\Theta - S_A$ on isopycnals can be tracked following the surface evolution of SST anomalies during MHWs, and can either be warm/salty (spicy) or cool/fresh (minty), such that the density of that isopycnal does not change. The winter-intensified 2014–2016 MHW had spicy anomalies on 25.4 kg m^{-3}, which lagged the spatiotemporal evolution of SST anomalies within the MHW (hatching in Figure 2.3). For example, surface MHW conditions appeared nearshore by late 2014 and began to fade as early as 2015, whereas subsurface spice anomalies did not reach the coast until winter 2015 and persisted into 2016. By comparison, summer $\Theta - S_A$ anomalies in 2019 lacked the transitional nature of the 2013–2016 MHW, yet they were much more widespread. Minty anomalies on 25.4 kg m^{-3} encompassed nearly the entire Gulf of Alaska

from late summer 2018 through summer 2020, while spicy anomalies lingered off the coast between Baja California and Hawai'i (Figure 2.3).

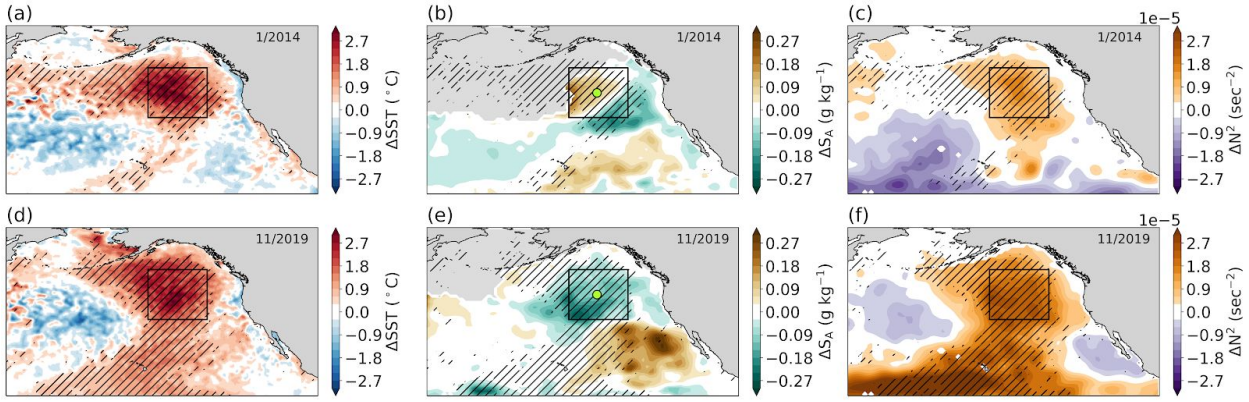

Figure 2.3 Spatial characteristics of NE Pacific MHWs during January 2014 (a-c) and November 2019 (d-f); the two warmest months of SST anomalies averaged in the boxed region from 2004 through 2020. First column (a,d) shows SST anomalies from the OISSTv2 where diagonal hatching indicates the locations experiencing a MHW. Hatching across columns is consistent. The middle column (b,d) is the absolute salinity anomaly on 25.4 kg m^{-3}. By definition, conservative temperature anomalies mirror salinity anomalies on isopycnals where conditions are either warm/salty or cool/fresh. The third column (c,f) shows the bulk upper ocean stability anomaly in terms of the Brunt-Väisälä frequency squared computed using the anomalous density difference between 2.5 and 200 dbar. All anomalies are referenced to the January 2004 through June 2020 monthly climatology. The bounding black box represents the area defined by 35.5–51.5ºN, 135.5–154.5ºW and the lime green circles in (b) and (c) mark 43.5ºN, 145.5ºW.

Positive stratification (N^2) anomalies occurred for both the 2013–2016 and 2019–2020 MHWs, however were much greater in 2019 (Figure 2.3). Warm and fresh near-surface anomalies in 2019 decreased density and increased the stratification (Figure 2.4), whereas in 2013–2016 the near-surface density reduction from a warm anomaly was partially offset by a salty anomaly. The increase in pressure along 25.4 kg m^{-3} beginning in 2018 reflects an increase in stratification even before the onset of the 2019 MHW (Figure 2.4). The 2019 large and positive stratification

anomaly likely inhibited the surface MHW from penetrating as deeply as the 2013–2016 MHW, and furthermore may have enhanced the surface build-up of heat.

Prior to 2013, two other noteworthy MHWs occurred in the NE Pacific from 2004–2005 and 2008–2009 (Figure 2.4). Warm subsurface Θ anomalies during these MHWs extended to depth beyond 100 dbar and anomalies at 25.4 kg m^{-3} were spicy, similar to that of the 2013–2016 event (Figure 2.4). Warm and salty anomalies reduced subsurface density and increased the stratification of the surface layer. The 2004–2005 MHW was more stratified than the 2008-2009 event owing to the larger surface density anomaly (Figure 2.4e and Figure 2.8b-c).

The simultaneous change in temperature from 0–200 dbar in 2008–2009 could have resulted from isopycnal heave, as indicated by the downward deflection of 26.3 kg m^{-3} (Figure 2.4a). Heave can occur in response to Ekman pumping due to wind stress curl that depresses the main thermocline (Bindoff and McDougall, 1994), or from other dynamic features such as large-scale Rossby waves (Xie et al., 2016) or eddies (Pegliasco et al., 2015). Positive pressure anomalies on 26 kg m^{-3} indicates a deepening of the thermocline in 2008–2009 at approximately 130 dbar (Figure 2.4f). These vertical isopycnal motions are nearly adiabatic. As seen from the conservation of water mass properties on the isopycnal (Figure 2.4b,d), there is little exchange of heat or salinity with the surrounding environment. As a result, warm and fresh anomalies in 2008–2009 occurred along the 150–200 isobars, however, were negligible on 26.3 kg m^{-3}, which ranges from 150–200 dbar (Figure 2.4).

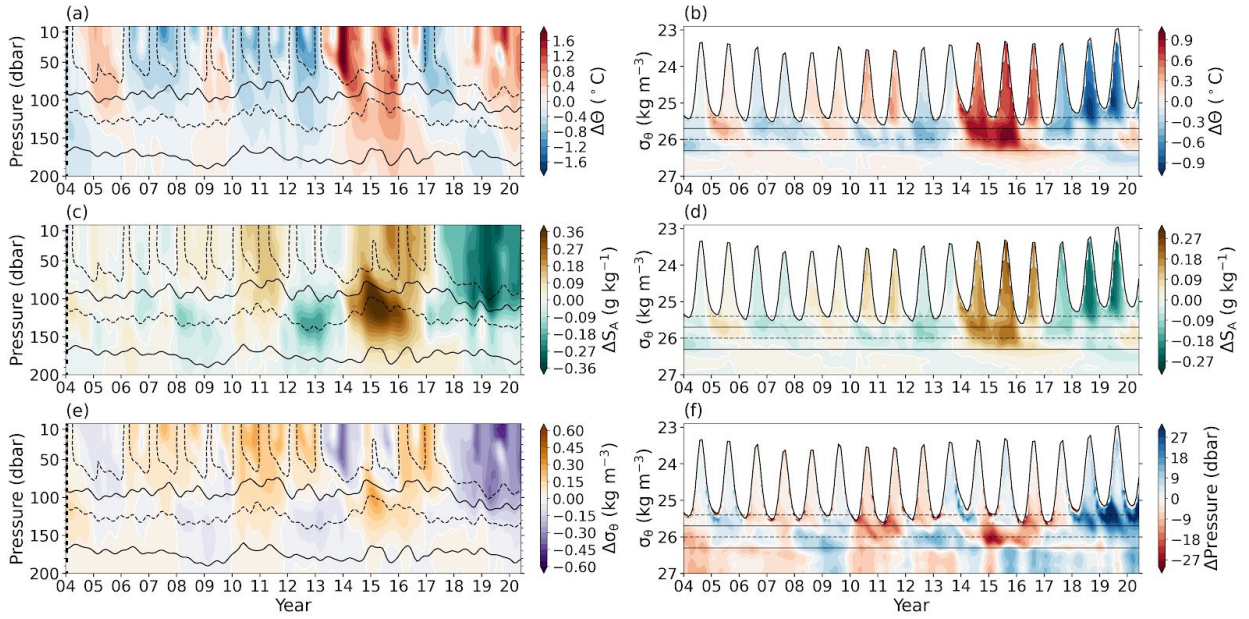

Figure 2.4 Progression of monthly anomalies in (a,b) conservative temperature, (c,d) absolute salinity, (e) potential density, and (f) isopycnal pressures at 43.5ºN, 145.5ºW (lime green circles in Figure 2.3) from January 2004 through June 2020. Contours of the 25.4 kg m^{-3} (upper dashed), 25.7 kg m^{-3} (upper solid), 26 kg m^{-3} (lower dashed), and 26.3 kg m^{-3} (lower solid) isopycnal surfaces vary with pressure (a,c,e), however are constant when plotted against density (b,d,f).

Analysis of $\Theta - S_A$ relationships along isopycnals provide additional insight into water-mass property changes during MHWs. Here, spice is primarily controlled by the exchange of heat and freshwater between the ocean and atmosphere, ocean turbulent mixing, and lateral advection. Spicy conditions occurred each winter (December-January-February) during the 2013–2016 MHW, most notably in waters lighter than 26.5 kg m^{-3} during the winters of 2014/15 and 2015/16 (Figure 2.5a). The warmest wintertime temperatures occurred in 2013/14 where $\Theta - S_A$ variations were confined to lighter isopycnals (<26 kg m^{-3}). Winter spice anomalies in 2013/14 likely mixed to denser isopycnals in the permanent halocline by summer, as can be seen along 25.6 kg m^{-3} during the summers of 2014 and 2015 (Figure 2.5b). By summer 2016, spice anomalies within the permanent halocline returned to near normal, however the seasonal

thermocline remained anomalously spicy. Spice anomalies during the summer 2019 MHW were minty compared to average. Minty conditions in June-July-August of 2019 were greatest within the seasonal thermocline above 25.5 kg m^{-3} (Figure 2.5b). As a consequence, the near surface $\Theta - S_A$ properties were much lighter compared to 2014–2016, both in winter and summer seasons. Minty conditions persisted into the winter of 2019/20.

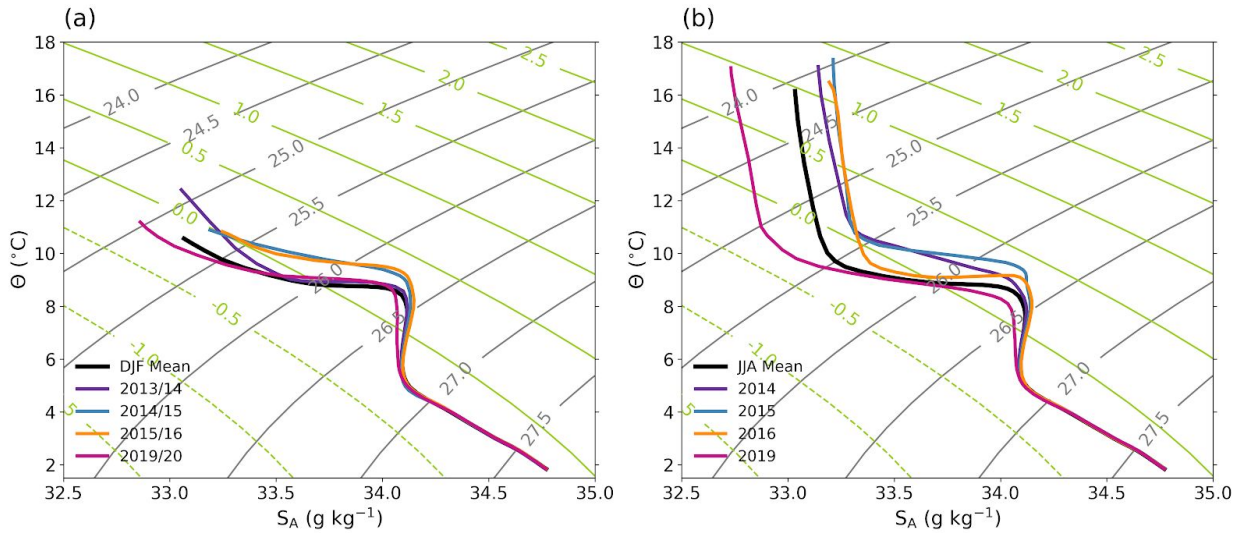

Figure 2.5 Winter (December-January-February) (a) and summer (June-July-August) (b) temperature-salinity relationships at 43.5ºN, 145.5ºW (lime green circles in Figure 2.3). The average 2004–2019 DJF and 2004–2019 JJA curves are shown by the thick black lines. Contours of constant spice (kg m^{-3}) in green are perpendicular to isopycnals in gray.

A connection between the evolution of surface and subsurface anomalies was a recurring theme during recent 2013–2016 and 2019–2020 NE Pacific MHWs and is visible in both Figures 2.4 and 2.8. To quantify the time lags associated with the penetrations of surface anomalies into the subsurface, we compute the lagged cross-correlation for Θ and S_A on isobars and isopycnals with values at 2.5 dbar and 25.7 kg m^{-3} respectively. Significant positive correlations between surface and subsurface $\Theta - S_A$ anomalies increase with positive lag and density between

25.7–27 kg m^{-3}. For example, the maximum cross-correlation on 26.3 kg m^{-3} occurs at 6 months positive lag (Figure 2.6). On the other hand, subsurface Θ anomalies (between 150–220 dbar) are most strongly correlated with the surface conditions for positive lags of 1–2 years, while subsurface S_A correlations peak at 6–12 months positive lags (Figure 2.6a and Figure 2.7a).

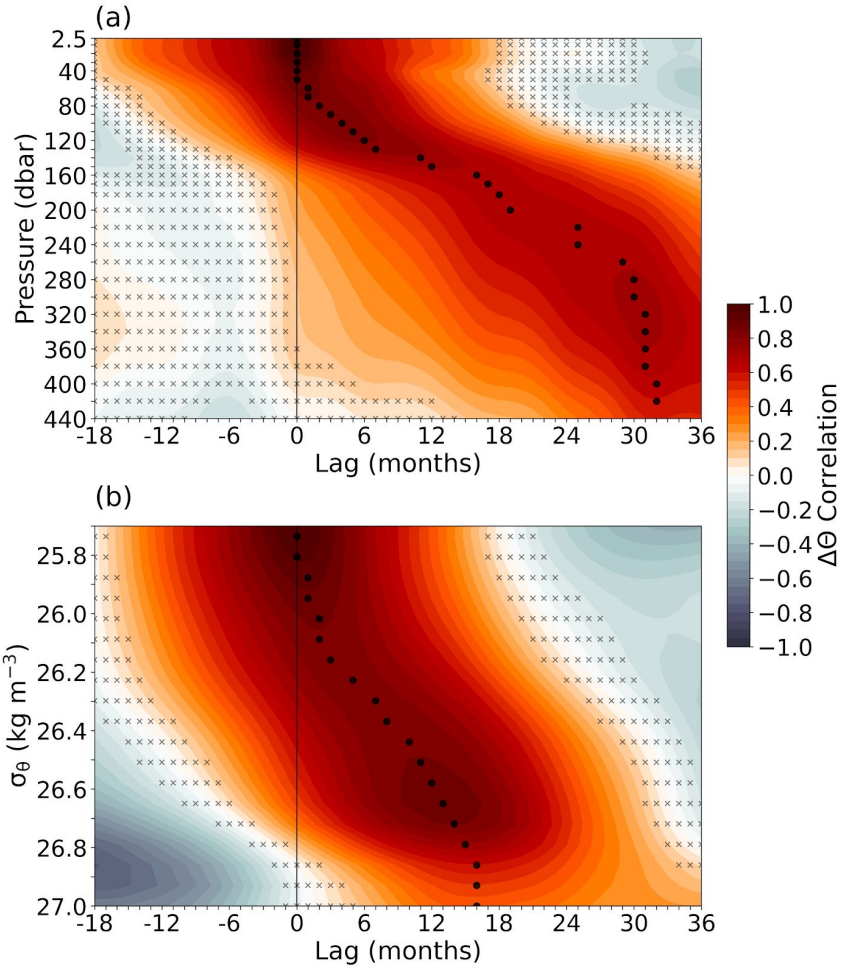

Figure 2.6 Lagged cross correlation between conservative temperature anomalies at (a) 2.5 dbar and (b) 25.7 kg m^{-3} with subsurface isobars (2.5–440 dbar) and isopycnals (25.7–27.0 kg m^{-3}) respectively. Anomalies are averaged within 35.5–51.5ºN, 135.5–154.5ºW (boxed outline in Figure 2.3). Cross correlation is computed as the Pearson's r-value ranging from -1.0 to +1.0, with larger absolute values indicating higher correlation. Cross hatching indicates insignificant correlations (p-value >= 0.05) and black circles indicate the highest positive correlation for each isobar (a) and isopycnal (b).

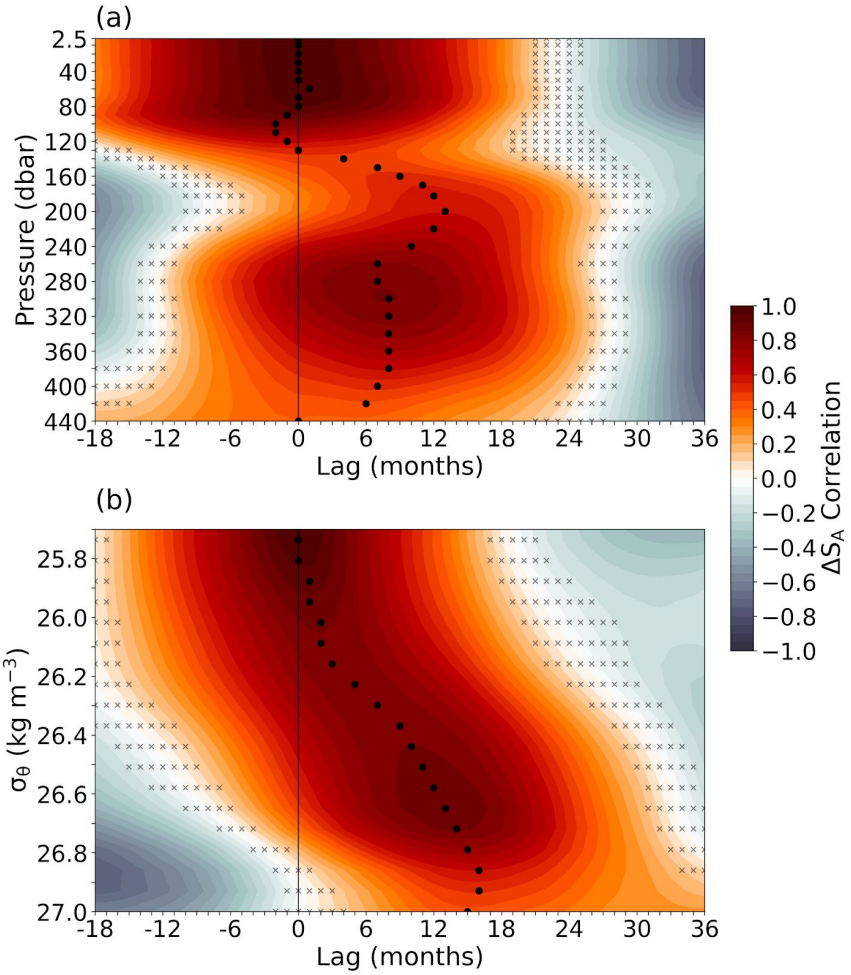

Figure 2.7 Lagged cross correlation between absolute salinity anomalies at (a) 2.5 dbar and (b) 25.7 kg m^{-3} with subsurface isobars (2.5–440 dbar) and isopycnal (25.7–27.0 kg m^{-3}) respectively. Anomalies are averaged within 35.5–51.5ºN, 135.5–154.5ºW (boxed outline in Figure 2.3). Cross correlation is computed as the Pearson's r-value ranging from -1.0 to +1.0, with larger absolute values indicating higher correlation. Cross hatching indicates insignificant correlations (p-value >= 0.05) and black circles indicate the highest positive correlation for each isobar (a) and isopycnal (b).

The downward progression of surface Θ and S_A anomalies suggest that the North Pacific Ocean is capable of maintaining long-term memory of surface MHWs. One measure of memory is the heat content anomaly, Q', evaluated here over equal thickness subsurface layers. The largest Q' values occur within the seasonally varying mixed layer (10–90 dbar) where temperature

fluctuations are the strongest (Figure 2.8). The largest positive anomalies are present during the 2013–2016 MHW. After a period of strong cooling, Q' steadily increased beginning in 2018 through the present. Prior to 2013 there were two smaller MHWs that occurred in 2004–2005 and 2008–2009 that also had small gains of heat content. Evaluating Q' over layers spanning the pycnocline (100–180 dbar) and interior (200–280 dbar) reveals the persistence of Θ anomalies below the surface temperature variability. Once $\Theta - S_A$ anomalies get into the subsurface, properties are nearly conserved even after the surface cools (Figure 2.8).

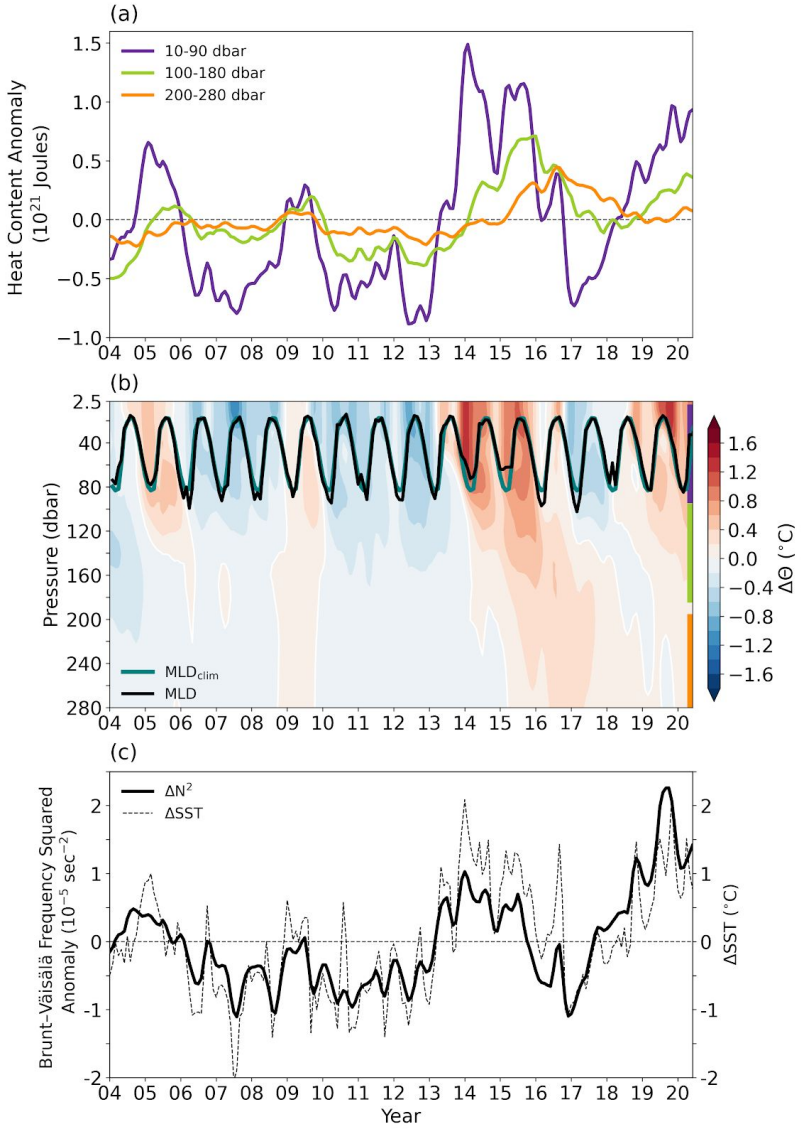

Figure 2.8 Variations in (a) upper ocean heat content anomalies, (b) temperature anomalies and mixed layer pressure, and (c) upper ocean stratification anomalies averaged in 35.5–51.5ºN, 135.5–154.5ºW (black outline in Figure 2.3). Ocean heat content anomalies are computed over three different 80-dbar pressure layers between 10–90 dbar, 100–180 dbar, and 200–280 dbar. These intervals are shown in (b) as vertical colored lines on the right hand side corresponding to (a). The mixed layer pressure and 2004-2019 climatology is computed from 19,697 Argo profiles using the Holt and Talley (2009) density algorithm. The bulk upper ocean stratification anomaly (solid lines) in (c) is computed as N^2 between 2.5 and 200 dbar and shown with the SST anomaly (dashed lines). Positive values of N^2 indicate higher water column stability and greater resistance to overturning or vertical displacement.

An increase in upper ocean heat content can affect the stability of the upper ocean. The depth of the mixed layer also shoals, which can be seen during the winters of 2013/2014 and 2014/2015 (Figure 2.8). The increase in stratification reduces entrainment of cool water from below and can exacerbate warming by reducing the thickness of the surface layer that accepts heat from the atmosphere, making the surface ocean easier to warm. The upper ocean stratification anomaly was noticeably higher (large N^2 anomaly values) in 2014–2015, with the largest values occurring in 2019 (Figure 2.8c). The very high values in 2019–2020 arise from the anomalously fresh near-surface conditions during that MHW.

2.6 Discussion

This study examines 21st Century MHWs in the NE Pacific based on gridded SST data, and also the evolution of subsurface $\Theta - S_A$ anomalies from Argo on both isobars and isopycnals during the 2013–2016 and 2019–2020 NE Pacific MHWs. Upper ocean salinity was anomalously fresh in the Gulf of Alaska during the 2019–2020 MHW, which greatly increased the buoyancy of the surface layer. Indeed, there was a net freshwater input from precipitation as can be seen in the 2018 precipitation anomaly in the Gulf of Alaska (Yu et al., 2019) that likely contributed to the decrease in surface salinity (Reagan et al., 2019). The resulting increase in stratification during 2019–2020 likely contributed to the decrease in the depth (and density) to which water property anomalies from this event were detrained, and in places subducted. The confinement of warm anomalies to the near-surface likely enhanced the MHW's intensity.

There are several dynamical pathways by which surface MHW anomalies in the NE Pacific could reach the subsurface; by means of detrainment, diabatic subduction (Jackson et al., 2018), lateral advection (Chao et al., 2017; Zaba et al., 2020), and/or adiabatic isopycnal heave. Subduction occurs in subtropical regions after temperature anomalies within the deep wintertime mixed layer detrain as a result of the mixed layer retreating in late spring. During the 2014 and 2015 spring transition of the mixed layer depth, subsurface warming occurred along both isopycnals and isobars below the mixed layer, suggesting that diabatic vertical or horizontal mixing could play a role in the penetration of MHW anomalies within the seasonal pycnocline. Indeed, Zaba et al. (2020) attribute positive subsurface heat content anomalies within the California Undercurrent to an increase in poleward heat transport from the tropics in September 2015. Alternatively, subsurface warming that occurs primarily on isobars and not on isopycnals was likely the result of isopycnal heave, defined as the downward deflection of a potential density surface. We speculate that heave is most likely responsible for the near-simultaneous appearance of anomalies below 150 dbar, for example during the 2008–2009 MHW, however the exact mechanisms of heave (i.e., from Ekman pumping due to wind stress curl) are not investigated here.

Once surface MHW anomalies are detrained out of the deep wintertime mixed layer, they may propagate downward. The lag associated with the vertical propagation of surface anomalies causes the subsurface heat content to remain anomalously high even after surface conditions return to normal. This persistence of subsurface heat and the possible seasonal reemergence of surface anomalies could in fact help supercharge the occurrence of multi-year events. As future

warming trends favor a more stratified upper ocean (Li et al., 2020), we expect that detrainment out of the mixed layer may become less effective in storing MHW anomalies in the subsurface, and therefore further amplify surface warming. This possibility is concerning owing to the impacts that accumulated heat stress and stratification have on pelagic marine ecosystems and primary production (Cavole et al., 2016; Jacox et al., 2016; Smale et al, 2019).

Mixed layer heat budgets are frequently used to diagnose the drivers of surface warming associated with MHWs; however, the influence of salinity and subsurface water mass properties are often overlooked (Holbrook et al., 2020). Using the global Argo array data, this study motivates complementary analyses on the role of salinity and subsurface $\Theta - S_A$ anomalies to better understand the ocean's role in the persistence and evolution of long-lived events. Further investigation into the drivers of salinity anomalies and their role in the development of NE Pacific MHWs would appear to be a fruitful avenue of future research. Analysis of the full 4-D heat budget using high resolution numerical models could be undertaken to investigate the local mechanisms of subsurface warming.

Chapter 3

TRACKING THE SPATIOTEMPORAL EVOLUTION OF MARINE HEATWAVES GLOBALLY

3.1 Abstract

Regional oceanic and atmospheric dynamics, and their interactions with the climate system, help to distinguish marine heatwaves (MHWs) across different ocean basins. Here, a novel tracking algorithm is presented that provides an objective chracterization of the spatiotemporal variability of MHWs. This tracking algorithm, termed *Ocetrac*, allows for the characterization of the evolution of MHWs globally from gridded datasets. Candidate MHW grid points are defined using seasonally varying temperature thresholds, and segmented into objects using edge detection. These closed-contour features undergo further elimination based on an areal size criteria. We demonstrate the sensitivities of the *Ocetrac* with respect to the edge detection and size thresholding criterion. The sensitivities to the definition for MHWs including temperature threshold, horizontal resolution of the underlying data, and the inclusion/exclusion of the long-term warming trend are also presented. The resulting three-dimensional MHWs are tracked and characterized by their intensity, duration, area, and trajectory. Using monthly satellite sea surface temperature data from 1981 through present, we demonstrate *Ocetrac's* use in characterizing four well-known MHWs in the Northeast Pacific, Gulf of Maine, off Western

Australia, and in the Mediterranean Sea. We discuss the broader uses of *Ocetrac* for tracking other oceanic extremes.

3.2 Introduction

Marine heatwaves (MHWs) occur throughout the global ocean, where their distributions are influenced by the mean state, natural variability, and anthropogenic climate change. Fundamentally, MHWs represent the extreme warm end distribution of local sea surface temperature (SST) anomalies. Previous studies have used the 90th (Oliver et al., 2018; Hobday et al., 2016) or 99th (Darmaraki et al., 2019; Frölicher et al., 2018) percentile of the SST distribution to define the extreme, where a MHW event is identified when SST exceeds this threshold for at least a certain period of time (e.g., 5-days; Hobday et al., 2016). Regions with large SST variance, for example the western boundary currents and their extensions, as well as in equatorial Pacific cold tongue, have the highest MHW intensities globally (Oliver et al., 2018). Using this definition, extremely long duration MHWs can be linked to Pacific SST variability associated with the El Niño-Southern Oscillation (ENSO) and its decadal-like counterparts (Holbrook et al., 2019; Scannell et al., 2016).

Natural variability such as ENSO can influence the surface temperature tendency during MHWs through the modulation of local conditions. For example, disturbances in atmospheric deep convection over the tropics can propagate planetary-scale waves to the midlatitudes where they excite MHWs through changes in local atmospheric conditions, or through changes in ocean thermocline depth and circulation. Large-scale modes of decadal SST variability (e.g.,

Interdecadal Pacific Oscillation) can suppress or enhance the likelihood of MHW occurrences depending on the phase and amplitude of the mode (Holbrook et al., 2019; Scannell et al., 2016). They can also influence the severity and duration of MHWs by altering the mean strength, direction, and location of ocean currents, as well as modulate air-sea heat flux. Interannual and decadal variability within the climate system has been explored using an empirical orthogonal function (EOF) decomposition of climate anomalies, with the first few EOF modes generally capturing enough of the variability to explain the dominant patterns of MHWs and their timescales (Wilks, 2006). This method has been repeatedly used to explain the spatial patterns and long-lived persistence of prominent MHWs (Amaya et al., 2020; Fewings and Brown, 2019; Oliver et al., 2018; Di Lorenzo and Mantua, 2016), however does not capture the global-scale spatiotemporal evolution of some MHWs.

The motivation to understand the evolution and drivers of MHWs is the vulnerability of marine ecosystems and fisheries to temperature extremes (Smale et al., 2019). Extreme surface warming during MHWs has resulted in widespread mass mortalities of marine invertebrates (Oliver et al., 2017; Garrabou et al., 2009), species range shifts (Mills et al., 2013), habitat destruction including coral bleaching (Hughes et al., 2017), and harmful algal blooms (McCabe et al. 2016). These impacts have the potential to alter the structure and functioning of marine ecosystems that can lead to declines in fishery landings and economic loss in tourism. As a result, MHW can directly cause socioeconomic and political tensions (Mills et al., 2013). The failure to anticipate the destructive impacts of MHWs leads to fishery management challenges, including changes to the supply chain and drop in value (Pershing et al., 2019).

Retrospective and contemporaneous studies have relied on pointwise metrics or fixed region heat budget analyses to characterize the evolution of MHW events through time. Although these approaches have been widely successful in determining the local processes responsible for MHWs, Holbrook et al. (2019) describe the merit of including large-scale dynamics in the eventual prediction of MHWs globally. Here, we consider the spatial connectivity of MHWs as they evolve in time, and describe events as connected components. We develop and propose a new method to investigate the evolution of MHWs that better describes their overall magnitude by considering total accumulated area and intensity. Four case studies are explored using this framework and we discuss the utility of characterizing the spatiotemporal evolution of MHWs in terms of prediction.

3.3 Methods

3.3.1 Data and Preprocessing

We analyze monthly global maps of SST from the 0.25º longitude by 0.25º latitude gridded Optimum Interpolation SST version 2 (OISSTv2) dataset that extends from September 1981 through April 2020. The OISSTv2 combines satellite Advanced Very High Resolution Radiometer (AVHRR-only) with observations from ship, buoy, and *in situ* measurements (including Argo floats and drifters), while accounting for platform differences and using interpolations to fill gaps in the satellite data (Reynolds et al., 2002; 2007). We create a mask over the Arctic (>65ºN) and Antarctic (>70ºS) Oceans to remove data in these regions and to avoid influence from seasonal sea ice and where the OISSTv2 data are less reliable (**Figure 3.3**).

To investigate the sensitivity of spatial resolution on MHW statistics, we resample the original grid using bilinear interpolation to 0.5º, 1º, and 2º degrees latitude-by-longitude resolution and repeat our analysis (**Figure 3.1**). As illustrated for the Gulf Stream, resampling coarsens the horizontal resolution and level of detail without changing the maximum and minimum amplitudes (**Figure 3.1**). The original ¼º grid reveals greater structure in Gulf Stream SST meanders and filaments that are difficult to discern at lower sampled resolutions.

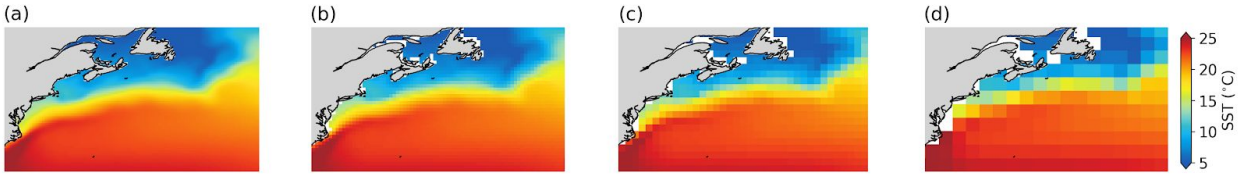

Figure 3.1 Resampled OISSTv2 from a horizontal resolution of (a) 0.25º to (b) 0.50º, (c) 1.0º, and (d) 2.0º. Maps show the mean SST from September 1981 through April 2020 in the Northwest Atlantic.

The decomposition of monthly SSTs at each grid point , represented as the fit (SST_{fit}) are a linear combination of the mean (SST_m), trend (SST_t), annual and semiannual harmonics (SST_s), where

$$SST_{fit} = SST_m + SST_t + SST_s \quad \textbf{(Figure 3.2)}.$$

The coefficients of SST_{fit} are found using least squares regression fit to monthly SST. We define SST anomalies $(SSTa)$ as the difference between monthly SST and the fitted SST time series, such that

$$SSTa = SST - SST_{fit} \ .$$

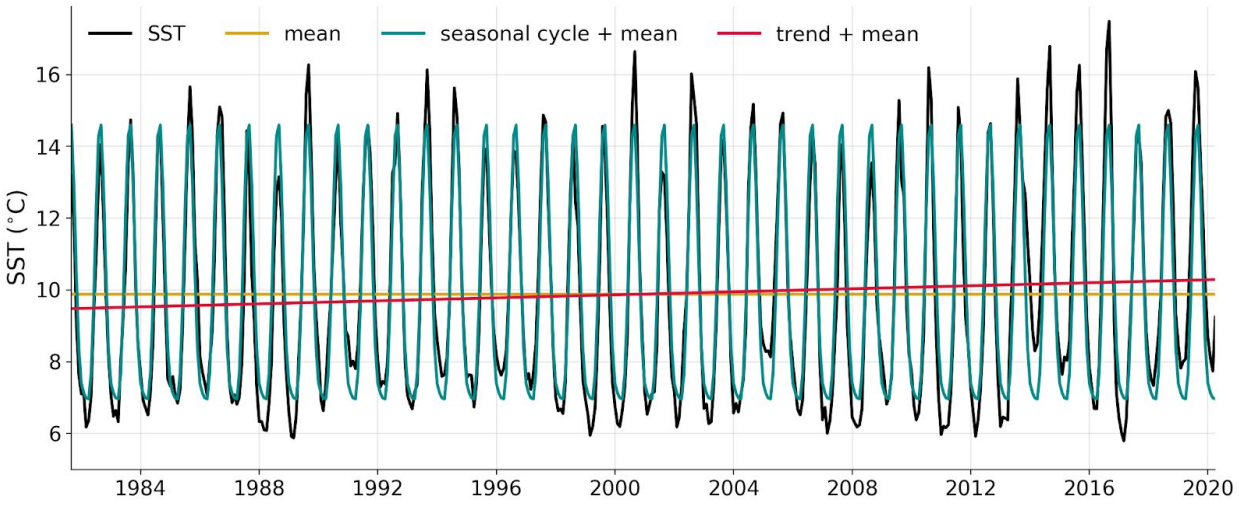

Figure 3.2 Decomposed monthly time series from the 0.25º resolution OISSTv2 at 47ºN, 149ºE into (a) mean, trend, annual and semiannual harmonics (seasonal cycle). Location is noted by white mark in **Figure 3.4b**.

We begin the analysis on detrended SST. We also repeat our analysis and sensitivity assessment with the trend included. The trend is largest at mid-latitudes in the subtropical gyres, especially in the Northwest Atlantic, western North Pacific, and western South Pacific (**Figure 3.3**). Regions with a large positive trend may produce more intense, longer lasting, and widespread MHWs toward the latter end of the record due to long-term warming.

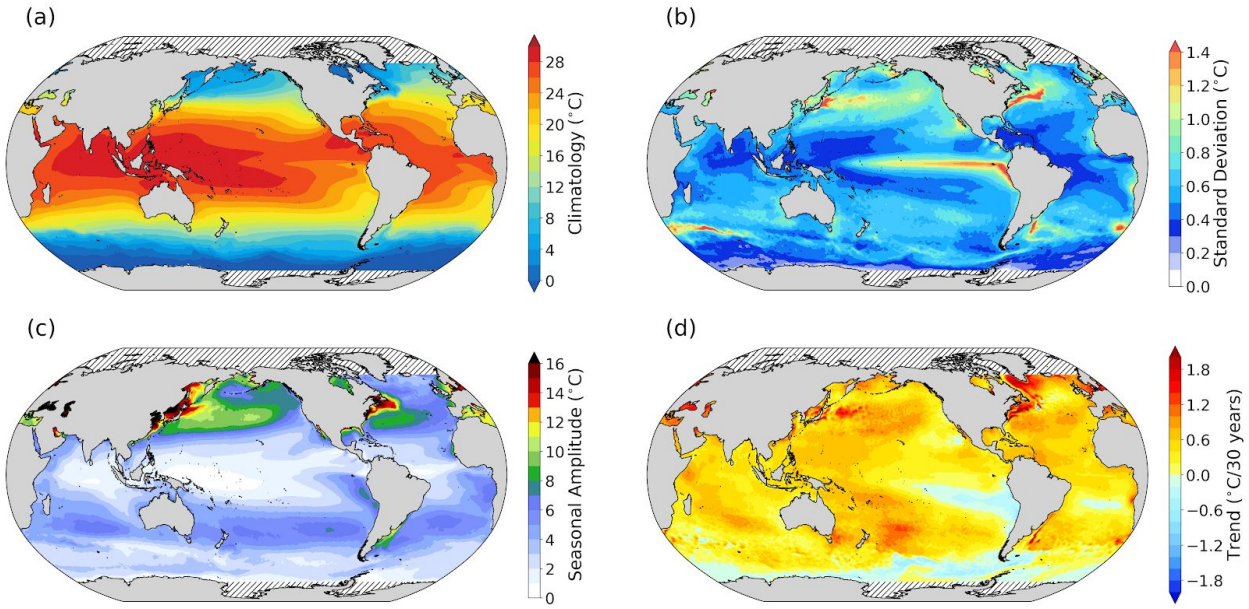

Figure 3.3 Global monthly mean distribution of (a) SST, (b) standard deviation of detrended SST anomalies, (c) amplitude of the seasonal cycle of SST, and (d) the 30 year trend in SST from 1989 through 2019. Maps in (a-c) have means computed with respect to September 1981 through April 2020. Hatching over the polar oceans represent regions that are excluded from this analysis.

3.3.2 Anomaly Detection

From the detrended monthly SST maps, we search for SST extremes that exceed an intensity threshold — defined as *anomaly detection*. We compute a seasonally varying temperature threshold to find candidate MHW points when SST exceeds the local 90th, 95th, or 99th percentile to explore the sensitivity of the results to the threshold percentile (**Figure 3.4**). During months where the target threshold criteria is exceeded, we take the SSTa by removing the local mean, trend, and seasonal harmonics. These detrended SSTa maps are then standardized by dividing by the respective local monthly standard deviation of SSTa over the entire period. Dividing by the standard deviation places equal variance on SST anomalies globally and accounts for non-seasonal spatial variability (**Figure 3.3**). High standard deviations occur in the eastern

equatorial Pacific, western boundary currents, the region connecting the Indian Ocean to the South Atlantic, and in frontal zones with large SST gradients. Comparatively, the subtropics, southern midlatitudes, equatorial Atlantic Ocean, equatorial Indian Ocean, and western tropical Pacific have low standard deviations (**Figure 3.3**).

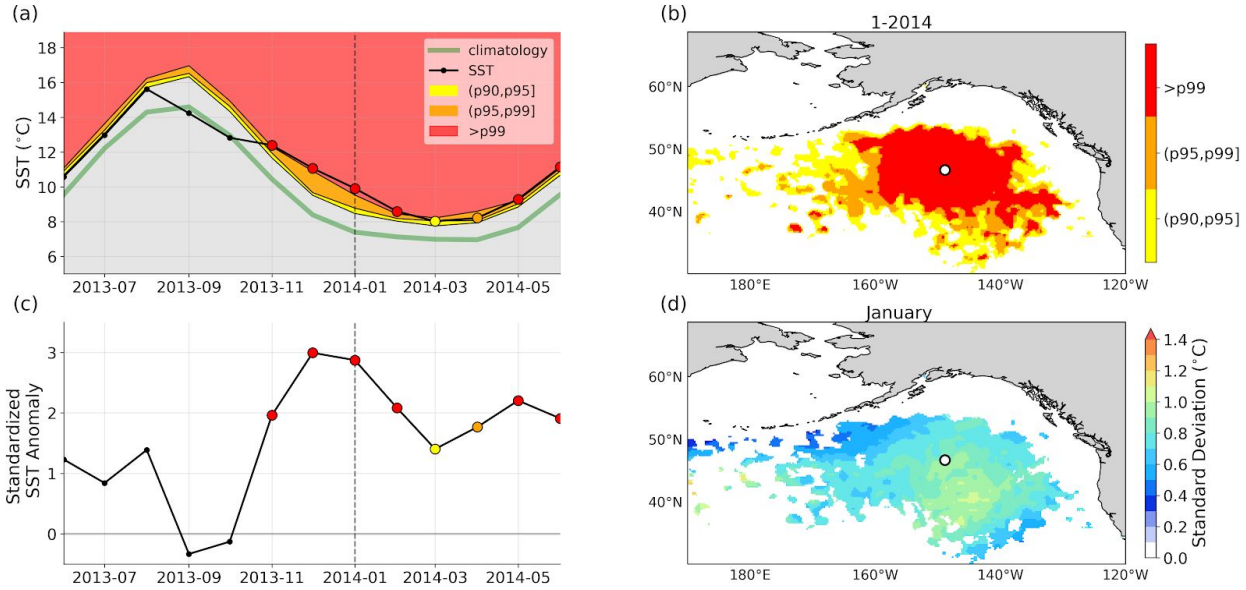

Figure 3.4 Monthly time series of SST in the Northeast Pacific (47ºN, 149ºE; white mark in (b and d)) from June 2013 through June 2014. The 90th, 95th, and 99th percentile thresholds, and the 1981-2020 climatology are shown in (a). Months that exceed the thresholds are emphasized and colored according to the percentile category of which they exceed. The map in (b) shows the spatial distribution of SST in January 2014 that exceeds the local 90th, 95th and 99th percentiles. Standardized anomalies (47ºN, 149ºE) are dimensionless in (c), where SSTs have the seasonal cycle, mean, and trend removed and are divided by the local monthly mean standard deviation of detrended SSTa from September 1981 through April 2020. MHW anomalies in (c) are emphasized as in (a). The map in (d) shows the standard deviation of January detrended SSTa.

The temperature threshold for anomaly detection is calculated as a percentile from the monthly distribution of SST over the entire period. Choosing the 99th percentile reduces the number of grid points identified as MHW candidates (**Figure 3.4b**), and selects only the highest intensity anomalies (**Figure 3.4c**). A higher percentile increases the intensity threshold that SST must

exceed to be considered a MHW. If normally distributed, a higher intensity threshold has a lower probability, and thus occurs less frequently. If the 90th percentile is used, a broader area of SSTa is identified as potentially a MHW and encompasses all anomalies detected using the 95th or 99th percentile as well (Figure 3.4c). Given the further limitations *Ocetrac* places on MHW detection, the 90th percentile appears to be a good choice for the initial selection criteria, however we discuss the implications of also choosing the 95th or 99th percentiles in Section 3.4.

The anomaly detection algorithm described in Section 3.3.2 is evaluated at every space and time point for SST at 0.25º, 0.5º, 1.0º, and 2.0º horizontal resolutions and for temperature thresholds of the 90th, 95th and 99th percentiles. The algorithm is repeated for SST with the trend removed, as well as with the trend retained. These variations produce 24 different datasets for extreme SSTa that are then used in the object tracking component of *Ocetrac*.

3.3.3 Multiple Object Tracking

The SSTa maps produced by the anomaly detection algorithm are transformed into a binary image where ones correspond to a candidate MHW grid point and zeros correspond to background grid points. Each month of the mask is treated as a separate image, with features represented by the presence of ones. Our goal is to identify groupings of ones that meet the spatial characteristics of MHWs in terms of structure and size. Image processing terminology and symbols are further defined in **Table 3.1** and illustrated in **Figure 3.5.**

Table 3.1 Glossary of common terms and their symbols used in image processing and set theory.

Term	Definition	Symbol
Binary Image	A 2D map (x,y) with ones corresponding to candidate MHW grid points (as described in Section 3.3.2) and zeros corresponding to either non-MHW grid points or land points.	I
Features	Within binary images, features refer to grid points with values of one.	
Objects	Within binary images, clusters are features that are connected in either space or time (x,y,t).	
Structuring Element	A 2D binary image with unique shape and size applied in the morphological operations such as erosion and dilation.	S
Connectivity Element	Centrosymmetric 3D binary array with shape 3x3x3 used to track MHWs in space and time (x,y,t).	
Erosion	Contracts the boundary of a binary image and removes small-scale details.	$I \ominus S$
Dilation	Expands the boundary of a binary image by adding a layer of pixels.	$I \oplus S$
Opening	Erosion followed by dilation. Smoothes contours by breaking narrow isthmuses and eliminates small islands and sharp peaks.	$I \circ S$
Closing	Dilation followed by erosion. Smoothes contours by fusing narrow breaks and long thin gulfs, and eliminates small holes.	$I \bullet S$
Centroid	The geographic center of each object. A MHW can have multiple centroids if connected objects merge or split.	
Sub ID	An additional ID given to MHWs with more than one centroid per month. For example, the 50th MHW with three centroids would be labeled as 50.1, 50.2 and 50.3 respectively.	
	"For all"	$\forall$
	"Element of"	$\in$
	"Subset of"	$\subseteq$
	"Union"	$\cup$
	"Set" or a collection of elements	$\{\}$
	"Such that"	$\mid$

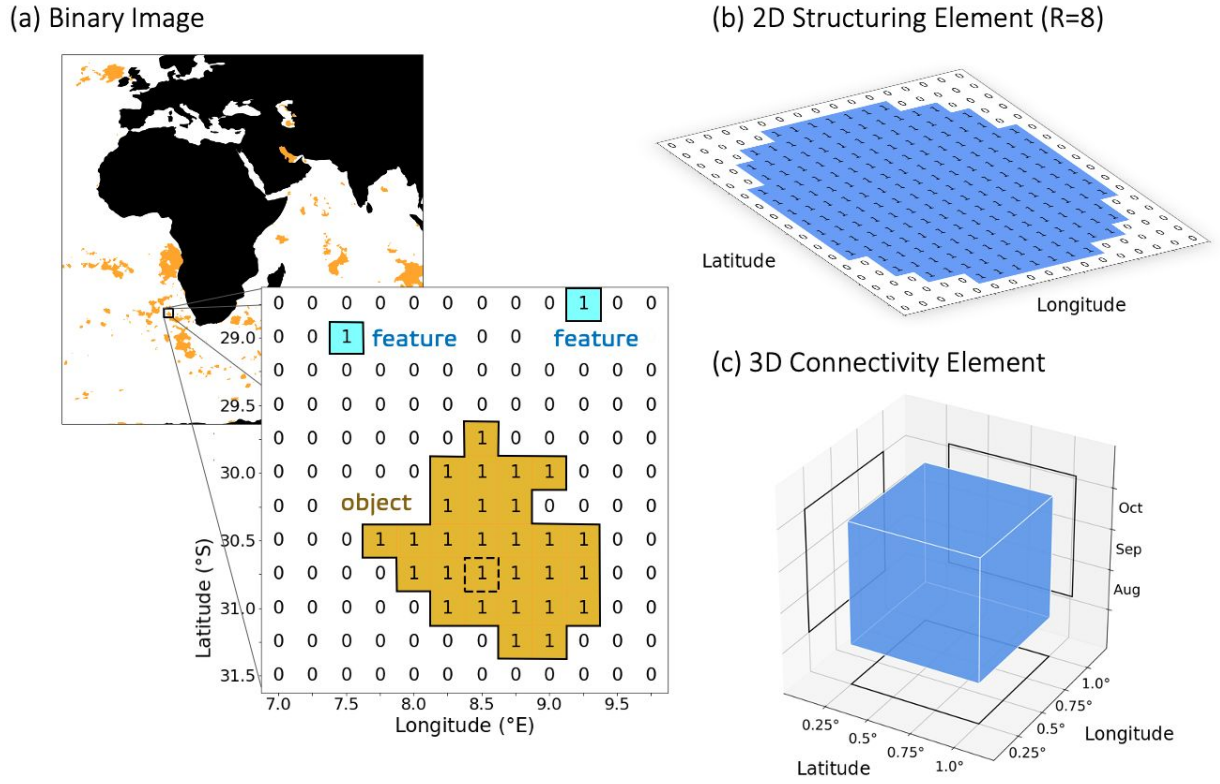

Figure 3.5 Illustrations of terminology used in *Ocetrac*. The (a) binary image contains features and connected features called objects. The centroid of an object is defined by its geometric center (dashed grid box). A (b) 2D structuring element is used in morphological operations, and a (c) 3D connectivity element is used in multiple object tracking.

We first use mathematical morphology operations from the SciPy multidimensional image processing Python package to remove small, isolated features, as well as fill small holes within feature clusters. A structuring element is defined according to its shape and size. Here we define the shape of the structuring element (S) by a quadratic surface with a size radius R, where

$$S = (x^2 + y^2) < R^2 \ , \ \forall R \in \{3, 4, 5, 6, 7, 8, 9, 10\} \ .$$

Here, x and y are vectors of grid spaces in longitude and latitude dimensions respectively, and have length $2R$. The units of R are in degrees per unit resolution of the grid (e.g., an R of 8 on a ¼° grid is equal to 2° latitude or longitude). We iterate through different values of R to explore

how the size of the structuring element affects MHW characteristics. By design, S is a binary image itself and represents a subset of the integer grid as it scans over the image at its origin (**Figure 3.6**).

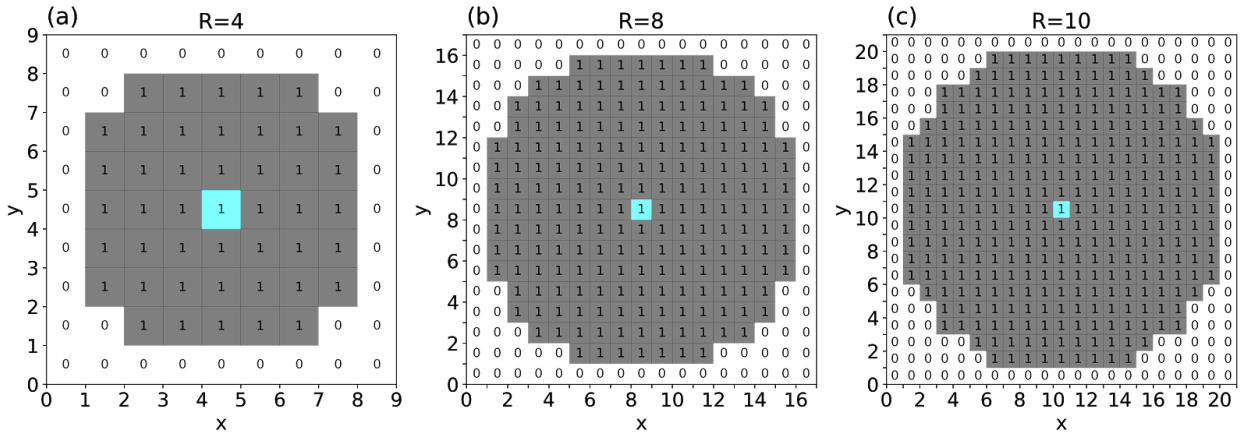

Figure 3.6 Structuring elements (S) defined by the binary subset of horizontal grid cells of x and y. The center of a structuring element (denoted by the cyan grid cell) is centered on each unique positional element of the image (I) for each erosion and dilation morphological operation. Structuring elements are defined by shape and size. As an example, elements shown here have a parabolic shape with radii (R) of (a) 4, (b) 8, and (c) 10 grid spaces.

The structuring element is used to scan over the entire image and is used to manipulate features based on the dilation and erosion of the image (Gonzalez and Woods, 2002). Erosion eliminates isolated and small features so that only substantial objects remain. If E represent the global integer grid domain and I the binary image at each monthly time step, then the erosion of I by a structuring element S (denoted $I \ominus S$) is defined by,

$$I \ominus S = \{i \in E \mid S_i \subseteq I\}\text{, where}$$

$$S_i = \{s + i \mid s \in S\}, \forall i \in E.$$

S_i is the geometric translation of the structuring element by the vector i so that its origin is along I. Vectors i and s represent each unique positional element of I and S respectively. For

each pixel in I, if the superimposition of S centered on all I pixels is not completely contained by ones, then that pixel in I is turned to zero, else that pixel is retained as a one. It is necessary to note that in order to prevent feature shrinkage around the border of I, we pad zeros along the perimeter equivalent to the diameter of S. After erosion, we remove the padded integers to retain the original shape of I.

Dilation is the opposite of erosion and is used to fill small holes within features. It acts to gradually enlarge the boundaries of the feature region. The dilation of I by S (denoted $I \oplus S$) is defined by the union of the geometric translation of I (I_s), where

$$I \oplus S = \bigcup_{s \in S} I_s \text{, and}$$

$$I_s = \{s + i \mid i \in I\} \text{, } \forall s \in E \text{.}$$

S is superimposed at the origin on all I pixels with values of one. All values within the superposition are turned to one, whereas other pixels remain zero.

Erosion and dilation are done for each unique i and s, and their operations can be combined in succession (**Figure 3.7**, Gonzalez and Woods, 2002). For example, morphological opening (denoted as $I \circ S$), is erosion followed by dilation using the same structuring element, defined as,

$$I \circ S = (I \ominus S) \oplus S \text{.}$$

Opening is useful for eliminating small features while preserving the shape and size of larger features in the image. Alternatively, morphological closing (denoted as $I \bullet S$), is the process of eroding a dilated image, again using identical structuring elements. Closing is defined as,

$$I \bullet S = (I \oplus S) \ominus S .$$

Closing fills small holes within features while also preserving the shape and size of other features in the image. Both opening and closing are beneficial for removing small features, and smoothing the borders of larger features. Here, we implement a series of morphological closing then opening, as we found this to optimally "clean" feature images in **Section 3.3.2** (**Figure 3.6**).

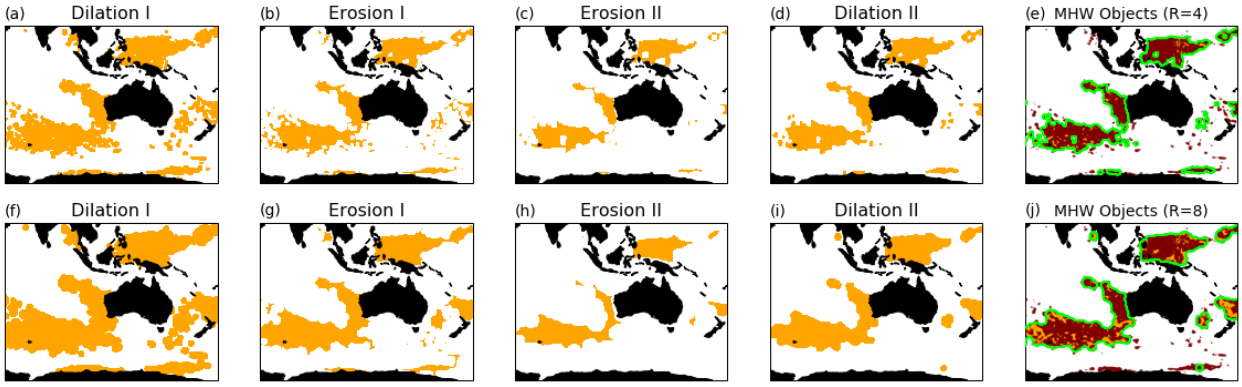

Figure 3.7 Sequence of morphological operations for closing (Dilation I followed by Erosion I) then opening (Erosion II followed by Dilation II) using a structuring element with a radius of 4 grid cells (a-e) and a radius of 8 grid cells (f-j). Orange shading represents the feature area that the morphological operations are performed on. Red stippling in (e, j) shows the grid cells identified as potential MHWs before the morphological operations. Green contours outline the final shape of the identified MHW objects. Data shown here is from February 2011 using the ¼° resolution OISSTv2 with the trend removed and 90th percentile as the threshold for anomaly detection.

Next, we label connected 2D objects from binary images using Scikit-Image's measure module in Python. We define objects when two neighboring features with the same value are connected either adjacent or diagonal from each other (**Figure 3.5**). The resulting 2D objects are assigned a

unique label, and this process is repeated for each time step. For each unique object, we use the latitude and longitude coordinates from the Scikit-Image's regionprops module to calculate total object area. Using the distribution of all object areas from 1981 through 2020, we calculate a percentile based minimum size threshold criteria ranging from the 60^{th} to 95^{th} percentile, and we eliminate objects that fall below this threshold. We discuss the sensitivity of the chosen size threshold on MHW characteristics in **Section 3.4**.

Once objects smaller than the size threshold are eliminated, we convert the images back to binary where ones correspond to objects and zeros are ignored as the background. We redefine objects using a 3D centrosymmetric connectivity element, such that two features with similar values that are either adjacent or diagonal to each other and that also overlap in time are connected. Objects are again uniquely labeled with an ID and tracked sequentially through time. No temporal gap is allowed and no minimum percent overlap is enforced here. There are two possible evolutions: (1) multiple objects with the same ID will merge at a future time, and (2) a single object can split into multiple objects where they will retain their original ID. As a result, any objects that have connectivity will share an ID.

In summary, we describe a new tracking algorithm called *Ocetrac* to detect and follow the evolution of MHWs (**Figure 3.8**). There are two design choices inherent to *Ocetrac*, including morphological radius (R) and minimum size threshold. We discuss the sensitivities of these choices in the following section, along with useful metrics for characterizing the global spatiotemporal evolution of MHWs.

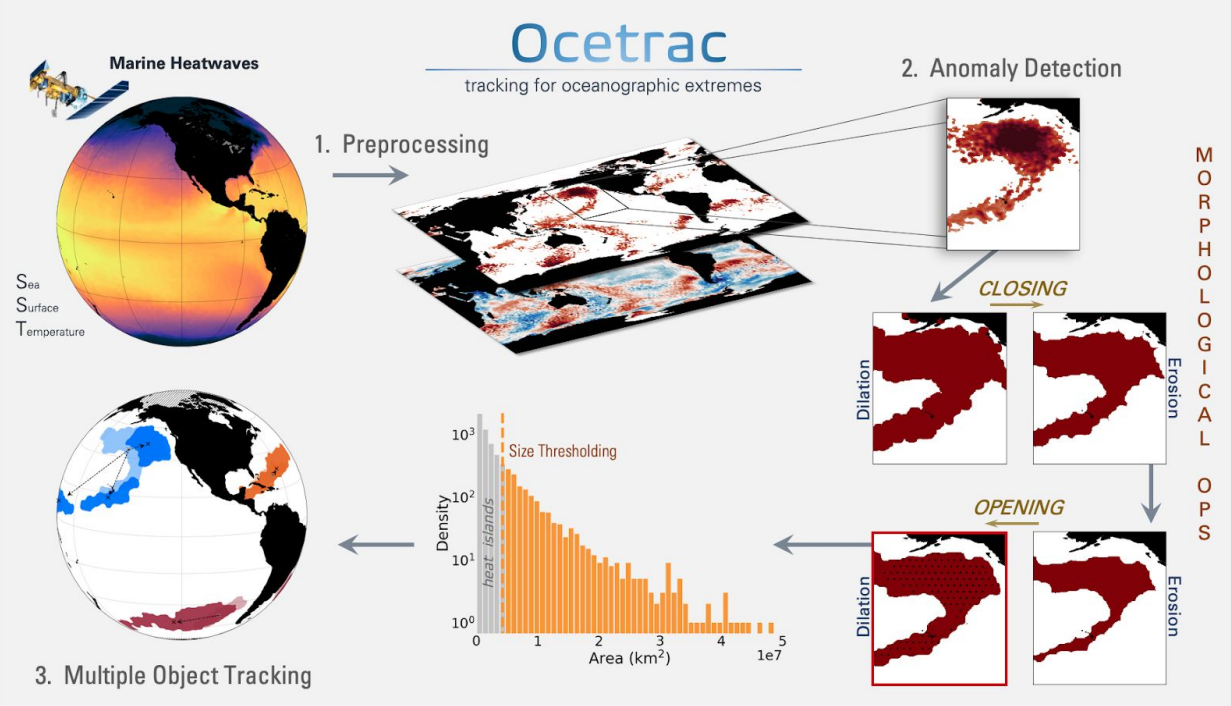

Figure 3.8 Multi-step process for detecting and tracking marine heatwaves implemented by the *Ocetrac* algorithm. Global gridded satellite measurements of sea surface temperature are used to extract seasonally varying detrended anomalies that exceed the local 90th percentile. These anomalies are then passed through two sequences of morphological operations (closing and opening) to detect object edges. Objects that exceed the 75th percentile of the distribution of object areas are then labeled and tracked as they evolve through time and space.

3.4 Sensitivity Analysis

The representation of MHWs is dependent on the criteria used to define their intensity, size, duration, and shape. In addition, this representation can be influenced by the horizontal resolution of the SST data, and whether or not the trend is removed. We investigate the sensitivity of the morphological smoothing radius and minimum size threshold criterion implemented in *Ocetrac*. Specifically, we quantify the effect of these criteria on the number of

MHWs detected, average duration, minimum MHW area, and the percent of MHWs with multiple centroids.

As the smoothing radius and minimum size threshold increase, fewer MHWs are detected (**Figure 3.9a**). A large radius increases the connectedness of features in the binary images, thus resulting in fewer, but also larger, MHWs. These well connected MHWs are also likely to persist for durations greater than 3 months (**Figure 3.9e**). The percentage of MHWs with multiple centroids decreases with increasing radius (**Figure 3.9d**). Fewer MHWs have multiple centroids with large radii as a result of increased connectivity among features.

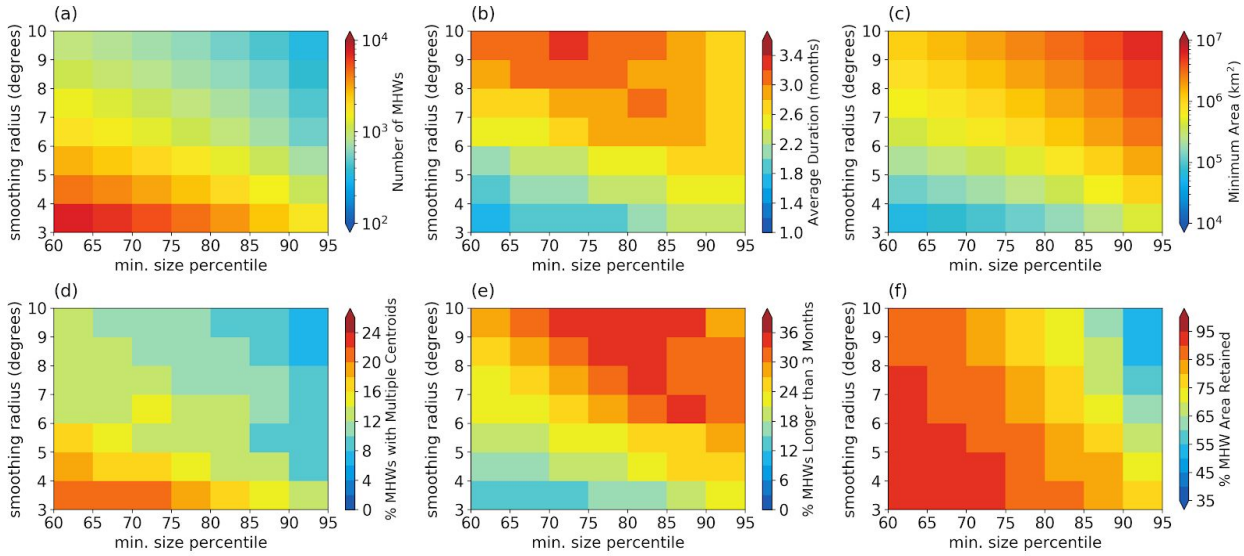

Figure 3.9 Sensitivity of MHW characteristics globally with varying smoothing radius and minimum size percentile parameters, including the (a) number the MHWs detected from September 1981 through April 2020, (b) average monthly duration of MHWs, (c) minimum MHW area, (d) percent of MHWs with multiple centroids, (e) percent of MHWs longer than 3 months, and (f) percent of MHW area retained. Data shown here are for ¼° resolution OISST with MHWs defined when detrended SST exceeds the local monthly 90th percentile from September 1981 through April 2020.

The sensitivity of duration is non-monotonic, however, and generally increases with smoothing radius and minimum size percentile. This nonlinear behavior is the result of the decline in the number of MHWs detected as the minimum size percentile increases. A smaller population size also decreases the average duration (**Figure 3.9 b and e**). Duration appears most sensitive to smoothing radius, where large radii increases connectivity between neighboring features allowing MHWs to persist for longer periods of time.

Large minimum size thresholds reduce the percentage of the total MHW area retained. Small thresholds retain a greater percent of the original MHW area, and therefore also produce more MHWs of smaller size (**Figure 3.9 a, c and f**). As the size threshold increases, the percent of total MHW area retained quickly declines to less than 50%. The number of MHWs detected also declines to less than 100 and the smallest sized events intuitively increase in size. If the size threshold is held constant, the percent of total MHW area retained also decreases and the minimum MHW area increases with increasing smoothing radius. The larger smoothing radii help join neighboring features and fills holes within feature clusters. Thus, large smoothing radii help to grow MHWs, while also decreasing the total number of MHWs detected.

For a demonstration of the sensitivity of an example MHW to the smoothing radius and size percentile threshold, consider the 2011 MHW off Western Australia (**Fig. 3.10**). In this case, the shape and size of the detected objects are noticeably different between radii of 4 and 8, and with the results are independent of area threshold. A smoothing radius of 4 produces objects with sharp and jagged edges and interior holes (**Figure 3.10 a,d,g**). The object shape difference

between a radius of 8 and 10 is nearly negligible, with the exception of small features disappearing (e.g., **Figure 3.10b vs. Figure 3.10c**). As the minimum size threshold increases, there are sudden disappearances of objects whose areas fall below the threshold. The sensitivities of the radius and size parameters gives insight into the biases introduced in tracking MHWs. Here, we use a radius of 8 as it provides enough detail of the original objects while creating smooth edges. We also choose the 75th percentile for the minimum size threshold as it isolates the well-known MHWs that have occurred in the 21st Century, including the event of Western Australia in 2011 (**Figure 3.10e**).

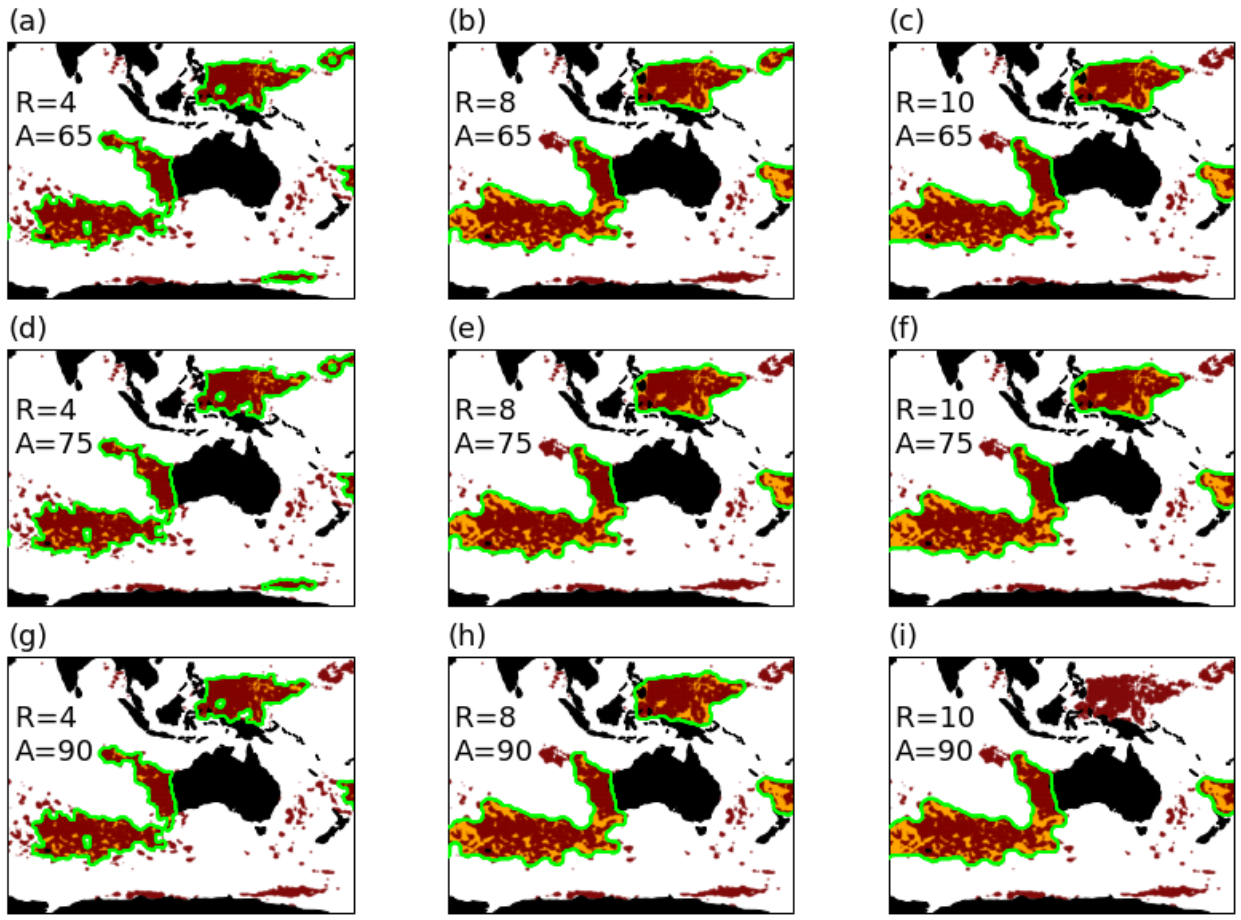

Figure 3.10 Sensitivity of objects detected from the morphological operations in February 2011 from the ¼° resolution OISSTv2 with the trend removed and 90th percentile as the threshold for anomaly detection. Each panel represents a unique combination of radius and minimum size

threshold from 4−10 grid spaces and 65^{th}−90^{th} percentiles respectively. Detected objects are outlined in green, red stippling indicates grid points where SST exceeds the 90th percentile, and orange shading represents filled in MHW regions to create closed contour objects outlined in green.

The sensitivity analysis reveals the effect that the choice of parameter influences basic characteristics of MHWs such as number, duration, and size. To optimize our choice, we aim for approximately 10 MHWs per year (~400 from 1982-2020), a minimum area roughly the size of Alaska (~$2x10^6$ km^2), and lasting on average 3 months (Holbrook et al., 2019). Below, we show results using a smoothing radius of 8 and the 75^{th} minimum size percentile for MHWs that exceed the local monthly 90^{th} temperature percentile using the ¼º OISSTv2.

3.5 Metrics

Ocetrac allows for the characterization of discrete MHWs in both time and space. For the MHWs identified, we define a set of metrics that are computed over the lifetime of each event and at monthly increments (**Table 3.2**). The first set of metrics describe the SSTa intensity within the MHW. Since the object detection includes regions not initially identified as MHW candidate grid points (e.g., orange regions in **Figure 3.10**), we use the entire SSTa field within the object contour (green outlines in **Figure 3.10**) to calculate the mean, maximum, and cumulative intensity. These anomalies are calculated with respect to the local monthly climatology from 1982-2020 and have been standardized by the local monthly standard deviation of the SSTa (see *Anomaly Detection*). The MHW anomalies are summed over the area and duration of the event to calculate the cumulative intensity. Degree heating weeks (ºC-weeks) are commonly used to study the impacts of coral bleaching in tropical reef ecosystems (Kayanne,

2017; Eakin et al., 2010). Here, the cumulative intensity (ºC-km^2-months) provides a measure of accumulated heating over the lifetime of the MHW and can be informative when assessing the time, space, and temperature dependence of ecological impacts related to MHWs.

Table 3.2 Description of metrics used to characterize individual MHW events.

Metric	Unit	Definition
Intensity		
Mean	ºC	Average SSTa
Maximum	ºC	Maximum SSTa
Cumulative	ºC km^2 months	Sum of SSTa over the total area for the duration of the event
Duration	months	Persistence of MHWs in time
Area		
Mean	km^2	Average MHW grid area over the duration of the event
Maximum	km^2	Largest MHW grid area over the duration of the event
Total	km^2	Sum of unique grid area over the duration of the event
Centroid	(ºlat, ºlon)	Geometric center of each object for each MHW defined at each time step

MHWs have a discrete start and end date, which defines the duration of an event. Here, the start date is determined once the SST exceeds the local 90th percentile with a continuous area that exceeds the minimum size threshold. The termination of a MHW occurs when either the SST falls below the temperature threshold or when the area diminishes to less than minimum size criteria. The time frequency considered here is monthly, meaning that events with durations shorter than a month are not considered.

Area is an important qualifier for a MHW and is defined as the sum of grid boxes contained within each object and takes into consideration grid resolution and latitude. Since MHW with multiple objects can contain several centroids, we also compute the area for each object within

the MHW. Given that MHWs evolve in space over their lifetime, it is also informative to find the total MHW area as the sum of unique grid points contained within the MHW over its duration. The mean and maximum areas are also computed for each MHW. Since area is dependent on the horizontal grid resolution, we investigate the sensitivity to downsampled grids for case studies in **Section 3.6**.

The distributions of MHW duration and area are heavy-tailed, meaning that short lived or small area events occur more frequently than long-lasting or large area events (**Figure 3.11**). By construction, both duration and area have minimum thresholds of one month and 1.85×10^6 km^2 respectively. The largest MHW occurred during the 2013–2017 NE Pacific "Blob" impacting a total area of 1.96×10^9 km^2 and persisting for 53 months. The 2009–2011 MHW off Western Australia had the second largest total area and duration covering 1.04×10^9 km^2 for 51 months (**Table 3.3**). The 2012 Gulf of Maine and 2003 Mediterranean Sea MHWs were closer to the global average duration (3.15 months) and average total area (2.38×10^7 km^2) of all 727 MHWs detected from September 1982 through April 2020.

The maximum MHW intensity has a positively skewed distribution with a mean of 3.41ºC, maximum of 10.06ºC, and minimum of 1.55ºC (**Figure 3.11**). The 2013–2017 Northeast Pacific "Blob" had a larger maximum intensity (8.93ºC) than the 2009–2011 Western Australia (4.57ºC), 2012 Gulf of Maine (3.68ºC), and 2003 Mediterranean Sea (4.14ºC) MHWs, although the maximum intensities of all four MHWs were above average (**Figure 3.11a, Table 3.3**).

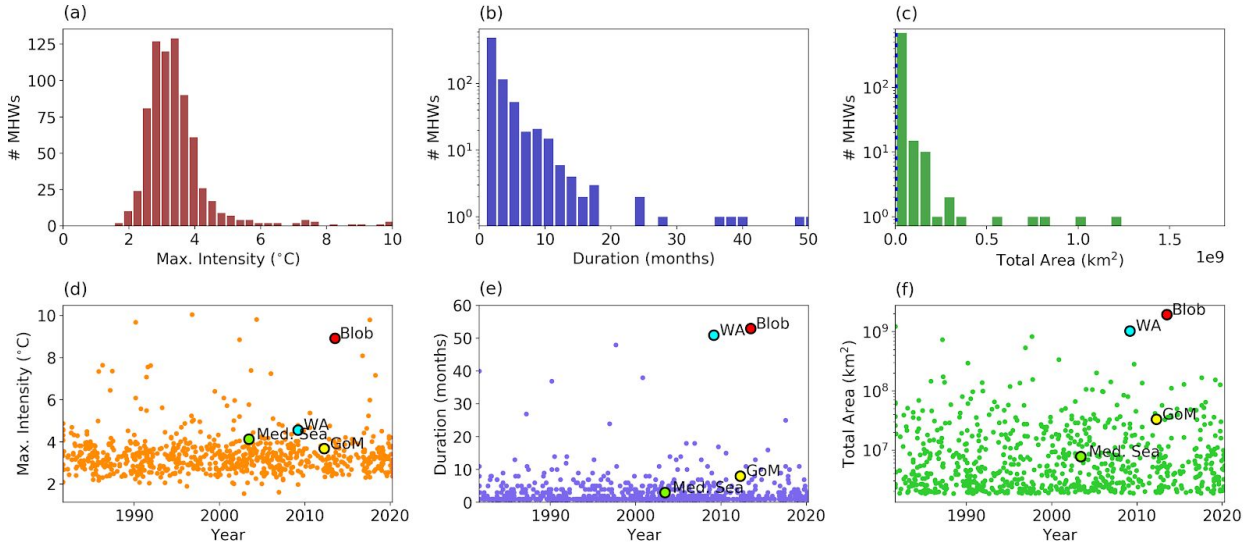

Figure 3.11 Distribution of (a) maximum intensity (mean=3.41ºC, min.=1.55ºC, max.=10.06ºC), (b) duration (mean=3.15 months, minimum=1 month, maximum=53 months), and (c) total area (mean=2.38x10^7 km^2, minimum=1.85x10^6 km^2, maximum=1.96x10^9 km^2) for 727 MHWs detected between September 1981 through April 2020. MHWs are identified from the ¼º resolution OISSTv2 and defined when the detrended SST exceeds the local monthly averaged 90th percentile. MHWs have been smoothed with a 8 grid spacing morphological radius and only events that exceed the 75th percentile (1.85x10^6 km^2) of the initial areal distribution are considered.

There is considerable year-to-year variability in MHW metrics that is likely caused by natural climate variability (**Figure 3.12**). The El Niño-Southern Oscillation is the largest interannual driver of SST variability that can influence the likelihood of MHW and their characteristics (Scannell et al., 2016). We investigate the relationship between the yearly global means in maximum intensity, duration, and area with the Niño 3.4 index between 1982–2019. We derived the Niño 3.4 index as the average detrended yearly SSTa averaged within 5ºN–5ºS and 170ºW–120ºW from 1982 through 2020. Although ENSO and its teleconnections are important drivers of MHWs (Holbrook et al., 2019), we did not find a significant correlation between the yearly Niño3.4 index and interannual variability associated with MHW intensity, duration, or

area. Therefore, Niño3.4 might not be the most informative index of year to year MHW variability.

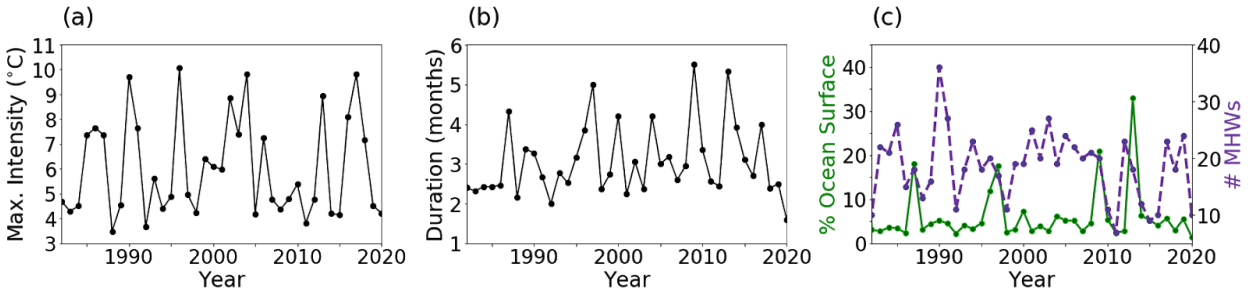

Figure 3.12 Globally averaged yearly (a) maximum MHW intensity, (b) duration, and (c) percent of total ocean area covered by a MHW and number of MHW events from 1982 through 2020. MHWs are identified from the ¼º resolution OISSTv2 and defined when the detrended SST exceeds the local monthly averaged 90th percentile. MHWs have been smoothed with a 8 grid spacing morphological radius and only events that exceed the 75th percentile (1.85x10^{6} km^{2}) of the initial areal distribution are considered.

MHW metrics not only vary in time, but also geographically. We compute the maximum intensity, number of centroids, and accumulated duration within 5º-latitude by 5º-longitude bins between September 1982 through April 2020 (**Figure 3.13**). There were a total of 3,048 centroids corresponding to 727 MHW events. Maximum MHW intensities were greatest (>4ºC) at middle and high latitudes, and in the eastern tropical Pacific and central Indian Ocean (**Figure 3.13a**). Despite an even distribution of MHW centroids, the Pacific and Indian Oceans have been exposed to more total MHW months compared to the Atlantic Ocean (**Figure 3.13b,c**). We suspect this is likely due to the large influence of Pacific SST variability originating from the tropics.

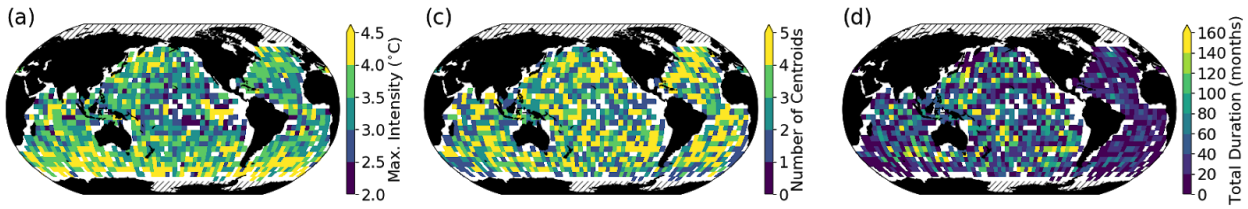

Figure 3.13 Binned (a) maximum intensity, (b) number of centroids, and (c) total duration for 3,048 centroids corresponding to 727 unique MHWs. Bin size is 5º latitude by longitude. MHWs are identified from the ¼º resolution OISSTv2 and defined when the detrended SST exceeds the local monthly averaged 90th percentile. MHWs have been smoothed with a 8 grid spacing morphological radius and only events that exceed the 75th percentile (1.85x10^{6} km^{2}) of the initial areal distribution are considered.

Metrics from **Table 3.2** are useful to describe MHWs and characterize their evolutions in both time and space. In the following section, we use *Ocetrac* to detect and follow four well-known MHWs occurring during the 21st Century, including the 2013–2017 Northeast Pacific (Bond et al. 2015, Di Lorenzo and Mantua, 2016), 2009–2011 Western Australia (Pearce and Feng, 2013), 2012 Gulf of Maine (Mills et al., 2013), and 2003 Mediterranean Sea (Black et al., 2004; Sparnocchia et al., 2006) MHWs.

3.6 Case Studies

Ocetrac provides a global dataset of MHW spatiotemporal metrics that we can then probe to explore how past events evolved (**Table 3.3).** Until now, tracking MHWs was performed on an adhoc basis. Here we explore these recent events and determine (1) if they are well captured by *Ocetrac* based on what we know from past literature, and (2) if there is anything new that can be learned about MHWs by taking into consideration their spatial connectivity. We focus on four events that had major impacts on both socioeconomic and ecological systems and that sample from unique geographical regions in both the tropics and midlatitudes.

Table 3.3 Spatiotemporal metrics using *Ocetrac* to describe four well-known and highly impactful 21st Century marine heatwaves.

Region	Start date	End date	Duration (months)	Intensity Mean (ºC) , Max. (ºC), Cumulative (ºC km^2 months)	Area (km^2) Mean, Max., Total	Centroids Total (max. per month)
Northeast Pacific	7/2013	11/2017	53	1.58 8.93 4.77x10^6	1.14x10^7 7.19x10^7 1.96x10^9	172 (9)
Gulf of Maine	4/2012	11/2012	8	1.49 3.68 9.42x10^4	4.14x10^6 6.05x10^6 3.31x10^7	8 (1)
West Coast of Australia	3/2009	5/2013	51	1.34 4.57 2.14x10^6	7.57x10^6 3.09x10^7 1.04x10^9	137 (5)
Mediterranean Sea	6/2003	8/2003	3	2.16 4.14 2.37x10^4	2.61x10^6 2.69x10^6 7.76x10^6	3 (1)

3.6.1 Northeast Pacific

A MHW, colloquially referred to as "The Blob", in the Northeast Pacific was notorious for its unusual scale and magnitude (Bond et al. 2015). MHW anomalies that developed in late 2013 were connected to the warm SSTs in the western tropical Pacific months prior through the excitation of atmospheric Rossby waves that weakened the mean state of atmospheric circulation over the North Pacific (Hartmann, 2015). This resulted in an exceptionally high ridge of atmospheric pressure through the winter of 2014 that weakened surface wind speeds, lowered rates of turbulent heat loss from the ocean to the atmosphere, and reduced the normal Ekman transport of cold water from the north (Bond et al., 2015). Offshore SST anomalies that formed during the boreal winter of 2013/14 made their way to the U.S. West Coast by late spring following the mean circulation of the ocean gyre (Di Lorenzo and Mantua, 2016). The MHW

lingered for several years along the coast and was strengthened equatorward by an extreme 2015/16 El Niño in the eastern equatorial Pacific (Tseng et al., 2017).

Pacific anomalies in 2013–2015 were dynamically linked through atmospheric variability and thermodynamic coupling that manifested on top of modes of North Pacific decadal SST variability (Tseng et al., 2017; Di Lorenzo and Mantua, 2016; Lee et al., 2015). We use *Ocetrac* to explore the spatial connectivity of Pacific anomalies during this multi-year event and track its evolution through time (**Figure 3.14**). We start by identifying the circular mass of anomalies just south of the Gulf of Alaska as described by Bond et al. (2015) that formed during late 2013. We trace these anomalies back to their origin as early as July 2013 in the western Tropical Pacific. The MHW was confined to the western and northeast Pacific through late 2014. SST anomalies in the Indian Ocean had been above average for most of 2014, which played a factor in the failed development of a major El Niño event in 2014/2015 (Dong and McPhaden, 2018; McPhaden, 2015). The warm background SSTs likely enabled the MHW to grow in the Indian Ocean and persist through 2015. Meanwhile, the North Pacific portion of this mega MHW resembled the spatial pattern of the positive Pacific Decadal Oscillation (PDO) in winter 2015 that extended from the Gulf of Alaska to the eastern tropical Pacific (**Figure 3.14**). Di Lorenzo and Mantau (2016) indeed showed that the weak El Niño of 2014/2015 provided the Aleutian Low with enough variability to drive this PDO-like expression of SST anomalies. This variability, along with increased heat content in the tropical Pacific, were important precursors to the development of the most powerful El Niño on record in 2015/2016.

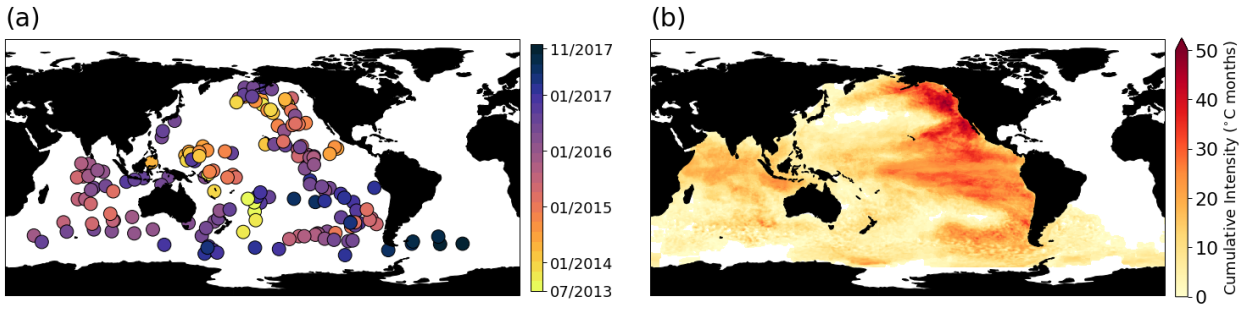

Figure 3.14 Spatiotemporal evolution of the Northeast Pacific "Blob" (event #617) from July 2013 through November 2017. Each circle in (a) represents the centroid of an object belonging to the MHW, where color corresponds to date. Colors in (b) show the cumulative intensity (ºC-months) over the entire footprint of the MHW (1.96×10^9 km^2). Data are from the monthly ¼º resolution OISSTv2 with the trend removed using a minimum area threshold of the 75th percentile and an edge detection radius of 8 grid spaces (~2º latitude and longitude).

3.6.2 Gulf of Maine

The so-called Gulf of Maine MHW in 2012 covered an ocean area from Cape Hatteras, North Carolina to Iceland and up into the Labrador Sea (**Figure 3.15**; Mills et al., 2013). A northward meridional shift in the atmospheric jet stream over North America during the late autumn and early winter of 2011/2012 stabilized atmospheric high pressure over the western North Atlantic (Chen et al., 2014). This led to an overall reduction in surface wind speeds and higher than normal air humidity and temperature, which acted to inhibit turbulent heat loss from the ocean to the atmosphere and increase water column stratification (Chen et al., 2014). As a result, SSTs systematically warmed over the continental shelf from November 2011 through at least June 2012 (Chen et al., 2014). Anomalous warming in the spring of 2012 was attributed to large-scale atmospheric variability during the winter of 2011/2012, whereas local advective heat flux played a secondary role to cool SSTs (Chen et al., 2014; 2015).

Our analysis shows that the Gulf of Maine MHW was indeed a regional event that impacted the Northwest Atlantic. The center of action was centered offshore of Newfoundland with maximum cumulative intensities occurring in the Gulf of Maine, Gulf of St. Lawrence, and part of the Labrador Sea (**Figure 3.15**). The MHW, which began in April 2012, persisted for 8 months and covered a total ocean area of 3.31×10^7 km^2 with a maximum intensity of 3.68ºC (**Table 3.2**).

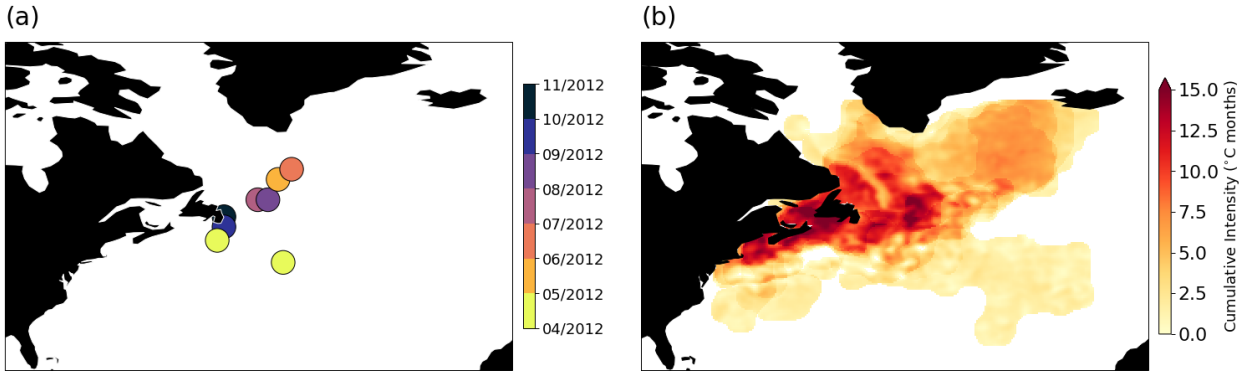

Figure 3.15 Spatiotemporal evolution of the Gulf of Maine (event #590) from April to November 2012. Each circle in (a) represents the centroid of an object belonging to the MHW, where color corresponds to date. Colors in (b) show the cumulative intensity (ºC-months) over the entire footprint of the MHW (3.31×10^7 km^2). Data are from the monthly ¼º resolution OISSTv2 with the trend removed using a minimum area threshold of the 75th percentile and an edge detection radius of 8 grid spaces (~2º latitude and longitude).

Scannell et al. (2016) also tracked the 2012 Gulf of Maine MHW using 2º-latitude by 2º-longitude resolution monthly detrended SST for three months, between June and August 2012, and found its area to be 7.60×10^6 km^2 with a maximum intensity exceeding 3ºC. They also showed that the likelihood of a MHW this size is enhanced during the negative phase of the North Atlantic Oscillation (NAO) and positive phase of the Atlantic Multidecadal Oscillation (AMO), with the AMO being more dominant. Unsurprisingly, the AMO had been positive since the early 1990s and the NAO took a negative excursion in 2012. The resulting relationship

between natural modes of SST variability and MWH size may have favored the large-scale nature of the 2012 warm anomalies.

3.6.3 West Coast of Australia

A major, unprecedented MHW occurred in late February 2011 off the coast of Western Australia (Pearce and Feng, 2013). An important driver of this MHW was the fast phase transition from Central Pacific El Niño in 2009/2010 to La Niña in 2010/2011 that was in part driven by strong easterly wind stress caused by warm SSTs in the Indian Ocean (Kim et al., 2011). Easterly wind anomalies in the western Tropical Pacific and over Indonesia excited an eastward upwelling Kelvin wave that quickly terminated warming associated with an El Niño in 2009/2010 (Kim et al., 2011; as described in Kug and Kang, 2006; Yoo et al., 2010). An extraordinary La Niña quickly ensued, which increased SSTs and sea level heights in the western tropical Pacific and off the northwest coast of Australia. High steric height anomalies forced a stronger than normal, poleward flowing Leeuwin Current (Feng et al., 2013). In addition, northerly wind anomalies associated with low sea level pressure anomalies off the coast of Western Australia helped to intensify the Leeuwin Current and reduce turbulent heat loss form the ocean (Feng et al., 2013). The poleward advection of warm water contributed to two thirds of the warming, while positive air-sea heat fluxes into the ocean accounted for approximately the other one third of the warming (Benthuysen et al., 2014). The anomalous air-sea heat flux in February 2011 acted to reinforce the MHW rather than damp the warming effects from La Niña (Feng et al., 2013). The exceptional MHW that resulted along Australia's western coast was dubbed 'Ningaloo Niño' for its semblance to other coupled ocean-atmosphere phenomena in the Pacific (El Niño) and

Atlantic (Benguela Niño) (Feng et al., 2013). After the peak warming in March 2011 along the coast, positive sea level and SST anomalies propagated offshore following the propagation of mesoscale eddies (Benthuysen et al., 2014).

Indian Ocean SSTs during the following summers of 2012 and 2013 remained anomalously warm off Western Australia (Caputi et al., 2014). The persistence of anomalies was part of an increasing trend of Ningaloo Niño conditions since the early 1990s (Feng et al. 2014). The trend was driven in part by a change to the negative phase of the Interdecadal Pacific Oscillation (IPO) and enhanced ENSO variance, the former sustains positive heat content anomalies off Western Australia and favors cyclonic wind anomalies that reduce the prevailing alongshore southerly winds and enhance poleward heat transport by the Leeuwin Current (Feng et al. 2014). Further coupling between the along-shore winds and coastal SST has been shown to amplify Ningaloo Niño events (Kataoka et al., 2014).

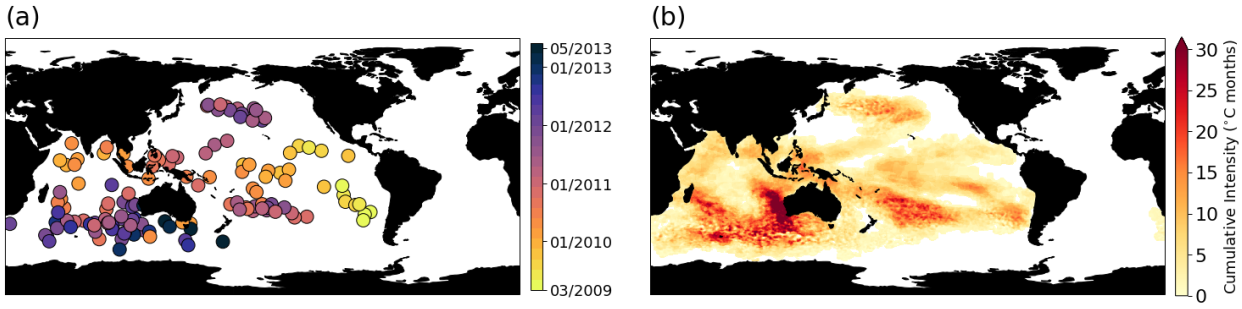

Figure 3.16 Spatiotemporal evolution of the Western Australia (event #553) from March 2009 through May 2013. Each circle in (a) represents the centroid of an object belonging to the MHW, where color corresponds to date. Colors in (b) show the cumulative intensity (ºC-months) over the entire footprint of the MHW (1.04×10^9 km^2). Data are from the monthly ¼º resolution OISSTv2 with the trend removed using a minimum area threshold of the 75th percentile and an edge detection radius of 8 grid spaces (~2º latitude and longitude).

3.6.4 Mediterranean Sea

During the summer of 2003, Western Europe experienced its worst heatwave in over 500 years, which caused excessive morbidity throughout the region, especially in hard hit France (Luterbacher et al., 2004; Valleron and Boumendil, 2004). The extremely hot conditions over land from May through August stemmed from a persistent anticyclonic circulation centered over northern France that reduced cloud cover and precipitation (Black et al. 2004, ; Grazzini et al., 2003). Although short-lived, the anomalous atmospheric anomalies quickly warmed SSTs in the central Mediterranean Sea in May before affecting the entire basin by July, with the exception of the Aegean Sea (Grazzini and Viterbo, 2003). The Medierannean Sea MHW warmed passively as a result of increased surface air temperatures, reduced surface wind speeds, and lower rates of turbulent and longwave heat loss to the atmosphere (Olita et al. 2007). The MHW dissipated abruptly in late August to early September when strong westerly winds cooled surface air temperatures and induced wind-driven turbulent mixing that cooled SSTs (Sparnocchia et al., 2006).

The Mediterranean Sea MHW in *Ocetrac* during the summer of 2003 started in June and persisted through August. Due to the nature of the semi-enclosed region, MHW anomalies in the Mediterranean Sea did not connect with those in the Atlantic and had only one centroid per month. This meant that the MHW was highly localized with maximum anomalies over 4ºC and a total surface area of 7.76×10^6 km^2, where the maximum cumulative anomalies occurred in the central and western regions of the basin (**Table 3.2, Figure 3.17b**). The 2003 Mediterranean Sea

MHW was the smallest size event of the four case studies examined here, however, was intense enough to decimate rocky benthic macroinvertebrate species (**Table 3.2**; Garrabou, et al. 2009).

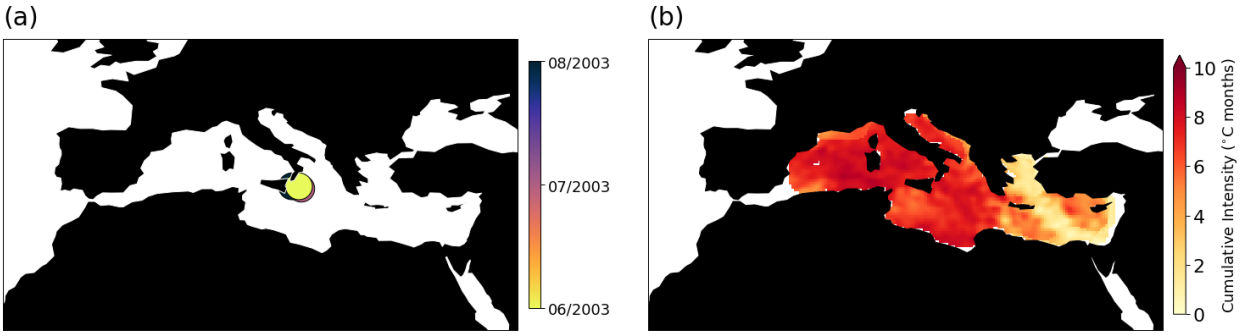

Figure 3.17 Spatiotemporal evolution of the Western Australia (event #429) from June through August 2003. Each circle in (a) represents the centroid of an object belonging to the MHW, where color corresponds to date. Colors in (b) show the cumulative intensity (ºC-months) over the entire footprint of the MHW (7.76×10^6 km^2). Data are from the monthly ¼º resolution OISSTv2 with the trend removed using a minimum area threshold of the 75th percentile and an edge detection radius of 8 grid spaces (~2º latitude and longitude).

Remote forcing from the northward shift and intensification of the Intertropical Convergence Zone over West Africa, as well as Rossby waves emanating from tropical America that intensified the Azores anticyclone, contributed to the unusual atmospheric conditions driving the 2003 Mediterranean Sea MHW (Black et al., 2004). Decadal fluctuations in North Atlantic SSTs and the thermohaline circulation are known to influence European weather over long timescales. During 2003, the AMO index was positive and associated with elevated air temperatures and reduced wind stress over western Europe (Sutton and Hodson, 2005).

3.7 Summary

We present a new tracking algorithm called *Octerac* that can be used to characterize the spatiotemporal evolution of MHWs globally. Previously, our understanding about the complex

spatial connectivity and temporal behavior of MHWs has been limited due to the lack of software able to detect and follow MHWs as they evolve. Using *Ocetrac*, we are able to characterize new spatial patterns and behavior of some of the most dangerous MHWs of the 21st Century. Our approach is threefold:

1. **Preprocess** global SSTs to exclude the long-term warming trend and define anomalies with respect to the local climatology. Anomalies are then standardized by the monthly standard deviation of SSTa over the entire climatological period. The climatological periods should cover at least the most recent 30-years.
2. **Detect** MHWs where SST exceed a local seasonally varying threshold (e.g., 90th percentile) computed over the same climatological period. Connect edges that define the perimeter of MHWs larger than a minimum size threshold (e.g., 75th percentile of the anomaly size distribution).
3. **Track** MHWs using 3D connectivity in both space (x,y) and time (z). Keeping track of multiple centroids as MHWs split or merge is a novel component of *Ocetrac*.

We demonstrate the usefulness of *Ocetrac* in following the evolutions of four MHWs in the Pacific, Indian, and Atlantic Oceans, as well as in the Mediterranean Sea. The advantage of using *Ocetrac* globally, rather than a single regionally focused analysis, is that it is designed to capture the large-scale and dynamically linked connections between remote SST anomalies that perpetuate MHWs. In combination with dynamical studies, *Ocetrac* can provide a tool to better understand the origin of MHWs and their evolution.

To a large extent, our interpretation of extreme events is dependent on how thresholds are defined. In many circumstances, extreme events are determined based on the space and time scales of their impacts and associated risks. For example, extreme flooding events are often classified by their extent and frequency in terms of their potential for damage (ten Veldhuis, 2011). It is therefore useful to consider MHWs as temperature variance outside the normal range of thermal tolerance to native species. For this reason, we remove the warming trend due to greenhouse gas emissions to better isolate the behavior of SST variance.

We also explore the sensitivity of *Ocetrac* to the resolution of gridded observational data, ranging from eddy-permitting (0.25º) to very coarse (2º). The overall large-scale spatial patterns agree well among the different resolutions, however the MHWs tracked with coarser resolution lacked the intensity and frequency expected with higher resolution. These results are consistent with modeling studies led by Hayashida et al. (2020) and Pilo et al. (2019), and agree that greater spatial detail gained from high resolution datasets better represent the changes expected to occur to MHWs in the future.

Understanding the spatiotemporal connectivity of MHWs and their underlying dynamical processes will ultimately guide the future development of forecasts to anticipate MHW risk, as well as improve preparedness in ecosystem management. Machine learning is a well-suited application of *Ocetrac*, and could be designed to leverage the spatiotemporal information to make predictions several months ahead. The inclusion of high-quality, near real time data will remain a challenge for making uptodate forecasts (Schlegel et al. 2019).

CONCLUSIONS

Since the first time the term 'Marine Heat Wave' (MHW) was coined in 2011, following the extreme warming event off Western Australia (Pearce et al., 2011), these events have become increasingly recognized to occur across a range of spatiotemporal scales. MHWs can be regionally confined, for example in the Northwest Atlantic (Chen et al., 2014; 2015) and Mediterranean Sea (Olita et al., 2006), or they can be broadly distributed and span multiple ocean basins, where they are often associated with the El Niño-Southern Oscillation (ENSO) (Di Lorenzo and Mantua, 2016; Feng et al., 2013). MHWs can persist on scales from weeks (Pearce and Feng, 2013) to multiple years (Di Lorenzo and Mantua, 2016), and linger in the subsurface (Jackson et al., 2018). Within the past 10 years, there has been an incredible growth in the appreciation and understanding of MHWs, including their physical drivers and characteristics, ecological impacts, socioeconomic implications, and the effects of anthropogenic warming on these extreme events (Benthuysen et al., 2018).

This dissertation contributes to the wealth of knowledge on the drivers, persistence, and evolution of MHWs globally, and more generally sea surface temperature (SST) variability. The first chapter (Scannell and McPhaden, 2018) diagnoses the drivers of the seasonal cycle of SST variability in the eastern Tropical Atlantic using a mixed layer heat budget with 5-years of observations collected from an ocean mooring at 6ºS, 8ºE that is part of the Prediction and

Research Moored Array in the Tropical Atlantic (PIRATA; Bourlès et al., 2008). Historically, this region in the southeastern edge of the Tropical Atlantic cold tongue suffers from large SST biases in global climate models that are too warm compared with observations (Zuidema et al., 2016). This problem is particularly widespread amongst the 5th phase of the Coupled Model Intercomparison Project, as well as in earlier model generations. Our study uses observations to describe the seasonal evolution of mixed layer temperature, which has two pronounced regimes: warm-fresh from December through April, and cold-salty May through September.

During the warm-fresh regime, solar heating is very effective in warming SST due to an increase in near-surface stratification and shallow mixed layers. The mixed layer heat balance during this time is dominated by shortwave radiation. Conversely, in the cool and salty regime, the southeasterly Trades intensify in response to the onset of the West African Monsoon and the displacement of the ITCZ further north. This enhances local evaporative cooling and upwelling along the African coast as well as along and south of the equator. As a result, the mixed layer shoals in August, where cool and salty water is entrained into the mixed layer.

The cool SSTs in August stabilize the shallow stratocumulus cloud deck along the eastern boundary, shielding the ocean surface from downwelling shortwave radiation, which is at a minimum at this time of year. These findings indicate that the distribution of SST is highly sensitive to surface fluxes in the southeastern tropical Atlantic where the most severe climate model biases occur. In particular, absorbed shortwave radiation is dependent on low-level cloud cover, which is often misrepresented in global climate models (Zuidema et al., 2016). We

concluded that an underestimation of low level marine stratocumulus cloud deck allows excessive absorption of shortwave radiation to reach the sea surface and contributes strongly to the SST warm biases in the eastern tropical Atlantic. The underrepresentation of clouds may be further amplified by insufficient turbulent vertical mixing of cold water across the base of the mixed layer that cools SST in August. The biases in modeled SST undermine efforts to accurately simulate regional and global climate variability, including MHWs where their likelihoods are expected to increase under continued anthropogenic warming (Frölicher et al., 2018; Nnamchi et al., 2015).

Chapter two of this dissertation describes the subsurface persistence and evolution of recent MHWs in the Northeast Pacific using subsurface observations from Argo. In particular, we compare and contrast two long-lived MHWs occuring in 2013–2016 and 2019–2020, colloquially referred to as The Blob (Bond et al., 2015) and Blob2.0 (Amaya et al., 2020). We explore the connections between surface MHWs and the subsurface structure of temperature, salinity, and density on both isobars and isopycnals, and speculate on the roles that detrainment, diabatic subduction, and adiabatic isopycnal heave may have in the sequestration of MHW anomalies into the permanent pycnocline where they can persist for years (Jackson et al. 2018).

A significant finding was the propagation and persistence of 2019 anomalies into the subsurface, although a strong freshwater signal increased the buoyancy of the surface layer and prevented anomalies from penetrating as deeply as the 2013–2016 MHW. Regardless, a buildup of subsurface heat content was observed through 2020 and may help prolong the duration of this

event into 2021. Furthermore, the confinement of warm anomalies to the near-surface likely helped to enhance the MHW's intensity.

Understanding the subsurface evolution and persistence of MHWs gives insight into the potential predictability and reemergence of these events in the future, where a trend towards shallower summertime MLDs is expected to increase the likelihood and frequency of MHWs in the North Pacific (Amaya et al., in review). As future warming trends favor a more stratified upper ocean (Li et al., 2020), we expect that detrainment out of the mixed layer may become less effective in storing MHW anomalies in the subsurface, and therefore further amplify surface warming. This possibility is concerning owing to the impacts that accumulated heat stress and stratification have on pelagic marine ecosystems and primary production (Smale et al, 2019; Cavole et al., 2016; Jacox et al., 2016).

The third chapter presents a novel tracking algorithm, termed *Ocetrac*, that characterizes the spatiotemporal evolution of MHW globally. *Ocetrac* is flexibly designed to incorporate SST from gridded datasets and extracts MHW according to a specified threshold. There are three components of *Ocetrac* that include preprocessing SST anomalies, detecting MHWs based on intensity and size criteria, and tracking MHWs in both 2D space and time. We describe the sensitivities to how MHWs are tracked including the spatial resolution of the data, whether or not the trend is retained or removed, and the choice of intensity and size parameters. The overall large-scale spatial patterns agree well among resolutions ranging from 0.25º to 2º, however the MHWs tracked with coarser resolution lacked the intensity and frequency expected with higher

resolution. Using a 99th percentile to define MHWs, compared to the 90th, resulted in shorter duration and smaller sized MHWs. Knowing the sensitivities of these criteria allows users to choose data products and thresholds most appropriate for their research application.

We test the use of *Ocetrac* on four well-known MHWs occuring in the Pacific, Indian, and Atlantic Oceans, as well as in the Mediterranean Sea. We found that two of these MHW, occurring between 2013–2017 and 2009–2013 encompassed multiple basins and were connected to anomalies associated with ENSO variability. These examples highlight the role of teleconnections and remote drivers in the connectivity of MHWs globally, which may lend to predictability. Two other MHWs occuring in the Northwest Atlantic in 2012 and in the Mediterranean Sea in 2003 are described as regional events encompassing a smaller area for a shorter period of time.

The advantage of using *Ocetrac* globally, rather than using a single regionally focused analysis, is that it is designed to capture the large-scale and dynamically linked connections between remote SST anomalies that perpetuate MHWs. Paired with dynamical studies, *Ocetrac* can provide a tool to better understand the origin of MHWs, their evolution, and perhaps predictability.

In combination, these three chapters describe new patterns in the spatiotemporal evolution of MHWs that are aimed to improve their eventual prediction (Chapters 2 & 3) and representation in global climate models (Chapter 1). Chapter 3 will also provide a new open-source python

package using ideas from image processing to aid oceanographers in the analysis of anomaly detection and tracking. This package could eventually be modified to also quantify the spatiotemporal evolution of other extreme phenomena that are known to negatively impact ecosystems (e.g., harmful algal blooms, low oxygen, and acidic events) by incorporating biogeochemical data and satellite imagery. Anticipating the paths of destructive MHWs will provide a warning for fishers, fishery managers, and aquaculture farmers, and will help to guide scientists on the deployment of in-situ autonomous instruments (e.g., ocean gliders, pH sensors, sail drones, and profiling floats), as well as the design of biological surveying to better monitor, and predict the impacts from these deadly events.

Building from this dissertation, some immediate avenues of continued research will be to more closely examine the relationships between MHWs and ENSO, particularly as they relate to MHW intensity, duration, size, and frequency. The pace of MHW research has rapidly evolved in the direction of attributing the severity of events to anthropogenic climate change. Indeed this is a worthwhile research direction, however, there has not yet been a thorough study done to evaluate the role of ENSO in MHW variability, which has often been overlooked. Given that ENSO is at least somewhat deterministic, building these linkages between MHWs and tropical Pacific variability may be the most promising path toward near-term prediction.

Another avenue for future research is the evaluation of MHWs in global climate models benchmarked against observations. In Chapter 1, we showed that cloud radiative feedbacks and the strength of turbulent mixing are critically important processes to the seasonal variability of

SST in the Southeast Tropical Atlantic (Scannel and McPhaden, 2018). In most climate models, the incorrect parametrization clouds can lead to warm biases in SST may incorrectly represent MHWs (such as the Atlantic Niño and Bengula Niño). To quantify the significance of various factors in coupled climate models that lead to systematic warm biases in the eastern tropical Atlantic, model-based mixed layer heat budget analyses complimentary to Chapter 1 are needed. Lastly, mixed layer heat budgets are frequently used to diagnose the drivers of surface warming associated with MHWs; however, we found in Chapter 2 that near surface stratification and subsurface water properties are equally important to consider. Future work quantifying the role and drivers of subsurface salinity and temperature would help to better understand the ocean's role in the persistence and evolution of long-lived events.

Appendix

A. TITLES AND ABSTRACTS OF CO-AUTHORED PAPERS

[2016] A Hierarchical Approach to Defining Marine Heatwaves

Hobday, A. J., Alexander, L. V., Perkins, S. E., Smale, D. A., Straub, S. C., Oliver, E. C. J., Benthuysen, J. A., Burrows, M. T., Donat, M. G., Feng, M., Holbrook, N. J., Moore, P. J., Scannell, H. A., Sen Gupta, A., & Wernberg, T. (2016). A hierarchical approach to defining marine heatwaves. *Progress in Oceanography*, 141, 227-238. doi:10.1016/j.pocean.2015.12.014

Marine heatwaves (MHWs) have been observed around the world and are expected to increase in intensity and frequency under anthropogenic climate change. A variety of impacts have been associated with these anomalous events, including shifts in species ranges, local extinctions and economic impacts on seafood industries through declines in important fishery species and impacts on aquaculture. Extreme temperatures are increasingly seen as important influences on biological systems, yet a consistent definition of MHWs does not exist. A clear definition will facilitate retrospective comparisons between MHWs, enabling the synthesis and a mechanistic understanding of the role of MHWs in marine ecosystems. Building on research into atmospheric heatwaves, we propose both a general and specific definition for MHWs, based on a hierarchy of metrics that allow for different data sets to be used in identifying MHWs. We generally define a MHW as a prolonged discrete anomalously warm water event that can be described by its duration, intensity, rate of evolution, and spatial extent. Specifically, we consider an anomalously warm event to be a MHW if it lasts for five or more days, with temperatures warmer than the 90th percentile based on a 30-year historical baseline period. This structure provides flexibility with regard to the description of MHWs and transparency in communicating MHWs to a general audience. The use of these metrics is illustrated for three 21st century MHWs; the northern Mediterranean event in 2003, the Western Australia 'Ningaloo Niño' in 2011, and the northwest Atlantic event in 2012. We recommend a specific quantitative definition for MHWs to facilitate global comparisons and to advance our understanding of these phenomena.

[2016] Frequency of Marine Heatwaves in the North Atlantic and North Pacific since 1950

Scannell, H. A., Pershing, A. J., Alexander, M. A., Thomas, A. C., & Mills, K. E. (2016). Frequency of marine heatwaves in the North Atlantic and North Pacific since 1950, *Geophys. Res. Lett.*, 43. doi:10.1002/2015GL067308

Extreme and large‐scale warming events in the ocean have been dubbed marine heatwaves, and these have been documented in both the Northern and Southern Hemispheres. This paper examines the intensity, duration, and frequency of positive sea surface temperature anomalies in the North Atlantic and North Pacific Oceans over the period 1950–2014 using an objective definition for marine heatwaves based on their probability of occurrence. Small‐area anomalies occur more frequently than large‐area anomalies, and this relationship can be characterized by a

power law distribution. The relative frequency of large- versus small-area anomalies, represented by the power law slope parameter, is modulated by basin-scale modes of natural climate variability and anthropogenic warming. Findings suggest that the probability of marine heatwaves is a trade-off between size, intensity, and duration and that region specific variability modulates the frequency of these events.

[2018] Longer and More Frequent Marine Heatwaves over the Past Century

Oliver, E. C. J., Donat, M. G., Burrows, M. T., Moore, P. J., Smale, D. A., Alexander, L. V., Benthuysen, J. A., Feng, M., Sen Gupta, A., Hobday, A. J., Holbrook, N. J., Perkins-Kirkpatrick, S. E., Scannell, H. A., Straub, S. C. & Wernberg, T. (2018). Longer and more frequent marine heatwaves over the past century, *Nature Communications*, 9, 1324, doi:10.1038/s41467-018-03732-9

Heatwaves are important climatic extremes in atmospheric and oceanic systems that can have devastating and long-term impacts on ecosystems, with subsequent socioeconomic consequences. Recent prominent marine heatwaves have attracted considerable scientific and public interest. Despite this, a comprehensive assessment of how these ocean temperature extremes have been changing globally is missing. Using a range of ocean temperature data including global records of daily satellite observations, daily in situ measurements and gridded monthly in situ-based data sets, we identify significant increases in marine heatwaves over the past century. We find that from 1925 to 2016, global average marine heatwave frequency and duration increased by 34% and 17%, respectively, resulting in a 54% increase in annual marine heatwave days globally. Importantly, these trends can largely be explained by increases in mean ocean temperatures, suggesting that we can expect further increases in marine heatwave days under continued global warming.

[2019] Marine Heatwaves threaten Global Biodiversity and the Provision of Ecosystem Services

Smale, D. A., Wernberg, T., Oliver, E. C. J., Thomsen, M., Harvey, B. P., Straub, S. C., Burrows, M. T., Alexander, L. V., Benthuysen, J. A., Donat, M. G., Feng, M., Hobday, A. J., Holbrook, N. J., Perkins-Kirkpatrick, S. E., Scannell, H. A., Sen Gupta, A., Payne, B. L. & Moore, P. J. (2019). Marine heatwaves threaten global biodiversity and the provision of ecosystem services, *Nature Climate Change*, 9, 306-312. doi:10.1038/s41558-019-0412-1

The global ocean has warmed substantially over the past century, with far-reaching implications for marine ecosystems1. Concurrent with long-term persistent warming, discrete periods of extreme regional ocean warming (marine heatwaves, MHWs) have increased in frequency2. Here we quantify trends and attributes of MHWs across all ocean basins and examine their biological impacts from species to ecosystems. Multiple regions in the Pacific, Atlantic and Indian Oceans are particularly vulnerable to MHW intensification, due to the co-existence of high levels of biodiversity, a prevalence of species found at their warm range edges or concurrent non-climatic human impacts. The physical attributes of prominent MHWs varied considerably, but all had deleterious impacts across a range of biological processes and taxa, including critical

foundation species (corals, seagrasses and kelps). MHWs, which will probably intensify with anthropogenic climate change, are rapidly emerging as forceful agents of disturbance with the capacity to restructure entire ecosystems and disrupt the provision of ecological goods and services in coming decades.

[2019] A Global Assessment of Marine Heatwaves and their Drivers

Holbrook, N. J., Scannell, H. A., Sen Gupta, A, Benthuysen, J. A., Feng, M., Oliver, E. C. J., Alexander, L. V., Burrows, M. T., Donat, M. G., Hobday, A. J., Moore, P. J., Perkins-Kirkpatrick, S. E., Smale, D. A., Straub, S. C., & Wernberg, T. (2019). A global assessment of marine heatwaves and their drivers. *Nature Communications*, 10, 2624. doi:10.1038/s41467-019-10206-z

Marine heatwaves (MHWs) can cause devastating impacts to marine life. Despite the serious consequences of MHWs, our understanding of their drivers is largely based on isolated case studies rather than any systematic unifying assessment. Here we provide the first global assessment under a consistent framework by combining a confidence assessment of the historical refereed literature from 1950 to February 2016, together with the analysis of MHWs determined from daily satellite sea surface temperatures from 1982–2016, to identify the important local processes, large-scale climate modes and teleconnections that are associated with MHWs regionally. Clear patterns emerge, including coherent relationships between enhanced or suppressed MHW occurrences with the dominant climate modes across most regions of the globe – an important exception being western boundary current regions where reports of MHW events are few and ocean-climate relationships are complex. These results provide a global baseline for future MHW process and prediction studies.

[2020] Keeping Pace with Marine Heatwaves

Holbrook, N. J., Sen Gupta, A., Oliver, E. C. J., Hobday, A. J., Benthuysen, J. A., Scannell, H. A., Smale, D. A., & Wernberg, T. (2020). Keeping pace with marine heatwaves. *Nature Reviews Earth & Environment*, 1, 482–493. doi:10.1038/s43017-020-0068-4

Marine heatwaves (MHWs) are prolonged extreme oceanic warm water events. They can have devastating impacts on marine ecosystems — for example, causing mass coral bleaching and substantial declines in kelp forests and seagrass meadows — with implications for the provision of ecological goods and services. Effective adaptation and mitigation efforts by marine managers can benefit from improved MHW predictions, which at present are inadequate. In this Perspective, we explore MHW predictability on short-term, interannual to decadal, and centennial timescales, focusing on the physical processes that offer prediction. While there may be potential predictability of MHWs days to years in advance, accuracy will vary dramatically depending on the regions and drivers. Skilful MHW prediction has the potential to provide critical information and guidance for marine conservation, fisheries and aquaculture management. However, to develop effective prediction systems, better understanding is needed of the physical drivers, subsurface MHWs, and predictability limits.

[2020] Drivers and impacts of the most extreme marine heatwaves events

Sen Gupta, A., Thomsen, M., Benthuysen, J. A., Hobday, A. J., Oliver, E. C. J., Alexander, L. V., Burrows, M. T., Donat, M. G., Feng, M., Holbrook, N. J., Perkins-Kirkpatrick, S., Moore, P. J., Rodrigues, R. R., Scannell, H. A., Tascheto, A. S., Ummenhofer, C. C., Wernberg, T. & Smale, D. A. (2020). Drivers and impacts of the most extreme marine heatwaves events. Scientific Reports, 10, 19359. https://doi.org/10.1038/s41598-020-75445-3

Prolonged high-temperature extreme events in the ocean, marine heatwaves, can have severe and long-lasting impacts on marine ecosystems, fisheries and associated services. This study applies a marine heatwave framework to analyze a global sea surface temperature product and identify the most extreme events, based on their intensity, spatial extent, and duration. Many of these events have yet to be described in terms of their physical attributes, generation mechanisms, or ecological impacts. Our synthesis identifies commonalities between marine heatwave characteristics and seasonality, links to the El Niño-Southern Oscillation, triggering processes and impacts on ocean productivity. The most intense events preferentially occur in summer, when climatological oceanic mixed layers are shallow and winds are weak, but at a time preceding climatological maximum sea surface temperatures. Most subtropical extreme marine heatwaves were triggered by persistent atmospheric high-pressure systems and anomalously weak wind speeds, associated with increased insolation, and reduced ocean heat losses. Furthermore, the most extreme events tended to coincide with reduced chlorophyll-a concentration at low and mid-latitudes. Understanding the importance of the oceanic background state, local and remote drivers and the ocean productivity response from past events are critical steps toward improving predictions of future MHW and their impacts.

B. MIXED LAYER DEPTH CORRECTION USING ARGO FLOATS

The calculation of mixed layer depth (MLD) is adjusted using 186 temperature and salinity profiles from neighboring Argo floats with ±2° latitude and longitude of 6°S, 8°E. Compared to the relatively coarse vertical resolution of PIRATA near the surface (1, 5, 10, 20, 40 m for temperature and salinity), Argo has a vertical sampling scheme of ~2 dbar in the upper 50 m. Buoy temperature and salinity data from 3 m were not used for this correction because of the short record of observations at 3 m for comparison with the Argo profiles. Argo accuracy is ±0.005 °C, ±0.01 salinity units, and 2.5 dbar for subsurface temperature, salinity, and pressure, respectively (Riser et al., 2016).

We compare MLDs using a density‐defined criteria of a 0.08 kg/m3 density equivalent increase from a 1‐m reference level (section 2.2) using subsampled Argo data at the PIRATA sampling depths and the full‐resolution Argo data (Figure A1). We use a least squares fit linear regression to quantify the error in MLD computed using the more coarsely resolved PIRATA data (Figure A2). Subsampled Argo data on average yield mixed layers that are 18% too shallow with a constant offset of 0.62 m. We correct the PIRATA mixed layer depths at 6°S, 8°E using a regression equation based on the Argo data. Once applied to the PIRATA data, this becomes an adjusted mixed layer depth used throughout the remainder of the analysis (Figure A1). The root‐mean‐square errors in the adjusted PIRATA MLDs compared to the MLDs computed using the full Argo resolution are 1.25 m in the upper 5 m, 1.25 m between 5 and 10 m, 2.07 m between 10 and 20 m, and 2.92 m between 20 and 30 m.

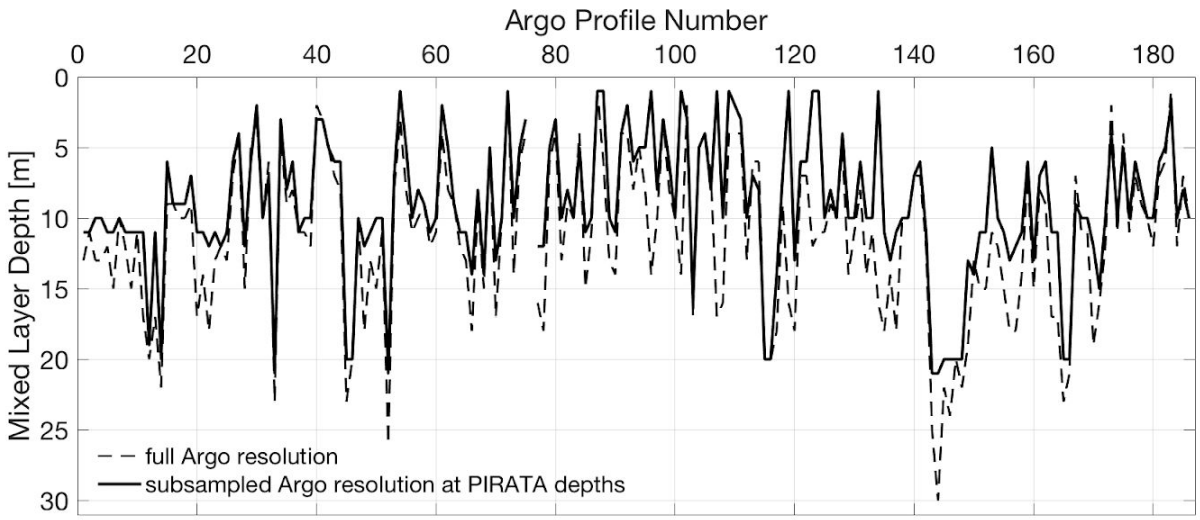

Figure A1.1 Comparison of Argo profile mixed layer depths and the adjusted mixed layer depth using the regression relationship between data at high and coarse vertical resolution.

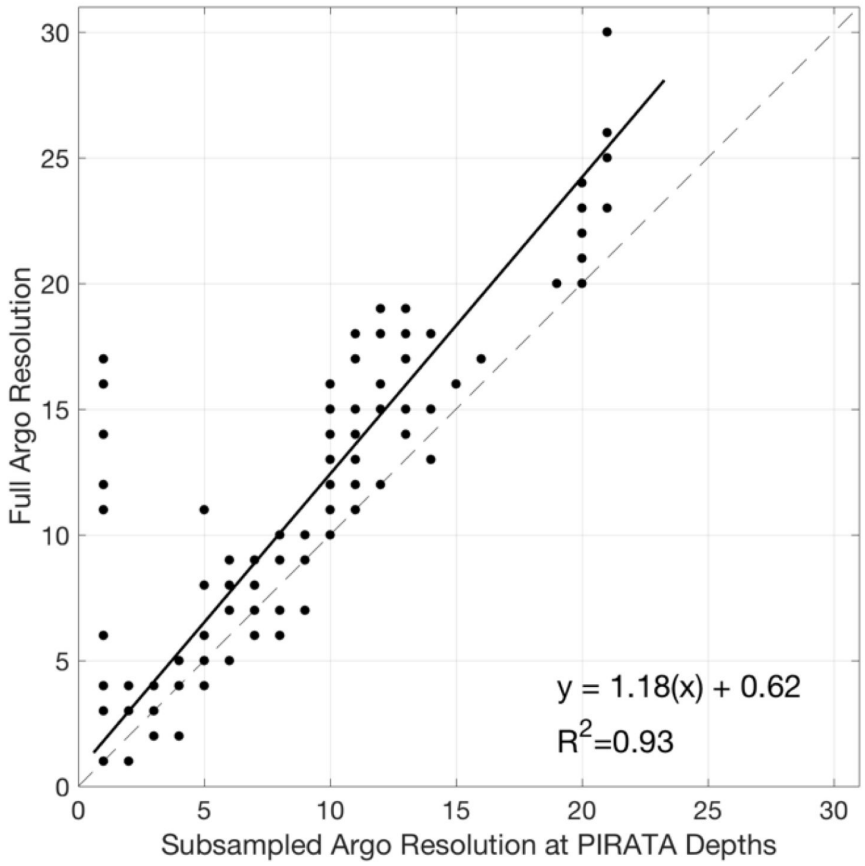

Figure A1.2 Linear regression of mixed layer depth between Argo profiles at full vertical resolution and Argo profiles subsampled at Prediction and Research Moored Array in the Atlantic depths.

C. OCETRAC SENSITIVITY ANALYSIS

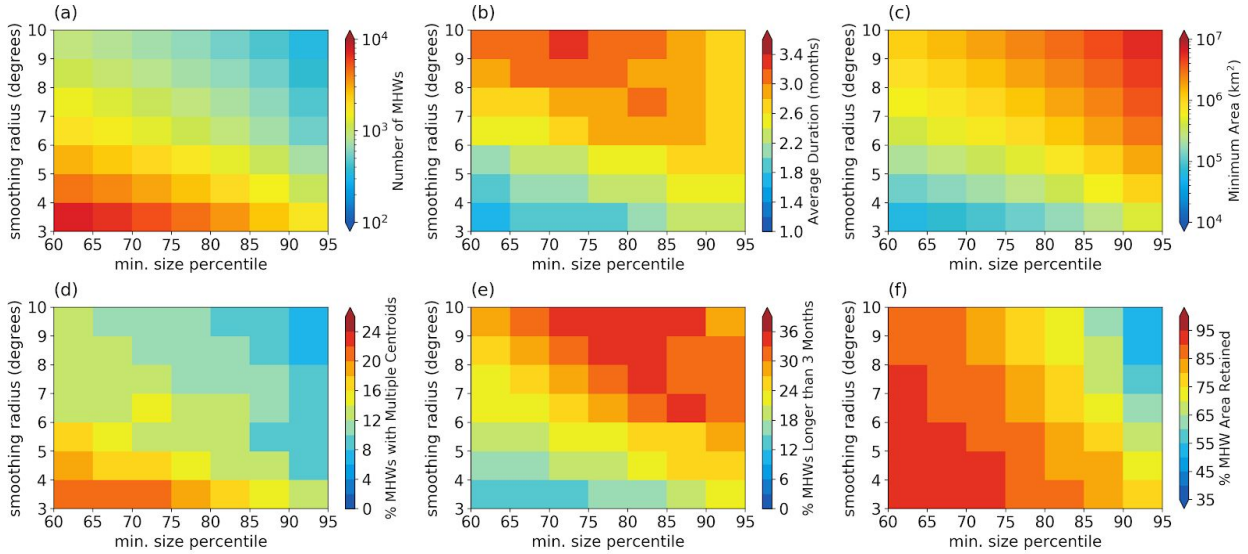

Figure C1.1 Sensitivity analysis for MHWs exceeding the local monthly 90th temperature percentile from the detrended 1/4º resolution OISSTv2 (T90_NoTrend_0.25_OISSTv2).

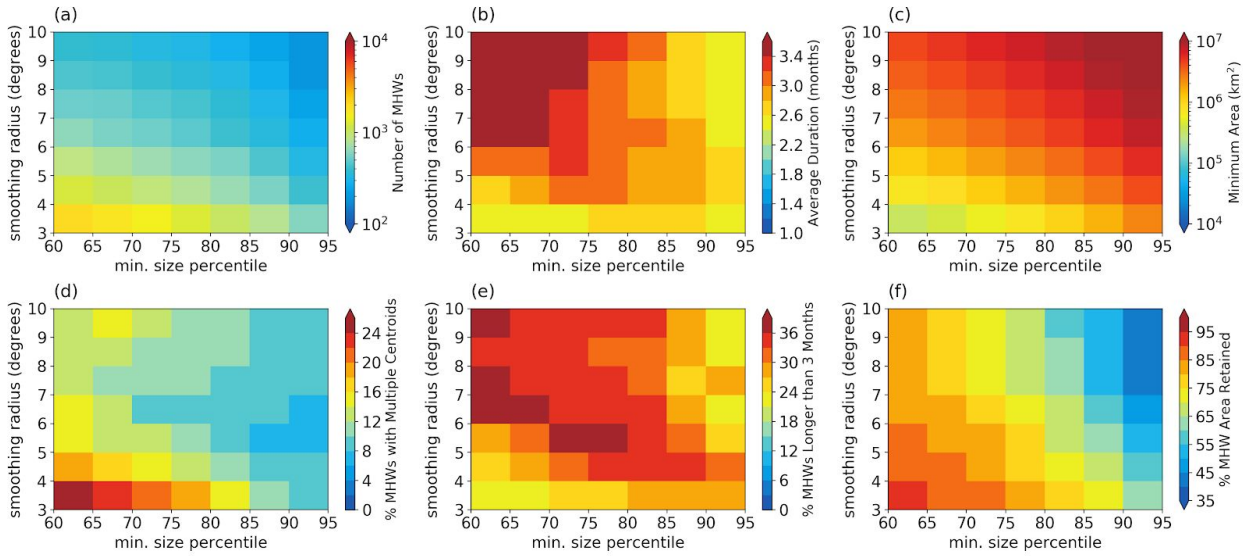

Figure C1.2 Sensitivity analysis for MHWs exceeding the local monthly 90th temperature percentile from the detrended 1/2º resolution OISSTv2 (T90_NoTrend_0.50_OISSTv2).

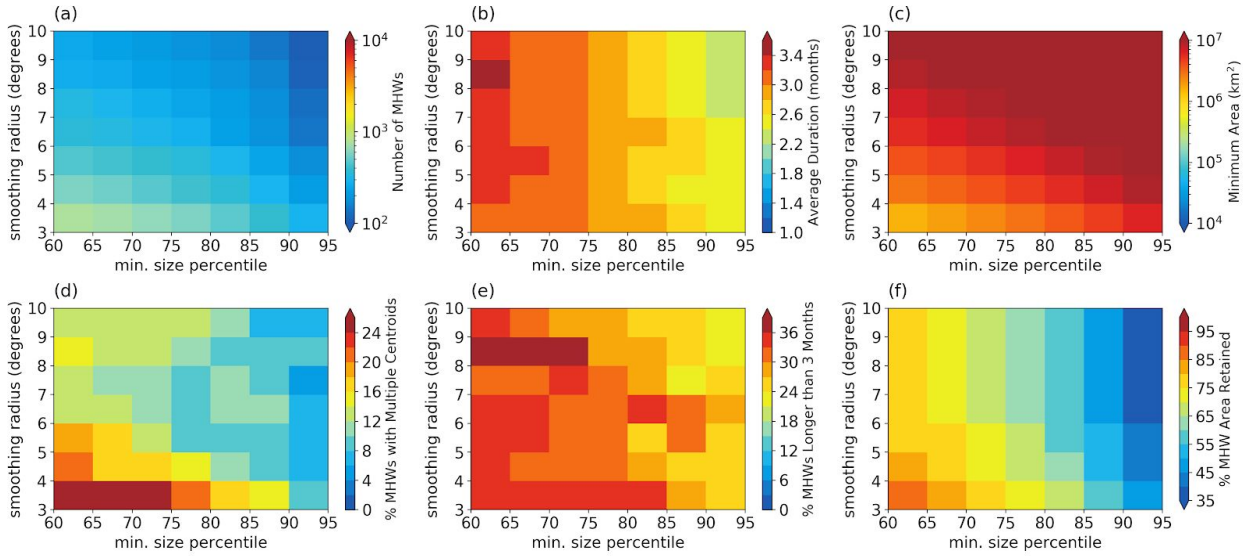

Figure C1.3 Sensitivity analysis for MHWs exceeding the local monthly 90th temperature percentile from the detrended 1º resolution OISSTv2 (T90_NoTrend_1.00_OISSTv2).

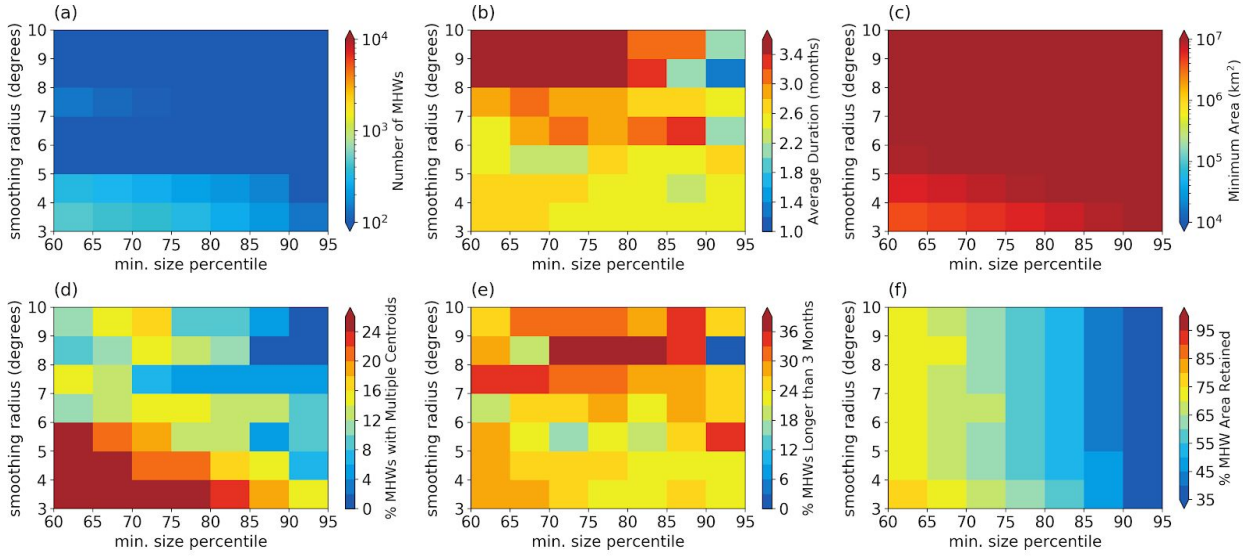

Figure C1.4 Sensitivity analysis for MHWs exceeding the local monthly 90th temperature percentile from the detrended 2º resolution OISSTv2 (T90_NoTrend_2.00_OISSTv2).

BIBLIOGRAPHY

A'Hearn, P. N., Freitag, H. P., & McPhaden, M. J. (2002). ATLAS module temperature bias due to solar heating (*NOAA Technical Memorandum OAR PMEL-121*). Seattle, WA: NOAA Pacific Marine Environmental Laboratory.

Alexander, M. A., Deser, C., & Timlin, M. S. (1999). The Reemergence of SST Anomalies in the North Pacific Ocean. *Journal of Climate*, 12, 2419–2433. doi:10.1175/1520-0442(1999)012<2419:TROSAI>2.0.CO;2

Amaya, D. J., Alexander, M. A., Capotondi, A., Deser, C., Karnauskas, K. B., Miller, A. J., & Mantua, N., Are long-term changes in mixed layer depth impacting North Pacific marine heatwaves? *Bulletin of the American Meteorological Society*. In review

Amaya, D. J., A. J. Miller, S. Xie, & Kosaka, Y. (2020). Physical drivers of the summer 2019 North Pacific marine heatwave. *Nature Communications*, 11, 1903. doi:10.1038/s41467-020-15820-w

Bachèlery, M. -L., Illig, S., & Dadou, I. (2016). Interannual variability in the South-East Atlantic Ocean, focusing on the Benguela Upwelling System: Remote versus local forcing. *Journal of Geophysical Research Oceans*, 121, 284–310. doi:10.1002/2015JC011168

Badescu, V. (1997). Verification of some very simple clear and cloudy sky models to evaluate global solar irradiance. *Solar Energy*, 61(4), 251-264. doi:10.1016/S0038-092X(97)00057-1

Benthuysen, J., Feng, M. & Zhong, L. (2014). Spatial patterns of warming off Western Australia during the 2011 Ningaloo Niño : Quantifying impacts of remote and local forcing. *Continental Shelf Research,* 91, 232–246 (2014). doi:10.1016/j.csr.2014.09.014

Benthuysen, J., Feng, M. & Zhong, L. (2014). Spatial patterns of warming off Western Australia during the 2011 Ningaloo Niño : Quantifying impacts of remote and local forcing. *Continental Shelf Research.* **91,** 232–246. doi:10.1016/j.csr.2014.09.014

Bindoff, N. L., & McDougall, T. J. (1994). Diagnosing Climate Change and Ocean Ventilation Using Hydrographic Data, *Journal of Physical Oceanography*, 24, 1137-1152. doi:10.1175/1520-0485(1994)024<1137:DCCAOV>2.0.CO;2

Black, E., Blackburn, M., Harrison, R. G., Hoskins, B. J. & Methven, J. (2004). Factors contributing to the summer 2003 European heatwave, *Weather*, 59, 217–223, doi:10.1256/wea.74.04

Bond, N. A., Cronin, M. F., Freeland, H., & Mantua, N. (2015). Causes and impacts of the 2014 warm anomaly in the NE Pacific. *Geophysical Research Letters*, 42(9), 3414-3420. doi:10.1002/2015GL063306

Bourles, B., Lumpkin, R., McPhaden, M. J., Hernandez, F., Nobre, R., Campos, E., et al. (2008). The PIRATA program history, accomplishments, and future direction. *Bulletin of the American Meteorological Society*, 89(8),1111-1125. doi:10.1175/2008BAMS2462.1

Boutin, J., Chao, Y., Asher, W. E., Delcroix, T., Drucker, R., Drushka, K., et al. (2016). Satellite and in situ salinity understanding near-surface stratification and subfootprint variability. *Bulletin of the American Meteorological Society*, 97, 1391-1407. doi:10.1175/BAMS-D-15-00032.1

Behrens, E., Fernandez, D., & Sutton, P. (2019). Meridional oceanic heat transport influences marine heatwaves in the Tasman Sea on interannual to decadal timescales. *Frontiers in Marine Science*, 6, 228. doi:10.3389/fmars.2019.00228

Benthuysen, J. A., Oliver, E. C. J., Chen, K.. & Wernberg, T. (2020). Editorial: Advances in Understanding Marine Heatwaves and Their Impacts. *Frontiers in Marine Science*, 7:147. doi:10.3389/fmars.2020.00147

Bryden, H. L., & Brady, E. C. (1985). Diagnostic model of the three dimensional circulation in the upper equatorial Pacific Ocean. *Journal of Physical Oceanography*, 15, 1255–1273. doi:10.1175/1520-0485(1985)015<1255:DMOTTD>2.0.CO;2

Camara, I., Kolodziejczyk, N., Mignot, J., Lazar, A., & Gaye, A. T. (2015). On the seasonal variations of salinity of the tropical Atlantic mixed layer. *Journal of Geophysical Research Oceans*, 120, 4441– 4462. doi:10.1002/2015JC010865

Caputi, N., G, J., Peace, A., Jackson, G. & Pearce, A. (2014). The marine heat wave off Western Australia during the summer of 2010/11 – 2 years on. Fisheries Research Report [Western Australia. doi:ISBN 9781921845253

Caputi, N., Kangas, M., Denham, A., Feng, M., Pearce, A., Hetzel, Y., & Chandrapavan, A. (2016). Management adaptation of invertebrate fisheries to an extreme marine heat wave event at a global warming hot spot, *Ecology and Evolution*, 6, 3583–3593. doi:https://doi.org/10.1002/ece3.2137

Carton, J. A., & Zhou, Z. X. (1997). Annual cycle of sea surface temperature in the tropical Atlantic Ocean. *Journal of Geophysical Research*, 102(C13), 27813–27824. doi:10.1029/97JC02197

Cavole, L. M., Demko, A. M., Diner, R. E., Giddings, A., Koester, I., Pagniello, C. M. L. S., Paulsen, M. -L., Ramirez-Valdez, A., Schwenck, S. M., Yen, N. K., Zill, M. E., & Franks, P. J. S. (2016). Biological impacts of the 2013–2015 warm-water anomaly in the Northeast Pacific: Winners, losers, and the future. *Oceanography*, 29(2), 273–285. doi:10.5670/oceanog.2016.32

Chang, P. (1993). Seasonal cycle of sea surface temperature and mixed layer heat budget in the tropical Pacific Ocean. *Geophysical Research Letters*, 20(91), 2079–2082. doi:10.1029/93GL02374

Chen, K., Gawarkiewicz, G. G., Lentz, S. J., & Bane, J. M. (2014). Diagnosing the warming of the Northeastern U.S. Coastal Ocean in 2012: A linkage between the atmospheric jet stream variability and ocean response, *Journal of Geophysical Research-Oceans*, 119, 218– 227. doi:10.1002/2013JC009393.

Chen, K., Gawarkiewicz, G., Kwon, Y.-O. & Zhang, W. (2015). The role of atmospheric forcing versus ocean advection during the extreme warming of the Northeast U.S. continental shelf in 2012. *Journal of Geophysical Research-Ocean*. 120, 4324–4339. doi:10.1002/2014JC010547

Collins M., M. Sutherland, L. Bouwer, S.-M. Cheong, T. Frölicher, H. Jacot Des Combes, M. Koll Roxy, I. Losada, K. McInnes, B. Ratter, E. Rivera-Arriaga, R.D. Susanto, D. Swingedouw, & L. Tibig, 2019: Extremes, Abrupt Changes and Managing Risk. In: IPCC Special Report on the Ocean and Cryosphere in a Changing Climate [H.-O. Pörtner, D.C. Roberts, V. Masson-Delmotte, P. Zhai, M. Tignor, E. Poloczanska, K. Mintenbeck, A. Alegría, M. Nicolai, A. Okem, J. Petzold, B. Rama, N.M. Weyer (eds.)]. In press.

Cronin, M. F., & McPhaden, M. J. (1997). The upper ocean heat balance in the western equatorial Pacific warm pool during September-December 1992. *Journal of Geophysical Research,* 102(C4), 8533-8553. doi:10.1029/97JC00020

Da-Allada, C. Y., Alory, G., du Penhoat, Y., Kestenare, E., Durand, F., & Hounkonnou, N. M. (2013). Seasonal mixed-layer salinity balance in the tropical Atlantic Ocean: Mean state and seasonal cycle. *Journal of Geophysical Research Oceans*, 118, 332–345. doi:10.1029/2012JC008357

Darmaraki, S., Somot, S., Sevault, F., & Nabat, P. (2019). Past variability of Mediterranean Sea marine heatwaves. *Geophysical Research Letters*, 46, 9813–9823. doi:10.1029/2019GL082933

De Cotlogon, G., Leduc-Leballeur, M., Meynadier, R., Bastin, S., Diakhat, M., Eymard, L., et al. (2013). Atmospheric response to sea-surface temperature in the eastern equatorial Atlantic at quasi-biweekly time-scales. *Quarterly Journal of the Royal Meteorological Society*, 140. doi:1700-1714. doi:10.1002/qj.2250

Delcroix, T., & Henin, C. (1991). Seasonal and interannual variations of sea surface salinity in the tropical Pacific Ocean. *Journal of Geophysical Research*, 96(C12), 22135-22150. doi:10.1029/91JC02124

Deser, C., Alexander, M. A., Xie, S. -P., & Phillips, A. S. (2010). Sea surface temperature variability: patterns and mechanisms. Annual Review of Marine Science, 2, 115–143. doi:10.1146/annurev-marine-120408-151453

Dessier, A., & Donguy, J. R. (1994). The sea surface salinity in the tropical Atlantic between 10ºS and 30ºN- seasonal and interannual variations (1997-1989). *Deep-Sea Research I*, 41(1), 81-100. doi:10.1016/0967-0637(94)90027-2

Ding, H., Keenlyside, N. S., & Latif, M. (2009). Seasonal cycle in the upper equatorial Atlantic Ocean. *Journal of Geophysical Research*, 114, C09016. doi:10.1029/2009JC005418

Di Lorenzo, E. & Mantua, N. (2016). Multi-year persistence of the 2014/15 North Pacific marine heatwave. *Nature Climate Change*, 6, 1042-1047. doi:10.1038/nclimate3082

Doi, T., Vecchi, G. A., Rosati, A. J., & Delworth, T. L. (2012). Biases in the Atlantic ITCZ in seasonal-interannual variations for a coarse- and a high-resolution coupled climate model. *Journal of Climate*, 25, 5494-5511. doi:10.1175/JCLI-D-11-00360.1

Donner, S. D., Skriving, W. J., Little, C. M., Oppenheimer, M., & Hoegh-Guldberg, O. (2005). Global assessment of coral bleaching and required rates of adaptation under climate change. *Global Change Biology,* 11, 2251–2265. doi:10.1111/j.1365-2486.2005.01073.x

Dong, L., & McPhaden, M. J. (2018). Unusually warm Indian Ocean sea surface temperatures help to arrest development of El Niño in 2014. *Scientific Reports*, 8, 2249. doi:10.1038/s41598-018-20294-4

Eakin, C. M., Morgan, J. A., Heron, S. F., Smith, T. B., Liu, G., et al. (2010). Caribbean Corals in Crisis: Record Thermal Stress, Bleaching, and Mortality in 2005. *PLOS ONE,* 5(11): e13969. doi:10.1371/journal.pone.0013969

Edson, J. B., Jampana, V., Weller, R. A., Bigorre , S. P., Plueddemann, A. J., Fairall, C. W., et al. (2013). On the exchange of momentum over the open ocean. *Journal of Physical Oceanography*, 43(8), 1589-1610. doi:10.1175/JPO-D-12-0173.1

Exarchou, E., Prodhomme, C., Brodeau, L., Guemas, V., & Doblas-Reyes, F. (2017). Origin of the warm eastern tropical Atlantic SST bias in a climate model. *Climate Dyn*amics, 51, 1819-1840. doi:10.1007/s00382-017-3984-3

Fairall, C. W., Bradley, E. F., Hare, J. E., Grachev, A. A., & Edson, J. B. (2003). Bulk parameterization of air-sea fluxes: updates and verification for the COARE algorithm. *Journal of Clim*ate, 16, 571-591. doi:10.1175/1520-0442(2003)016<0571:BPOASF>2.0.CO;2

Feng, M., Hendon, H. H., Xie, S.‐P., Marshall, A. G., Schiller, A., Kosaka, Y., Caputi, N., & Pearce, A. (2015). Decadal increase in Ningaloo Niño since the late 1990s, *Geophysical Research Letters*, 42, 104– 112. doi:10.1002/2014GL062509

Feng, M., McPhaden, M. J., Xie, S. P. & Hafner, J. (2013). La Niña forces unprecedented Leeuwin Current warming in 2011. *Scientific Reports*, 3, 1227. doi:10.1038/srep01277

Fewings, M. R. & Brown, K. S. (2019). Regional Structure in the Marine Heat Wave of Summer 2015 Off the Western United States. *Frontiers in Marine Science*, 6, 564. doi:10.3389/fmars.2019.00564

Florenchie, P., Lutjeharms, J. R. E., Reason, C. J. C., Masson, S., & Rouault, M. (2003). The source of Benguela Niños in the South Atlantic Ocean. *Geophysical Research Letters*, 30(10), 1505. doi:10.1029/2003GL017172

Foltz, G. R., Grodsky, S. A., & Carton, J. A. (2003). Seasonal mixed layer heat budget of the tropical Atlantic Ocean. *Journal of Geophysical Research*, 108, 3146. doi:10.1029/2002JC001584

Foltz, G. R., Grodsky, S. A., & Carton, J. A. (2004). Seasonal salt budget of the northwestern tropical Atlantic Ocean along 38ºW. *Journal of Geophysical Research*, 109, C03052. doi:10.1029/2003JC002111

Foltz, G. R., & McPhaden, M. J. (2009). Impact of Barrier Layer Thickness on SST in the Central Tropical North Atlantic. *Journal of Climate*, 22, 285-299. doi:10.1175/2008JCLI2308.1

Foltz, G. R., Schmid, C., & Lumpkin, R. (2013). Seasonal cycle of the mixed layer heat budget in the northeastern tropical Atlantic Ocean. *Journal of Climate*, 26, 8169-8188. doi:10.1175/JCLI-D-13-00037.1

Freitag, H. P., McCarty, M. E., Nosse, C., Lukas, R., McPhaden, M. J., & Cronin, M. F. (1999). COARE Seacat data: Calibrations and quality control procedures (*NOAA Technical Memorandum ERL PMEL-115*). Seattle, WA: NOAA Pacific Marine Environmental Laboratory.

Freitag, H. P., Ning, C., Berk, P., Dougherty, D., Marshall, R., Strick, J. M., & Zimmerman, D. (2016). ATLAS, T-Flex, BaiLong meteorological sensor comparison test report (*NOAA Technical Memorandum OAR PMEL-148*). Seattle, WA: NOAA Pacific Marine Environmental Laboratory.

Freitag, H. P., O'Haleck, M., Thomas, G. C., & McPhaden, M. J. (2001). Calibration procedures and instrumental accuracies for ATLAS wind measurements (*NOAA Technical Memorandum OAR PMEL-119*). Seattle, WA: NOAA Pacific Marine Environmental Laboratory.

Freitag, H. P., Sawatzky, T. A., Ronnholm, K. B., & McPhaden, M. J. (2005). Calibration procedures and instrumental accuracy estimates of next generation ATLAS water temperature and pressure measurements (*NOAA Technical Memorandum OAR PMEL-128*, NTIS: PB2008-101764). Seattle, WA: NOAA Pacific Marine Environmental Laboratory.

Frölicher, T. L., Fischer, E. M., & Gruber, N. (2018). Marine heat waves under global warming. *Nature*, 560(7718), 360-–364. doi:10.1038/s41586-018-0383-9

Frölicher, T.L., & Laufkötter, C. (2018). Emerging risks from marine heat waves. *Nature Communications*, 9, 650 (2018). doi:10.1038/s41467-018-03163-6

Garrabou, J., Coma, R., Bensoussan, N., Bally, M., Chevaldonné, P., Cigliano, M., Diaz, D., Harmelin, J.G., Gambi, M.C., Kersting, D.K., Ledoux, J.B., Lejeusne, C., Linares, C., Marschal, C., Pérez, T., Ribes, M., Romano, J.C., Serrano, E., Teixido, N., Torrents, O., Zabala, M., Zuberer, F. & Cerrano, C. (2009), Mass mortality in Northwestern Mediterranean rocky benthic communities: effects of the 2003 heat wave. *Global Change Biology*, 15: 1090-1103. doi:10.1111/j.1365-2486.2008.01823.x

Gawarkiewicz, G., Chen, K., Forsyth, J., Bahr, F., Mercer, A. M., Ellertson, A., Fratantoni, P., Seim, H., Haines, S., & Han, L. (2019). Characteristics of an Advective Marine Heatwave in the Middle Atlantic Bight in Early 2017. *Frontiers in Marine Science*, 6:712. doi:10.3389/fmars.2019.00712

Gentemann, C. L., Fewings, M. R. & García‐Reyes, M. (2017). Satellite sea surface temperatures along the West Coast of the United States during the 2014–2016 northeast Pacific marine heat wave. *Geophysical Research Letters*, 44, 312– 319. doi:10.1002/2016GL071039

Gonzalez. R. C., & Woods, R. E. (2002). "Digital Image Processing," Second ed., Prentice Hall, Upper Saddle River, NJ, pp. 519-560.

Goubanova, K., Sanchez-Gomez, E., Frauen, C., & Voldoire, A. (2018). Respective roles of remote and local wind stress forcings in the development of warm SST errors in the south-eastern tropical Atlantic in a coupled high-resolution model, *Climate Dynamics*, 52, 1359-1382. doi:10.1007/s00382-018-4197-0

Grazzini, F., Ferranti, L., Lalaurette, F. & Vitart, F. (2003), The exceptional warm anomalies of summer 2003. ECMWF Newsletter, 99, 2–8.

Grazzini, F. & Viterbo, P. (2003). Record-breaking warm sea surface temperature of the Mediterranean Sea, ECMWF Newsletter, 98, 30–31.

Harlaß, J., Latif, M., & Park, W. (2018). Alleviating tropical Atlantic sector biases in the Kiel climate model by enhancing horizontal and vertical atmosphere model resolution: climatology and interannual variability. *Climate Dynamics*, 50, 2605-2635. doi:10.1007/s00382-017-3760-4

Hartmann, D. L. (2015). Pacific sea surface temperature and the winter of 2014. *Geophysical Research Letters*, 42, 1894– 1902. doi:10.1002/2015GL063083

Hayashida, H., Matear, R.J., Strutton, P.G., & Zhang, X. (2020). Insights into projected changes in marine heatwaves from a high-resolution ocean circulation model. *Nature Communications*, 11, 4352. doi:10.1038/s41467-020-18241-x

Hayes, S. P., McPhaden, M. J., & Wallace, J. M. (1989). The influence of sea-surface temperature on surface wind in the eastern equatorial Pacific: Weekly to monthly variability. *Journal of Climate*, 2, 1500-1506. doi:10.1175/1520-0442(1989)002<1500:TIOSST>2.0.CO;2

Hobday, A. J., Alexander, L. V., Perkins, S. E., Smale, D. A., Straub, S. C., Oliver, E. C. J., Benthuysen, J. A., Burrows, M. T., Donat, M. G., Feng, M., Holbrook, N. J., Moore, P. J., Scannell, H. A., Sen Gupta, A., & Wernberg, T. (2016). A hierarchical approach to defining marine heatwaves. *Progress in Oceanography*, 141, 227-238. doi:10.1016/j.pocean.2015.12.014

Holbrook, N. J., Scannell, H. A., Sen Gupta, A, Benthuysen, J. A., Feng, M., Oliver, E. C. J., Alexander, L. V., Burrows, M. T., Donat, M. G., Hobday, A. J., Moore, P. J., Perkins-Kirkpatrick, S. E., Smale, D. A., Straub, S. C., & Wernberg, T. (2019). A global assessment of marine heatwaves and their drivers. *Nature Communications*, 10, 2624. doi:10.1038/s41467-019-10206-z

Holbrook, N. J., Sen Gupta, A., Oliver, E. C. J., Hobday, A. J., Benthuysen, J. A., Scannell, H. A., Smale, D. A., & Wernberg, T. (2020). Keeping pace with marine heatwaves. *Nature Reviews Earth & Environment*, 1, 482–493. doi:10.1038/s43017-020-0068-4

Holte, J. & Talley, L. (2009). A New Algorithm for Finding Mixed Layer Depths with Applications to Argo Data and Subantarctic Mode Water Formation. *Journal of Atmospheric and Oceanic Technology*, 26, 1920–1939. doi:10.1175/2009JTECHO543.1

Hopkins, J., Lucas, M., Dufau, C., Sutton, M., Stum, J., Lauret, O., & Channelliere, C. (2013). Detection and variability of the Congo River plume from satellite derived sea surface temperature, salinity, ocean colour and sea level. *Remote Sensing of Environment*, **139**, 365-385. doi:10.1016/j.rse.2013.08.015

Hughes, T., Kerry, J., Álvarez-Noriega, M. et al. (2017). Global warming and recurrent mass bleaching of corals. *Nature,* 543, 373–377. doi:10.1038/nature21707

Intergovernmental Oceanographic Commission, SCOR, and IAPSO (2010). The international thermodynamic equation of seawater – 2010: Calculation and use of thermodynamic properties, Intergovernmental Oceanographic Commission, Manuals and Guides No. 56, 196 pp., UNESCO

Jackson, J. M., Johnson, G. C., Dosser, H. V., & Ross, T. (2018). Warming from recent marine heatwave lingers in deep British Columbia fjord. *Geophysical Research Letters*, 45, 9757– 9764. doi:10.1029/2018GL078971

Jacox, M. G., Hazen, E. L., Zaba, K. D., Rudnick, D. L., Edwards, C. A., Moore, A. M. & Bograd, S. J. (2016). Impacts of the 2015–2016 El Niño on the California Current System: Early assessment and comparison to past events, *Geophysical Research Letters*, 43, 7072-7080. doi:10.1002/2016GL069716

Jayne, S.R., Roemmich, D., Zilberman, N., Riser, S. C., Johnson, K. S., Johnson, G. C., & Piotrowicz, S. R. (2017). The Argo Program: Present and future. *Oceanography*, 30(2), 18–28. doi:10.5670/oceanog.2017.213

Joh, Y., & Di Lorenzo, E. (2017). Increasing coupling between NPGO and PDO leads to prolonged marine heatwaves in the northeast Pacific, *Geophysical Research Letters*, 44(22): 663-671. doi:10.1002/2017GL075930

Kataoka, T., Tozuka, T., Behera, S. & Yamagata, T. (2014). On the Ningaloo Niño/Niña. *Climate Dynamics.* 43, 1463–1482. doi:10.1007/s00382-013-1961-z

Kayanne, H. (2017). Validation of degree heating weeks as a coral bleaching index in the northwestern Pacific. *Coral Reefs*, 36(1), 63–70. doi:10.1007/s00338-016-1524-y

Kim, W., Yeh, S.‐W., Kim, J.‐H., Kug, J.‐S., & Kwon, M. (2011). The unique 2009–2010 El Niño event: A fast phase transition of warm pool El Niño to La Niña, *Geophysical Research Letters*, 38, L15809. doi:10.1029/2011GL048521

Kolodziejczyk, N., Boutin, J., Vergely, J. -L., Marchand, S., Martin, N., & Reverdin, G. (2016). Mitigation of systematic errors in SMOS sea surface salinity. *Remote Sensing of Environment*, 180, 164-177. doi:10.1016/j.rse.2016.02.061

Kug, J.‐S., & I.‐S. Kang (2006). Interactive feedback between ENSO and the Indian Ocean, *Journal of Climate*, 19(9), 1784–1801. doi:10.1175/JCLI3660.1

Kumar, B. P., Vialard, J., Lengaigne, M., Murty, V. S. N., McPhaden, M. J., Cronin, M. F., Pinsard, F., & Reddy, K. G. (2013). TropFlux wind stresses over the tropical oceans: evaluation and comparison with other products. *Climate Dynamics,* 40, 2049-2071. doi:10.1007/s00382-012-1455-4

Lake, B. J., Noor, S. M., Freitag, H. P., & McPhaden, M. J. (2003). Calibration procedures and instrumental accuracy estimates of ATLAS air temperature and relative humidity measurements (*NOAA Technical Memorandum OAR PMEL-123*). Seattle, WA: NOAA Pacific Marine Environmental Laboratory.

Lee, T., Hobbs, W. R., Willis, J. K., Halkides, D., Fukumori, I., Armstrong, E. M., Hayashi, A. K., Liu, W. T., Patzert, W., & Wang, O. (2010). Record warming in the South Pacific and western Antarctica associated with strong central-Pacific El Niño in 2009-10, *Geophysical Research Letters*, 37, L19704. doi:10.1029/2010GL044865

Lee, M., Hong, C. & Hsu, H. (2015). Compounding effects of warm sea surface temperature and reduced sea ice on the extreme circulation over the extratropical North Pacific and North America during the 2013–2014 boreal winter. *Geophysical Research Letters*, 42, 1612–1618. doi:10.1002/2014GL062956

Li, G., Cheng, L., Zhu, J., Trenberth, K. E., Mann, M. E., & Abraham, J. P. (2020). Increasing ocean stratification over the past half-century. *Nature Climate Change*, doi:10.1038/s41558-020-00918-2

Li, T., & Philander, S. G. H. (1997). On the seasonal cycle of the equatorial Atlantic Ocean. *Journal of Climate*, 10, 813-817. doi:10.1175/1520-0442(1997)010<0813:OTSCOT>2.0.CO;2

Laufkötter, C., Zscheischler, J., & Frölicher, T. L. (2020). High-impact marine heatwaves attributable to human-induced global warming, Science, 369(6511), 1621-1625. doi:10.1126/science.aba0690

Lübbecke, J. F., Böning, C. W., Keenlyside, N. S., & Xie, S.-P. (2010). On the connection between Benguela and equatorial Atlantic Niños and the role of the South Atlantic Anticyclone. *Journal of Geophysical Research*, 115, C09015. doi:10.1029/2009JC005964

Luterbacher, J., Dietrich, D., Xoplaki, E., Grosjean, M., & Wanner, H. (2004). European seasonal and annual temperature variability, trends and extremes since 1500, *Science*, 303, 1499–1503. doi:10.1126/science.1093877

McCabe, R. M., Hickey, B. M., Kudela, R. M., Lefebvre, K. A., Adams, N. G., Bill, B. D., Gulland, F. M. D., Thomson, R. E., Cochlan, W. P., & Trainer, V. L. (2016). An unprecedented coastwide toxic algal bloom linked to anomalous ocean conditions, *Geophysical Research Letters*, 43, 10366–10376. doi:10.1002/2016GL070023.

McDougall, T. J., & Krzysik, O. A. (2015). Spiciness, *Journal of Marine Research*, 73, 141-152. doi:10.1357/002224015816665589

McGowan, H., & Theobald, A. (2017). ENSO weather and coral bleaching on the Great Barrier Reef, Australia, *Geophysical Research Letters*, 44. doi:10.1002/2017GL074877

McPhaden, M. J. (2015), Playing hide and seek with El Niño. *Nature Climate Change,* 5, 791–795. doi:10.1038/nclimate2775

McPhaden, M. J. (1982). Variability in the central equatorial Indian Ocean. Part II: Oceanic heat and turbulent energy balance. *Journal of Marine Research,* 40, 403–419.

Mills, K. E., Pershing, A.J., Brown, C.J., Chen, Y., Chiang, F.-S., Holland, D.S., Lehuta S., Nye, J.A., Sun, J.C., Thomas, A.C., & Wahle, R. A. (2013). Fisheries management in a changing climate: Lessons from the 2012 ocean heat wave in the Northwest Atlantic. *Oceanography,* 26(2):191–195. doi:10.5670/oceanog.2013.27

Mitchell, T. P., & Wallace, J. M. (1992). On the annual cycle in equatorial convection and sea surface temperature. *Journal of Climate*, 5, 1140–1156. doi:10.1175/1520-0442(1992)005<1140:TACIEC>2.0.CO;2

Moisan, J. R., & Niiler, P. P. (1998). The seasonal heat budget of the North Pacific: net heat flux and heat storage rates (1950-1990). *Journal of Physical Oceanography*, 28, 401-421. doi:10.1175/1520-0485(1998)028<0401:TSHBOT>2.0.CO;2

Morel, A (1988). Optical modeling of the upper ocean in relation to its biogenous matter content (case I waters). *Journal of Geophysical Research*, 93(C9), 10749-10768. doi:10.1029/JC093iC09p10749

Munk, W., 1981: Internal waves and small-scale processes. *Evolution of Physical Oceanography*, B. A. Warren and C. Wunsch, Eds., MIT Press, 264–291

Nnamchi, H., Li, J., Kucharski, F., Kang, I.-S., Keenlyside, N. S., Chang, P., & Farneti, R. (2015). Thermodynamic controls of the Atlantic Niño. *Nature Communications*, 6, 8895. doi:10.1038/ncomms9895

Olita, A., Sorgente, R., Ribotti, A., Natale, S. & Gaberšek, S. (2007). Effects of the 2003 European heatwave on the Central Mediterranean Sea surface layer: a numerical simulation. *Ocean Science Discussions,* 3, 85–125. doi:10.5194/os-3-273-2007

Oliver, E. C. J., Donat, M. G., Burrows, M. T., Moore, P. J., Smale, D. A., Alexander, L. V., Benthuysen, J. A., Feng, M., Sen Gupta, A., Hobday, A. J., Holbrook, N. J., Perkins-Kirkpatrick, S. E., Scannell, H. A., Straub, S. C. & Wernberg, T. (2018). Longer and more frequent marine heatwaves over the past century, *Nature Communications*, 9, 1324, doi:10.1038/s41467-018-03732-9

Oliver, E. C. J., Lago, V., Hobday, A. J., Holbrook, N. J., Ling, S., & Mundy, C. (2018). Marine heatwaves off eastern Tasmania: Trends, interannual variability, and predictability. *Progress in Oceanography,* 161. doi:10.1016/j.pocean.2018.02.007

Oliver, E. C. J., Perkins-Kirkpatrick, S. E., Holbrook, N. J., & Bindoff, N. L. (2018). Anthropogenic and natural influences on record 2016 marine heat waves. In "Explaining Extreme Events of 2016 from a Climate Perspective", *Bulletin of the American Meteorological Society*, 99(1), S44–S48, doi:10.1175/BAMS-ExplainingExtremeEvents2016.1.

Oliver, E., Benthuysen, J., Bindoff, N., Hobday, A. J., Holbrook, N. J., Mundy, C. N., & Perkins-Kirkpatrick, S. E. (2017). The unprecedented 2015/16 Tasman Sea marine heatwave. *Nature Communications*, 8, 16101. doi:10.1038/ncomms16101

Patricola, C. M., Li, M., Xu, Z., Change, P., Saravanan, & R., Hsieh (2012). An investigation of tropical Atlantic bias in a high-resolution coupled regional climate model. *Climate Dynamics*, 39, 2443-2463. doi:10.1007/s00382-012-1320-5

Pearce, A. F. & Feng, M. (2013). The rise and fall of the 'marine heat wave' off Western Australia during the summer of 2010/2011. *Journal of Marine Systems*, 111–112, 139–156. doi:10.1016/j.jmarsys.2012.10.009

Pearce, A., Lenanton R., Jackson, G., Moorel, J., Feng, M., & Gaughan, D. (2011). The "Marine Heat Wave" Off Western Australia During the Summer of 2010/11. Fisheries Research Report No. 222 (40pp) (Department of Fisheries, Western Australia)

Pershing, A. J., Record, N. R., Franklin, B. S., Kennedy, B. T., McClenachan, L., Mills, K. E., Scott, J. D., Thomas, A. C., & Wolf, N. H. (2019). Challenges to natural and human communities from surprising ocean temperatures. Proceedings of the National Academy of Sciences, 116(37), 18378–18383. doi: 10.1073/pnas.1901084116

Pilo, G. S., Holbrook, N. J., Kiss, A. E., & Hogg, A. M. (2019). Sensitivity of marine heatwave metrics to ocean model resolution. *Geophysical Research Letters*, 46, 14604–14612. doi:10.1029/2019GL084928

Plimpton, P. E., Freitag, H. P., & McPhaden, M. J. (1995). Correcting moored ADCP data for fish-bias errors at 0,110W and 0,140W from 1990 to 1993 (*NOAA Technical Memorandum ERL PMEL-107*). Seattle, WA: NOAA Pacific Marine Environmental Laboratory.

Plimpton, P. E., Freitag, H. P., & McPhaden, M. J. (2004). Processing of subsurface ADCP data in the equatorial Pacific (*NOAA Technical Memorandum OAR PMEL-125*). Seattle, WA: NOAA Pacific Marine Environmental Laboratory.

Qiu, B., & Huang, R. X. (1995). Ventilation of the North Atlantic and North Pacific: Subductions Versus Obduction, *Journal of Physical Oceanography*, 25, 2374-2390. doi:10.1175/1520-0485(1995)025<2374:VOTNAA>2.0.CO;2

Qu, X., Hall, A., Klein, S. A., & Caldwell, P. M. (2014). On the spread of changes in marine low cloud cover in climate model simulations of the 21st century. *Climate Dynamics*, 42, 2603-2626. doi:10.1007/s00382-013-1945-z

Reynolds, R. W., Smith, T. M., Liu, C., Chelton, D. B., Casey, K. S., & Schlax, M. G. (2007). Daily High-Resolution-Blended Analyses for Sea Surface Temperature. *Journal of Climate*, 20, 5473-5496. doi:10.1175/2007JCLI1824.1

Reynolds, R. W., Rayner, N. A., Smith, T. M., Stokes, D. C. & Wang W. (2002). An improved in situ and satellite SST analysis for climate, *Journal of Climate*, 15, 1609-1625. doi:10.1175/1520-0442(2002)015<1609:AIISAS>2.0.CO;2

Rhein, M. et al., 2013: Observations: Ocean. In: Climate Change 2013: The Physical Science Basis. Contribution of Working Group I to the Fifth Assessment Report of the Intergovernmental Panel on Climate Change [Stocker, T.F., D. Qin, G.-K. Plattner, M. Tignor, S.K. Allen, J.

Boschung, A. Nauels, Y. Xia, V. Bex and P.M. Midgley (eds.)]. Cambridge University Press, Cambridge, United Kingdom and New York, NY, USA, 255-316.

Richter, I., Behera, S. K., Masumoto, Y., Taguchi, B., Komori, N., & Yamagata, T. (2010). On the triggering of Benguela Niños: Remote equatorial versus local influences. *Geophysical Research Letters*, 37(20), L20604. doi:10.1029/2010GL044461

Richter, I. (2015). Climate model biases in the eastern tropical oceans: causes, impacts and ways forward. *WIREs Climate Change*, 6(3), 345-358. doi:10.1002/wcc.338

Riser, S. C., Freeland, H. J., Roemmich, D., Wijffels, S., Troisi, A., Belboch, M., et al. (2016). Fifteen years of ocean observations with the global Argo array. *Nature Climate Change*, 6, 145-153. doi:10.1038/nclimate2872

Roemmich, D. & Gilson, J. (2009). The 2004-2008 mean and annual cycle of temperature, salinity, and steric height in the global ocean from the Argo Program, *Progress in Oceanography*, 82, 81-100. doi:10.1016/j.pocean.2009.03.004

Rouault, M., Illig, S., Bartholomae, C., Reason, C. J. C., & Bentamy, A. (2007). Propagation and origin of warm anomalies in the Angola Benguela upwelling system in 2001. *Journal of Marine Systems*, 68(3–4), 473–488. doi10.1016/j.jmarsys.2006.11.010

Rouault, M., Servain, J., Reason, C. J. C., Bourles, B., Rouault, M. J., & Fauchereau, N. (2009). Extension of PIRATA in the tropical south-east Atlantic: an initial one-year experiment. *African Journal of Marine Science*, 31(1), 63-71. doi:10.2989/AJMS.2009.31.1.5.776

Scannell, H. A., G. C. Johnson, L. Thompson, J. M. Lyman, & S. Riser, Subsurface Evolution and Persistence of Marine Heatwaves in the Northeast Pacific, *Geophysical Research Letters*, accepted

Scannell, H. A., Pershing, A. J., Alexander, M. A., Thomas, A. C., & Mills, K. E. (2016). Frequency of marine heatwaves in the North Atlantic and North Pacific since 1950, *Geophys. Res. Lett.*, 43. doi:10.1002/2015GL067308

Scannell, H. A., & McPhaden, M. J. (2018). Seasonal mixed layer temperature balance in the Southeastern Tropical Atlantic, *J. Geophys. Res. Oceans*, 123, 5557–5570. doi:10.1029/2018JC014099

Schlegel, R. W., Oliver, E. C. J., Hobday, A. J., & Smit, A. J. (2019). Detecting Marine Heatwaves With Sub-Optimal Data. *Frontiers in Marine Science*, 6:737. doi:10.3389/fmars.2019.00737

Schmeisser, L., Bond, N. A., Siedlecki, S.A., & Ackerman, T. P. (2019). The role of clouds and surface heat fluxes in the maintenance of the 2013–2016 Northeast Pacific marine heatwave, *Journal of Geophysical Research: Atmospheres*, 124, 10772-10783. doi:10.1029/2019JD030780

Sen Gupta, A., Thomsen, M., Benthuysen, J. A., Hobday, A. J., Oliver, E. C. J., Alexander, L. V., Burrows, M. T., Donat, M. G., Feng, M., Holbrook, N. J., Perkins-Kirkpatrick, S., Moore, P. J., Rodrigues, R. R., Scannell, H. A., Tascheto, A. S., Ummenhofer, C. C., Wernberg, T. & Smale, D. A. (2020). Drivers and impacts of the most extreme marine heatwaves events. *Scientific Reports*, 10, 19359. https://doi.org/10.1038/s41598-020-75445-3

Serra, Y. L., A'Hearn, P., Freitag, H. P., & McPhaden, M. J. (2001). ATLAS self-siphoning rain gauge error estimates. *Journal of Atmospheric and Oceanic Technology*, 18, 1989-2002. doi:10.1175/1520-0426(2001)018<1989:ASSRGE>2.0.CO;2

Servain, J., Busalacchi, A. J., McPhaden, M. J., Moura, A. D., Reverdin, G., Vianna, M., & Zebiak, S. E. (1998). A Pilot Research Moored Array in the Tropical Atlantic (PIRATA). *Bulletin of the American Meteorological Society*, 79(10), 2019–2031. doi:10.1175/1520-0477(1998)079<2019:APRMAI>2.0.CO;2

Sherwood, S. C., Bony, S., & Dufresne, J. -L. (2014). Spread in model climate sensitivity traced to atmospheric convective mixing. *Nature*, 505, 37-42. doi:10.1038/nature12829

Smale, D. A., Wernberg, T., Oliver, E. C. J., Thomsen, M., Harvey, B. P., Straub, S. C., Burrows, M. T., Alexander, L. V., Benthuysen, J. A., Donat, M. G., Feng, M., Hobday, A. J., Holbrook, N. J., Perkins-Kirkpatrick, S. E., Scannell, H. A., Sen Gupta, A., Payne, B. L. & Moore, P. J. (2019). Marine heatwaves threaten global biodiversity and the provision of ecosystem services, *Nature Climate Change*, 9, 306-312. doi:10.1038/s41558-019-0412-1

Smith, S. D. (1988). Coefficients for sea surface wind stress, heat flux, and wind profiles as a function of wind speed and temperature. *Journal of Geophysical Research*, 93(C12), 15467-15472. doi:10.1029/JC093iC12p15467

Sparnocchia, S., Schiano, M. E., Picco, P., Bozzano, R. & Cappelletti, A. (2006). The anomalous warming of summer 2003 in the surface layer of the Central Ligurian Sea (Western Mediterranean). *Annales Geophysicae,* 24, 443–452. doi:10.5194/angeo-24-443-2006

Spillman, C., & Alves, O. (2009). Dynamical seasonal prediction of summer sea surface temperatures in the Great Barrier Reef. *Coral Reefs,* 28, 197–206. doi:https://doi.org/10.1007/s00338-008-0438-8

Sprintall, J., & Tomczak, M. (1992). Evidence of the barrier layer in the surface layer of the tropics. Jour*nal of Geophysical Research*, 97(C5), 7305-7316. doi:10.1029/92JC00407

Stevenson, J. W., & Niiler, P. P. (1983). Upper ocean heat budget during the Hawaii-to-Tahiti shuttle experiment. *Journal of Physical Oceanography*, 13, 1894-1907. doi:10.1175/1520-0485(1983)013<1894:UOHBDT>2.0.CO;2

Sutton, R. T., & Hodson, D. L. R. (2005). Atlantic Ocean forcing of North American and European summer climate. *Science*, 309(5731), 115–118. doi: 10.1126/science.1109496

ten Veldhuis, J. (2011). Urban flood risk assessment. *Journal of Flood Risk Management*, 4, 281-287. doi:10.1111/j.1753-318X.2011.01112.x

Tseng, Y.-H., Ding, R., & Huang, X.-M. (2017). The warm Blob in the northeast Pacific-the bridge leading to the 2015/2016 El Niño. Environmental Research Letters, 15(5). doi:10.1088/1748-9326/aa67c3

Tzortzi, E., Josey, S. A., Srokosz, M., & Gommenginger, C. (2013). Tropical Atlantic salinity variability: New insights from SMOS. *Geophysical Research Letters*, 40, 2143–2147. doi:10.1002/grl.50225

Valleron, A. J., & Boumendil, A. (2004). Epidemiology and heat waves: Analysis of the 2003 episode in France, *Comptes Rendus Biologies*, 327, 1125–1141. doi:10.1016/j.crvi.2004.09.009

Wallace, J. M., Mitchell, T. P., & Deser, C. (1989). The influence of sea surface temperature on surface wind in the eastern equatorial Pacific: Seasonal and interannual variability. *Journal of Climate*, 2, 1492-1499. https://doi.org/10.1175/1520-0442(1989)002<1492:TIOSST>2.0.CO;2

Wang, W., & McPhaden, M. J. (1999). The surface-layer heat balance in the equatorial Pacific Ocean. Part I: Mean seasonal cycle. *Journal of Physical Oceanography*, 29, 1812-1831. https://doi.org/10.1175/1520-0485(1999)029<1812:TSLHBI>2.0.CO;2

Wang, S. -Y., Hipps, L., Gillies, R. R., & Yoon, J.H. (2014). Probable causes of the abnormal ridge accompanying the 2013–2014 California drought: ENSO precursor and anthropogenic warming footprint. *Geophysical Research Letters*, 41(9), 3220–3226. doi:10.1002/2014GL059748.

Weisberg, R. H., & Tang, T. Y. (1990). A linear analysis of equatorial Atlantic Ocean thermocline variability. *Journal of Physical Oceanography*, 20, 1813-1825. https://doi.org/10.1175/1520-0485(1990)020<1813:ALAOEA>2.0.CO;2

Weller, E., Min, S., Lee, D., Kug, J., Cai, W., & Yeh, S. (2015). Human Contribution to the 2014 Record High Sea Surface Temperatures Over the Western Tropical And Northeast Pacific Ocean. *Bulletin of the American Meteorological Society*, 96(12), S100–S104. doi:10.1175/bams-d-15-00055.1.

Wernberg, T., Bennett, S., Babcock, R. C., de Bettignies, T., Cure, K., Depczynski, M., Dufois, F., Fromont, J., Fulton, C. J., Hovey, R. K., Harvey, E. S., Holmes, T. H., Kendrick, G. A., Radford, B., Santana-Garcon, J., Saunders, B. J., Smale, D. A., Thomsen, M. S., Tuckett, C. A., Tuya, F., Vanderklift, M.A., & Wilson, S. (2016). Climate-driven regime shift of a temperate marine ecosystem. *Science Reports*, 353, 169–172. doi:10.1126/science.aad8745

Wilks, D. S. (2011). Statistical methods in the atmospheric sciences (Vol. 100). Academic press.

Wood, R. (2012). Review: Stratocumulus Clouds. *Monthly Weather Review*, 140, 2373-2423. doi:10.1175/MWR-D-11-00121.1

Xie, S. -P., & Carton, J. A. (2004). Tropical Atlantic variability: patterns, mechanisms, and impacts. In *Earth's Climate: The Ocean-Atmosphere Interaction*, Wang, C., Xie, S. -P., & Carton, J. A. (Eds.), Geophysical Monograph, 147. Washington, D.C.: AGU Press, 121-142. doi:10.1029/147GM07

Yamagata, T., & Iizuka, S. (1995). Simulation of the tropical thermal domes in the Atlantic: A seasonal cycle. *Journal of Physical Oceanography*, 25, 2129-2140. doi:10.1175/1520-0485(1995)025<2129:SOTTTD>2.0.CO;2

Yoo, S.‐H., J. Fasullo, S. Yang, & C.‐H. Ho (2010). On the relationship between Indian Ocean sea surface temperature and the transition from El Niño to La Niña, *Journal of Geophysical Research*, 115, D15114. doi:10.1029/2009JD012978

Yu, L., Jin, X., & Weller, R. A. (2006). Role of net surface heat flux in seasonal variations of sea surface temperature in the tropical Atlantic Ocean. *Journal of Climate*, 19, 6153-6169. doi:10.1175/JCLI3970.1

Zaba, K. D. & Rudnick, D. L. (2016). The 2014–2015 warming anomaly in the Southern California Current System observed by underwater gliders. *Geophysical Research Letters*, 43, 1241-1248. doi:10.1002/2015GL067550

Zuidema, P., Chang, P., Medeiros, B., Kirtman, B. P., Mechoso, R., Schneider, E. K., et al. (2016). Challenges and prospects for reducing coupled climate model SST biases in the eastern tropical Atlantic and Pacific Oceans. *Bulletin of the American Meteorological Society*, 97(12), 2305-2327. doi:10.1175/BAMS-D-15-00274